CHALMERS
UNIVERSITY OF TECHNOLOGY

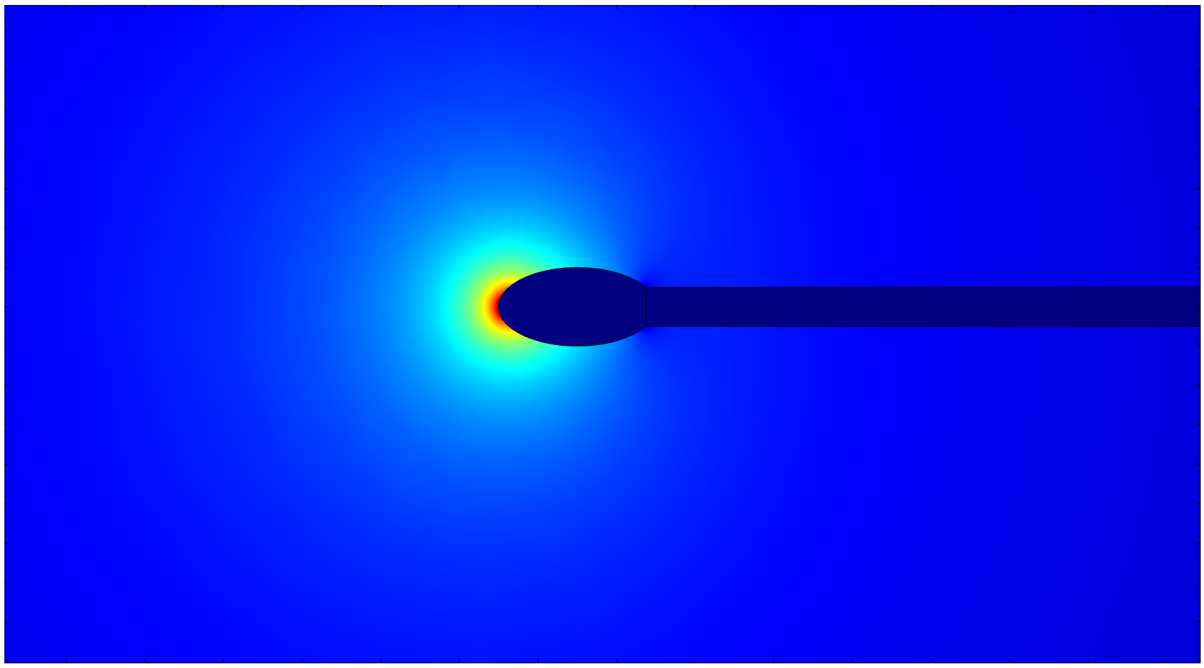

Crack propagation in dynamic power cables

Master's thesis in the International Master's Programme in Naval Architecture and Ocean Engineering

JAYAKRISHNAN HARIKUMAR
RÉMI ROUX

DEPARTMENT OF MECHANICS AND MARITIME SCIENCES
DIVISION OF MARINE TECHNOLOGY

CHALMERS UNIVERSITY OF TECHNOLOGY
Gothenburg, Sweden 2021
www.chalmers.se

MASTER'S THESIS IN THE INTERNATIONAL MASTER'S PROGRAMME
NAVAL ARCHITECTURE AND OCEAN ENGINEERING

Crack propagation in dynamic power cables

JAYAKRISHNAN HARIKUMAR and RÉMI ROUX

Department of Mechanics and Maritime Sciences
Division of Marine Technology
CHALMERS UNIVERSITY OF TECHNOLOGY
Göteborg, Sweden 2021

Crack propagation in dynamic power cables

JAYAKRISHNAN HARIKUMAR and RÉMI ROUX

Master's Thesis 2021:72
Department of Mechanics and Maritime Sciences
Division of Marine Technology
Chalmers University of Technology
SE-412 96 Göteborg
Sweden
Telephone: + 46 (0)31-772 1000

Cover figure:
Water tree simulation model from the thesis, simulated in COMSOL Multiphysics (2020)

Chalmers Reproservice
Göteborg, Sweden 2021

Crack propagation in dynamic power cables

Master's thesis in Naval Architecture and Ocean Engineering
JAYAKRISHNAN HARIKUMAR and RÉMI ROUX
Department of Mechanics and Maritime Sciences
Division of Marine Technology
Chalmers University of Technology

Abstract

Renewable energy has been the focus of recent years to decrease carbon emissions and global warming. Among them, wave energy has a high potential of being one of the primary sources of sustainable energy. Wave energy is harnessed using wave energy converters (WECs) which have multiple possible configurations. All these technologies need to transport the energy produced to the distribution centres on land. This step is carried out by dynamic subsea cables. Their service life is crucial for the profit of these solutions. The presence of water molecules in the insulating material causes a crack filled with water called a water tree, which grows with time and decreases the service life of these cables. This thesis studies the possible parameters that influence the water tree propagation: cyclic mechanical loading and Maxwell stresses.

The working environment for a dynamic cable connected to a WEC causes motions in the cable that subjects it to mechanical loads. These cable motions are studied by simulations of various sea states for the Waves4Power WEC WaveEL 3.0 installed in Runde, Norway, using the SIMA software. The results from this global model simulations are post-processed in MATLAB, and the fatigue life of the cable is determined over its length to determine the fatigue-critical locations. A local FE model of the cable is created in the ABAQUS software to simulate and analyse a segment of the cable. The stress responses in the conductor's insulation material are analysed in MATLAB using an in-house fatigue crack propagation code based on linear elastic fracture mechanics (LEFM). The results show only short propagation of the initial crack introduced to the insulation material for the simulated sea states and cable configuration. Hence, it was concluded the motion-induced stresses in the current case study have negligible influence on the cable's service life.

The flow of current causes an electric field in the cable's conductors which give rise to cyclic variations of Maxwell stresses. A model was developed in the COMSOL Multiphysics software to simulate this electric field. The model allows studying the electric field variation due to the presence of a water tree. The cyclic variation of the simulated Maxwell stress was used in a water tree growth model to determine its limitation in service life due to water tree growth using an in-house MATLAB code. The results show that water tree growth due to the cyclic variation of Maxwell stresses has a more considerable impact on the cable's service life than motions-induced stresses.

Keywords: Fatigue life, Fracture mechanics, Maxwell stresses, Subsea dynamic cable, Water tree, Wave Energy

Contents

Preface

This thesis has been carried by Jayakrishnan Harikumar and Rémi Roux according to the requirement for the master's degree at the Chalmers University of Technology. The work has been carried out at the Division of Marine Technology, Department of Mechanics and Maritime Sciences, Chalmers University of Technology between January and June of 2021.

First, we would like to thank Professor Jonas W. Ringsberg which has been the supervisor and examiner for this thesis. Along with this work, he has always been very kind, patient, and helpful. His expertise allowed us to learn a lot during this thesis, but also to better understand how to carry out a complex subject.

Then, we would also like to thank Shun-Han Yang and Zhiyuan Li for their help, their involvement, and their guidance through the thesis. They have been providing useful advice and help during all the thesis and, their knowledge offered us ways to carry out the thesis.

A special thanks to Professor Yuriy Serdyuk for his expertise in water trees. He gave us knowledge on water tree propagation and how experimentations are carried out.

Finally, we would like to thank our friends and family for their support throughout the thesis. A special thanks to both our opponents Anirudh Mallya Ullal and Fabian M. Ebbesson which agreed on reviewing our work and for their insight during the work.

Göteborg, 2021-10-31

Nomenclature

List of acronyms

EPFM	Elastic-Plastic Fracture Mechanics
FDA	Fatigue Damage Accumulation
HDE	Hydrodynamic Efficiency
LEFM	Linear Elastic Fracture Mechanics
MPC	Multiple Points Constraints
WEC	Wave Energy Converter
XLPE	Cross-Linked Polyethylene

List of symbols

a	Crack length	[m]
a_t	Crack length before an increment	[m]
a_{t+1}	Crack length after an increment	[m]
C	Growth rate	[mm/cycle]
c_0	Speed of light in vacuum	[m/s]
D	Damage accumulation	[-]
$Displ_X$	Displacement used as input in ABAQUS (2020) on the SIMA (2020) coordinate system along X	[mm]
$Displ'_X$	Displacement used as input in ABAQUS (2020) on the ABAQUS (2020) coordinate system along X	[mm]
$Displ_Y$	Displacement used as input in ABAQUS (2020) on the SIMA (2020) coordinate system along Y	[mm]
$Displ'_Y$	Displacement used as input in ABAQUS (2020) on the ABAQUS (2020) coordinate system along Y	[mm]
$Displ_Z$	Displacement used as input in ABAQUS (2020) on the SIMA (2020) coordinate system along Z	[mm]
$Displ'_Z$	Displacement used as input in ABAQUS (2020) on the ABAQUS (2020) coordinate system along Z	[mm]
D_{WEC}	Width of the WEC	[m]
E	Electric field strength	[Vm^{-1}]
EA	Axial stiffness	[N]
EI	Bending stiffness	[Nm²]
F	Maxwell stress	[Pa]
F_{axial}	Axial force	[N]
f	Geometry factor	[-]
g	Gravity constant	[$m.s^{-2}$]
H	Wave surface elevation	[m]
H_s	Wave height	[m]
K	Stress intensity factor	[-]
K_I	Stress intensity factor of mode I	[-]
K_{II}	Stress intensity factor of mode II	[-]
$K_{case\#1}$	Stress intensity factor of fracture model #1	[-]
$K_{case\#2}$	Stress intensity factor of fracture model #2	[-]
$K_{case\#3}$	Stress intensity factor of fracture model #3	[-]
$K_{case\#4}$	Stress intensity factor of fracture model #4	[-]
K_{eff}	Effective stress intensity factor	[-]
K_i	Stress intensity factor of the stress range	[-]
K_{th}	Minimum stress intensity factor	[-]
k	Stress levels	[-]
L	Initial length of the beam	[m]

L_{lay}	Length for a complete layup rotation	[m]
l_{segm}	Length of the segment taken in SIMA (2020)	[mm]
m	Fatigue crack exponent	[-]
N_i	Number of cycles needed for the material to fail of the stress level	[-]
N_f	Number of cycles needed for the material to fail	[-]
n_i	Number of occurrences of the stress level	[-]
P	Bending force	[N]
P_d	Mean absorbed power	[W]
P_w	Wave power per unit length	[W/m]
R_{lay}	Radius of the layup rotation	[m]
r	Radius	[m]
$S33$	Axial stress from ABAQUS (2020)	[MPa]
T	Wave period	[s]
T_z	Wave period	[s]
u	Deformation	[m]
V_0	Volume of XLPE	$[m^3]$
V_0	Voltage	[V]
X_1	X position at the beginning of the segment (end point 1)	[mm]
X_2	X position at the end of the segment (end point 2)	[mm]
X_{theo}	Theoretical X position at the end point 2 of the cable	[mm]
Y_1	Y position at the beginning of the segment (end point 1)	[mm]
Y_2	Y position at the end of the segment (end point 2)	[mm]
Y_a, Y_a', Y_a''	Axial coefficients due to the geometry	[-]
Y_b, Y_b', Y_b''	Axial coefficients due to the geometry	[-]
Y_{theo}	Theoretical Y position at the end point 2 of the cable	[mm]
Z_1	Z position at the beginning of the segment (end point 1)	[mm]
Z_2	Z position at the end of the segment (end point 2)	[mm]
Z_{theo}	Theoretical Z position at the end point 2 of the cable	[mm]
α	Angle between the coordinate system in SIMA (2020) and the cable around Y-axis	[rad]
α_{lay}	Angle of the layup rotation	[rad]
α_{geo}	Geometry coefficient	[-]
β	Angle between the coordinate system in SIMA (2020) and the cable around Z-axis	[rad]
Δ_{max}	Maximum beam deflection	[m]
$\Delta\sigma$	Stress range	[MPa]
ϵ_0	Vacuum permittivity	$[Fm^{-1}]$
ϵ_r	Relative permittivity	$[Fm^{-1}]$
ρ	Seawater density	$[kg.m^{-3}]$
σ_{axial}	Axial stress	[MPa]
$\sigma_{bending}$	Bending stress	[MPa]
σ_{max}	Maximum axial stress from ABAQUS (2020)	[MPa]
σ_{min}	Minimum axial stress from ABAQUS (2020)	[MPa]
$\sigma_{min,\ axial}$	Minimum axial stress to propagate the crack	[MPa]
$\sigma_{min,\ bending}$	Minimum bending stress to propagate the crack	[MPa]
σ_{yield}	Yield strength of XLPE	[MPa]
μ_0	Vacuum permeability	[H/m]

1 Introduction

This chapter aims to give a basic understanding of the need for this thesis. The background and motivation sections provide the context of the thesis along with some of the challenges involved. The objective and goals introduce the aims of the work that has been divided into multiple phases. Finally, the scope of the thesis, the various assumptions, and limitations are defined. The last section provides an overview of the layout of the entire report.

1.1 Background and motivation

In the last decades, electricity has played a crucial role in the improvement of living conditions, the development of new technologies, and the development of transport such as trains, electric cars, etc. In 2017, the report from Sönnichsen (2020) recorded a global consumption of 22.5 trillion kilowatt-hours. Electricity has been produced in different ways using coal, natural gas, and diesel. These solutions unfortunately have severe impacts on the environment. However, environmental awareness is drastically expanding, and many countries, companies, and people are looking forward to sustainable electric production. These solutions take advantage of natural phenomena such as wind, wave, thermal and solar power to convert them into electricity. Renewable energy is more favourable because they are inexhaustible and have the potential to be cleaner. Besides, Europe had set a target for 2020 to reach 20% of renewable energy. However, the recent report from Eurostat (2020) shows that the target has not been reached by 0.3%. For example, Sweden reached 54.6% of renewable energies in 2020 when on the other hand, the Netherlands only reached 7.4%. Hence, the Europe commission continues to move forward with a target of 32% of renewable energies by 2030 (European Union, 2021). Moreover, Sweden aims to have no net emissions of greenhouse gases by 2045 according to the Ministry of the Environment (2018). Outside the European Union, Norway has the highest percentage of renewable energy of 72.8% in total.

Offshore solutions with wind turbines and wave energy converters (WEC) are promising because they would significantly reduce the land space used to produce electricity and would have a minimal impact on human life because of their locations (Kaldellis & Kapsali, 2013). In addition, wave energy has the second-highest potential for electricity production, with a theoretical availability from wave energy is 29500 TWh/year, from which 10-20% could be exploited (Aderinto & Li, 2018). For wave energy converters, the number of studies is rising with promising results. An economic analysis carried out by Astariz & Iglesias (2015) states that a capacity factor could be determined for wave energy converters, the capacity factor being the ratio between average annual energy and theoretical maximum energy. Astariz & Iglesias (2015) further show that this capacity factor could be in the range of 20-45% based on the various operating principles of WEC. Even if these solutions are promising, the electricity transport from the offshore installations to the land remains crucial.

Dynamic subsea cables are cables that transport the electricity produced by offshore installations to onshore installations that redistribute the electricity to cities and facilities. The length of these cables varies depending on the offshore installation location, with the current trend to move furthest from the coast to reach higher efficiency for wind turbines (Kaldellis & Kapsali, 2013). The voltage considered in this case is 1kV since the analysis considers low voltage cables. The cable lifetime is vital

since it directly affects the profitability of offshore solutions. Hence, cables are designed with small stiffness properties in bending and torsion that remove constraints from the cable. In addition, they are designed with high axial stiffness to sustain the main axial loads and protect the cable. The initial design should sustain stresses for 20-25 years (Young, 2019). However, it has been seen that cable failure occurs earlier for various reasons.

Offshore maintenance and repair are inherently costly due to the extreme environment, the sophisticated equipment, and the personnel involved in getting the task completed. The time involved in carrying out these operations is also considerably long attributed to the environment. Most of the repair work or maintenance concerns dynamic subsea cables. Precisely, 80% of offshore wind projects experience a cable-related incident (de Wild, 2018). It has resulted in an average repair cost of around £12.5 million in the UK, with an average repair time ranging from three to five months (Export Cable Reliability Description Concerns, 2017). With the downtime of the wind farm, the total loss has been determined to be around £22.8 million splits approximately between repair cost and lost revenue (Young, 2019). The report from De Wild (2018) shows the number of claims related to the offshore field and emphasizes the importance of dynamic subsea cables.

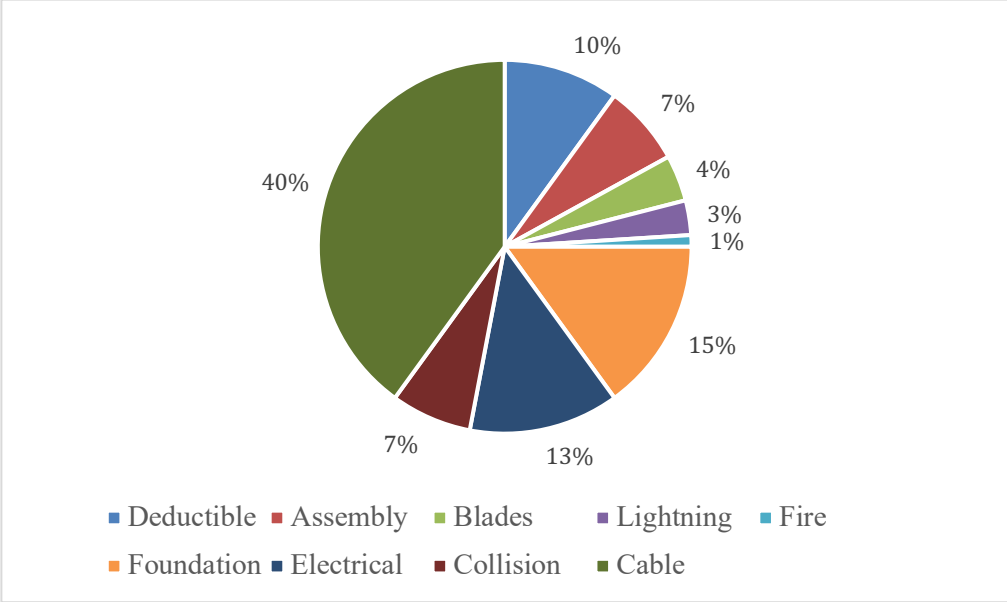

Figure 1.1: Failures claims in the offshore power industry (GCube, 2016)

Cable failures occur mainly due to mechanical damage, water ingress, and overheating. Mechanical damage occurs mainly during the installation process when the cable is vulnerable. An incorrect installation or damage during the process leads to up to 50% of cable failures (Young, 2019). Similarly, mechanical damage can occur during the transportation or the manufacturing processes (Young, 2019). However, their lifetime estimation of around 25-30 years ends abruptly over two to five years. This cause is attributed to a phenomenon called water treeing (de Wild, 2018). It has been found that the process of water treeing or the propagation of water trees is aided by motion-induced and electrical-induced stresses considering the environment in which the dynamic subsea cables are installed and operated. It adds further stress for pre-emptive repair and maintenance to reduce the cost incurred and shorten the downtime of offshore power plants (Young, 2019).

Water trees have a small electrical signature: they cause a slight electrical disturbance which makes them difficult to detect (Young, 2019). Also, water trees are classified into two different categories: vented and bow water trees (Young, 2019). Vented water trees derive from defects that occur at the interface of the two mediums, where they can either grow inwards from the outer surface of the insulator or, they can grow outward from the inner surface of the insulator. The former originates due to age and external damage, and the latter derives from the defects in the conductor manufacturing (Young, 2019). These water trees grow across the insulating material thickness until they reach a critical length corresponding to 60% of the thickness. Then, a dielectric breakdown occurs in the cable (Young, 2019). Also, Young (2019) further points out that the length of the water tree is closely related to the dielectric breakdown rather than the density of water treeing or the ageing of cables. In the case of bow-tie water trees, they form within the insulating material due to impurities. Once initiated, they grow in either direction till they transform into electrical trees (Young, 2019). Once electrical trees are present, they rapidly grow until the insulation layer cannot withstand the applied voltage. Electric trees propagate through the mechanism of partial discharge (PD), which occurs when the dielectric strength of the insulating material is unable to handle the applied electric field (Dissado et al., 1998). This process produces heat which allows the newly formed electrical trees to propagate across the insulator. However, the transformation of the water tree into the electric tree is not necessary for the breakdown of the insulating material (Young, 2019).

1.2 Objectives and goals

The main goal of this thesis is to investigate the water tree propagation. This investigation leads to the calculation of the fatigue life of dynamic subsea cable caused by the presence of water tree. This fundamental goal is composed of three objectives. Two of them concern the water tree propagation through two processes taken independently: motion-induced stresses and electrical-induced stresses. The last objective is to create a final model combining both mechanisms.

The first objective is the study of the motion-induced stresses affecting the water tree propagation. Hence, the cable motions are the most important. The data from a test site and a literature review provide the most frequent sea states which give the cable motions. Then, the next step is to identify critical locations where the cable has the highest damage accumulation. From these locations, the target is to determine the local displacements for one cable segment. The local stresses are determined using these displacements and a FE model in ABAQUS software (2020). Finally, a linear elastic fracture mechanics (LEFM) model taking the output from the simulation determines the water tree propagation and hence, the fatigue life from the motion-induced stresses.

The second objective is the study of the electrical-induced stresses influencing the water tree propagation. The electrical-induced stresses are defined as the Maxwell stresses. A simulation model in COMSOL Multiphysics software (2020) indicates the electric field distribution caused by a water tree. This distribution leads to the calculation of the Maxwell stresses. These stresses provide the water tree propagation and the fatigue life based on the literature review.

The last objective of this work is the development of a combined model considering the motion-induced stresses and the electrical-induced stresses. This model can be created

based on the approaches of the previous objectives. Later, it gives the water tree propagation in the insulation layer and an overall cable fatigue life expectancy.

1.3 Scope, assumptions, and limitations of the study

This section presents the scope of the study. In addition, the assumptions and limitations are also introduced.

1. Understanding water tree by literature study and identifying the limitations and the assumption for the thesis.
2. Extracting hydrodynamic simulation results for a specific state from SIMA software (2020) to determine the motion-induced stresses on the cable, using a linear analysis in ABAQUS software (2020).
3. Building a simulation and analysing the electromagnetic field for a theoretical water tree in COMSOL Multiphysics software (2020) and identifying the Maxwell stresses related to it.
4. Identifying the impact of motion-induced and electrical-induced stresses on the cable fatigue life.
5. Combining the two processes to get the general overview of the water tree propagation and developing a LEFM model to calculate the cable fatigue life.
6. Identifying the variables that could influence water tree propagation and studying them using the previous LEFM model created.

This work aims to give a good understanding of water tree growth in a dynamic subsea cable. Then, it targets the estimation of the cable fatigue life. Hence, some assumptions and limitations have been considered based on papers and simulations to redirect the focus.

The work emphasizes the development of methods for the analysis of propagation of water tree cracks. One example of a dynamic power cable is used in a case study. The cable's insulation material is normally not made of cross-linked polyethylene (XLPE) material which is sensitive to the occurrence of water tree cracks. However, all other material and mechanical properties of this cable were known from former research and the insulation material was in this study substituted to XLPE material to show-case the methods developed in the thesis.

There are temperature variations that could affect the material properties. The heat produced in the core can be high due to the high voltage used. However, the temperature is assumed to be constant over time and, the only concern is the material properties which could depend on the temperature. This last aspect has been also disregarded.

This work assumes that in the cross-section of the insulation, only one water tree can be found. It means that the interaction of multiple water trees in a same cross-section is disregarded. This assumption is reasonable because Hvidsten et al. (1998) explain that the density of water trees in a same cross-section does not affect the electrical breakdown, and only the length of the water tree matters.

The chemical process affecting the water tree growth is a researched subject. It relates to the study of the microscopic fracture of chemical bonds in the insulation layer (Young, 2019). A lot of researchers (Shaw & Shaw, 1984; Xu & Boggs, 1994) found it relevant, when other researchers focused their experimentation more on motion-

induced and electrical-induced stresses (Chen & Filippini, 1993; W. Tao et al., 2016; Z. Wang et al., 2012). The focus of this work is on the motion-induced and electrical-induced stresses; hence the chemical process is not considered.

1.4 Outline of the thesis

Chapter 1 is an introductory chapter that provides an idea of the background, motivation, and aims for this thesis to offer a basic understanding of the study. Chapter 2 gives a literature review about dynamic subsea cables and how it impacts the offshore industry with the different dynamic subsea cables properties. In addition, the degradation of these cables is explained through fracture mechanics, and an explanation of the water tree process is issued. Chapter 3 explains more thoroughly the methodology addressed in this work to determine the impact of the motion-induced stresses and the influence of an electric field on a water tree. Chapter 4 contains the different setups, parameters, and calibrations used both for mechanical and electrical simulations, in addition to the fracture mechanics model. Then, Chapter 5 presents a discussion about the various results from the models explained in Chapter 4. Chapter 6 explains the different results and proceeds them to conclude the work. Finally, Chapter 7 discusses the future work of this thesis and suggests some ideas on how to improve the results of this work.

2 Literature review

This chapter presents main theories and authors which help to understand the subject and carry out the work. First, it introduces the dynamic subsea cables in the offshore industry. Then, details about the wave energy converters are offered, in addition to the explanation of wave energy conversion. Next, all the different parameters and material properties used in this thesis are displayed. Finally, this work presents a theory about the failure in dynamic subsea cables.

2.1 Cables in the offshore industry

The cables are designed with low bending and torsional stiffnesses and high axial stiffness to sustain different sea states and mechanical loads. Hence, they are free to bend without implying high local stresses. Each consists of components such as copper cores, sheathings, and insulation layers. The copper cores transport electricity due to their high conductivity. On the other hand, the insulation layers have very low conductivity and protect the copper cores. They ensure the safety of the cable and make sure that an event of current leakage does not occur. Also, other components are added to the cable to increase the mechanical properties such as Kevlar ropes. Even if there are different cable types, the three-phase cable is the most popular one since it offers better electrical stability with the possibility of using a three-phase delta configuration. A three-phase electrical cable has three conductors insulated.

2.2 Wave energy converter (WEC)

Wave energy converters are one solution to produce electricity without increasing carbon emissions. This solution uses the natural phenomenon of waves to power cities and facilities. The theoretical global potential for ocean energy is estimated to be around 20000-92000 TWh/year (Esteban & Leary, 2012). Hence, this section presents the fundamental mechanism of the conversion and explains the different possible infrastructures.

2.2.1 The technical principle of wave energy conversion

The whole process of converting wave energy into electricity can be divided into three distinct stages (Zhang et al., 2021), as presented in Figure 2.1.

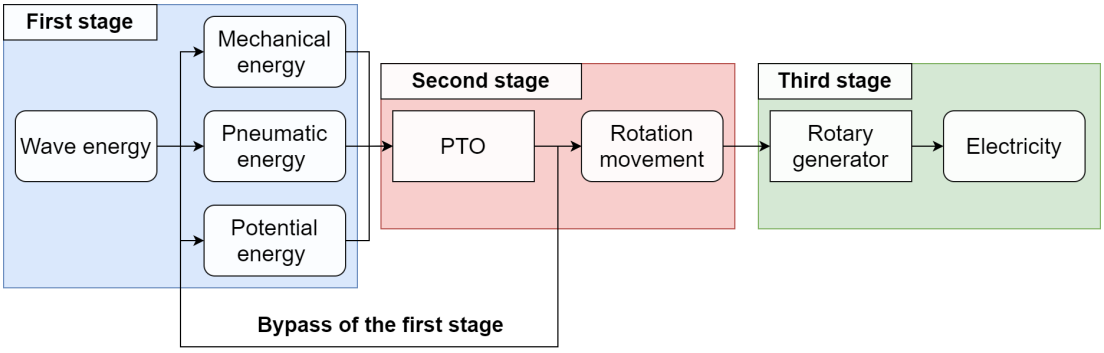

Figure 2.1: Stages of the electric generation from wave energy (data source: Zhang et al., 2021)

The first stage converts the wave energy into mechanical, pneumatic, or potential energy. This stage is achieved with different technologies presented later in the section.

The second stage is the conversion of the energy created in the first stage into useful mechanical energy (Zhang et al., 2021). The definition of useful mechanical energy comes from the potential conversion of this mechanical energy into electrical energy. This conversion is made using a power take-off (PTO) system, converting the energy from the first stage into a mechanical rotation (Zhang et al., 2021). Then, the third stage exploits this rotation provided to produce electricity using a rotary generator. If the direct conversion of the wave energy into useful mechanical energy is possible, the first stage is bypassed (Zhang et al., 2021).

Additionally, a recent overview proposed by Faiz & Nematsaberi (2017) shows the possibility for a direct-drive marine energy conversion between wave energy and electricity production. The principle is to connect magnets to the boy going through coils directly attached to a fixed ground. The vertical translation of the boy along this fixed ground induces the magnets/coils mechanisms to generate electricity due to electromagnetic principles. This solution is promising since it reduces the complexity of the WEC system and lowers the number of conversions that directly affect efficiency (Faiz & Nematsaberi, 2017).

2.2.2 Infrastructures

Falcão (2010) describes the diverse WEC infrastructures then sorts them into three categories: oscillating water column, overtopping, and oscillating bodies. The oscillating water column uses an air chamber with two openings, one connected to a rotary generator and the other connected to the water level. Due to waves, the water surface in the chamber changes and creates an airflow implying the rotation of an air turbine coupled to a rotary generator. The overtopping technology is based on the same principle as the oscillating water column. It exploits a flow created by the variable sea level to produce electricity. However, this technology employs ramps leading to a reservoir fulfilled by the overtopping of the waves crashing on the ramps. This reservoir is directly related to the sea, and the extent of the water level creates a flow. This flow balances the equilibrium between the water sea level and the reservoir's water level. Finally, the oscillating bodies use floating bodies and exploit their movements to produce electricity. Since the oscillating bodies are the solutions considered as most economical, a lot of research has been relying on this technology (Zhang et al., 2021). Czech & Baur (2012) classify the various configurations of these WECs according to the wave direction such as point absorber, terminator, and attenuator. A point absorber is a device that absorbs wave energy in all directions using the vertical displacement of the water surface. On the other hand, the terminator and attenuator absorb the wave energy only in one direction and are composed of multiple segments. The terminator is installed perpendicular to the wave direction, and the attenuator is parallel to the wave direction. Zhang et al. (2021) term the tools used to define their efficiency to rank the different technologies. The energy capture performance index hydrodynamic efficiency HDE characterises the amount of power available from the waves compared to the WEC power production. The index is defined as Equation (1).

$$\begin{cases} HDE = \dfrac{P_d}{P_w D_{WEC}} \\ P_w = \dfrac{1}{32\pi}\rho g^2 H^2 T \end{cases} \tag{1}$$

where P_d is the mean absorbed power, P_w the incident wave power per unit length, D_{WEC} is the width of the device, ρ is the seawater density, g is the gravity constant, H is the wave surface elevation, and T is the wave period.

In their report, Zhang et al. (2021) show several converters tested in actual sea conditions and present their respective capacity and HDE. From this data, the point absorber has an HDE between 20-40%, with a capacity between 250-1000kW. The attenuator has an HDE between 8-15%, with a capacity between 160-750kW. Finally, the terminator has an HDE between 40-45%, with a capacity between 250-315kW.

2.3 Dynamic subsea cables properties

This section defines the different mechanical and electrical cable properties used in this work. It also specifies the various friction coefficients between the components of the cable. The focus of this work has been to identify the mechanical and Maxwell stresses in the insulation layer made of cross-linked Polyethylene called XLPE.

2.3.1 Mechanical properties

The global mechanical properties of the cable defined in Table 2.1 are based on the study by Yang (2018). This study concerned the RJIT Chalmers cable. Later, the calculation of the global loads along the cable length uses these properties.

Table 2.1: Global mechanical properties of the dynamic subsea cable (Yang, 2018)

Parameter	Symbol	Value	Unit
Cross-sectional outer diameter	D_{Cable}	0.038	[m]
Mass	M_{Cable}	2.3	[kg/m]
Axial stiffness	EA_{Cable}	4.7	[MN]
Bending stiffness	EI_{Cable}	5	[Nm^2]
Torsional stiffness	GK_{Cable}	3	[Nm^2/rad]

The material properties of the XLPE are presented in Table 2.2 according to Granta EduPack software (2020).

Table 2.2: Mechanical properties of the cross-linked Polyethylene (XLPE) insulation (Granta EduPack software, 2020)

Parameter	Symbol	Value	Unit
Density	ρ	920 - 1240	[kg/m^3]
Young's modulus	E	0.537 – 0.564	[GPa]
Yield strength	σ_Y	8.27 – 13.8	[MPa]
Tensile strength	σ_T	10.3 – 21.4	[MPa]
Compressive modulus	B	0.537 – 0.564	[GPa]
Compressive strength	σ_C	9.92 – 16.6	[MPa]
Shear modulus	G	0.188 – 0.197	[GPa]
Poisson's ratio	ν	0.431 – 0.433	
Fatigue strength at 10^7 cycles	N_f	4.12 – 8.56	[MPa]

In this thesis, it has also been necessary to look into the different friction coefficients between the components, as shown in Table 2.3. The friction characteristics determine the interaction between the cable's components and thereby its overall global characteristics.

Table 2.3: Friction coefficients for different material combinations

Material combination		Condition	Static	Reference
Polyethylene	Polyethylene	Clean and dry	0.2	Engineering ToolBox (2004)
Nylon	Nylon	Clean and dry	0.15-0.25	Engineering ToolBox (2004)
Nylon	Polyethylene + Polyurethane	Clean and Dry	0.3	Assumption
Polyethylene	Polyurethane	Clean and dry	0.3	Assumption
Copper	Polyethylene	Clean and Dry	1	Assumption

A thin layer of Nylon protects the Kevlar ropes. Then, the mechanical properties of these ropes do not change. However, the friction coefficient is set as 0.3 when in contact with Polyethylene and Polyurethane. This choice has been made because the friction coefficient between Nylon to Nylon is around 0.2 and Nylon to Steel is 0.4. The lack of data for the friction coefficient between Polyethylene and Polyurethane led to the assumption that this friction coefficient is the same as the friction coefficient between Nylon and Polyurethane. Finally, during the manufacturing, all the conductor is shrunk, and penetration of the Copper in the insulation is possible. Due to this characteristic, a full-stick condition has been assumed between Copper and Polyethylene, and the friction coefficient is 1.

2.3.2 Electrical properties

The different electrical properties used in this thesis for the XLPE and the Copper have been taken from Young's (2019) work and are shown in Table 2.4.

Table 2.4: Electrical properties of the materials used (Young, 2019)

Material	Parameter	Symbol	Value	Unit
XLPE	Electrical conductivity	κ_{XLPE}	$1e^{-17}$	[S/m]
	Relative permittivity	ε_{rXLPE}	2.3	[-]
Copper	Electrical conductivity	κ_{Cu}	$9.33e^{6}$	[S/m]
	Relative permittivity	ε_{rCu}	1	[-]

2.4 Degradation of dynamic subsea cables

This section explains the degradation of dynamic subsea cables through different principles. The fracture mechanics include the crack propagation from the mechanical stresses and the water tree process, which introduces the electric field as a principal factor of the failure mechanism in dynamic subsea cables. Moreover, this thesis aims to study the superposition of mechanical stresses combined with Maxwell stresses. This task has been carried out only a few researchers studied this superposition.

2.4.1 Fracture mechanics

Fracture mechanics is the study of cracks in structure materials. It implies the investigation of static loads or cyclic loads that could lead to failure in a material. Static loads correspond to loads that do not vary or have a low variation over time. Cyclic loads stand for loads that are repeated over time with different amplitudes. An example of cyclic loads is vibrations (Dowling, 2013). Fracture mechanics is divided into two principal theories: linear elastic fracture mechanics (LEFM) and elastic-plastic fracture mechanics (EPFM). LEFM is defined when the deformation of the material due to the loads stays in the elastic zone and small-scale yielding of the zone near the tip of the crack is fulfilled. This thesis follows the assumptions of LEFM as recommended by Young (2019), whoever, its validity must be verified later, based on the maximum stresses and material response near the crack tip.

The usage of LEFM requires calculation of the stress intensity factor. The stress intensity factor is defined for three modes of crack propagation. Mode I is the opening mode, mode II is the shearing mode, and mode III is the tearing mode, as shown in Figure 2.2.

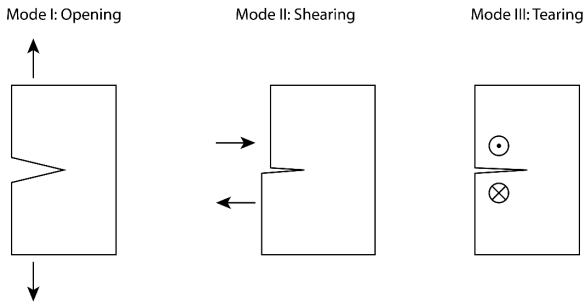

Figure 2.2: Different modes of crack opening and growth

This thesis focuses only on mode I due to the geometry of the cable and the loads applied. Mode II requires important torsional moments and shear stresses. That is not encountered in this case due to the mechanical properties of the cable.

Based on the LEFM theory, the crack growth by cycle can be established by Paris' law equation shown in Equation (2).

$$\frac{da}{dN} = C(\Delta K)^m \tag{2}$$

where $\frac{da}{dN}$ is the crack growth by load cycle, C and m are material constants, and ΔK is the stress intensity factor range.

2.4.2 Fatigue life and fatigue crack growth equations

The SN-approach together with the rainflow counting method have been used to identify the location along the cable where the largest fatigue damage is accumulated. Fracture mechanics applied to polymer materials has been studied by e.g. Radon (1980). This subchapter gives a brief summary of these methods.

2.4.2.1 Rainflow counting

The motions-induced loads on the cable are cyclic. The rainflow counting method has been used to calculate the number of load cycles and stress amplitude for the fatigue damage accumulation calculation. The principle is to take the stress history described with peaks and valleys and extract cycle ranges; see Figure 2.3 for a schematic.

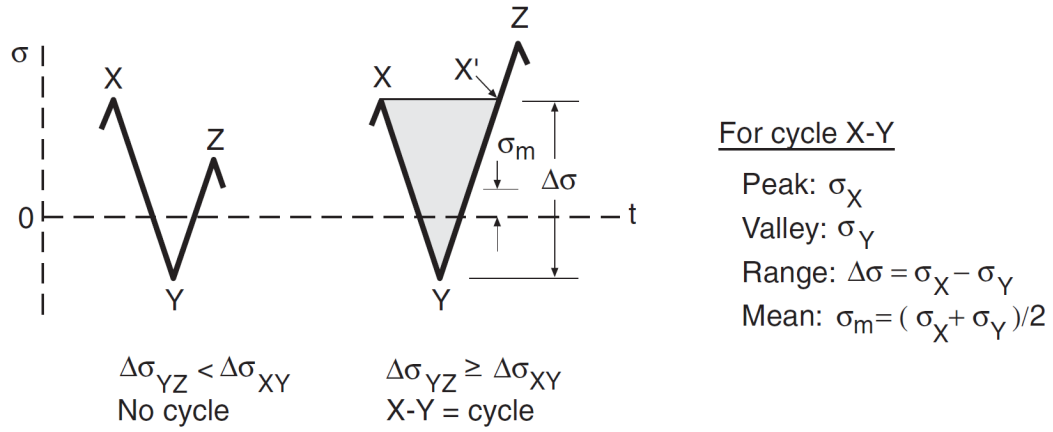

Figure 2.3: Condition for counting a cycle with the rainflow method (Dowling, 2013)

X, Y, and Z points represent each peak/valley. There is a cycle when the stress range between points Y and Z is higher in amplitude than the stress range between points X and Y. This cycle has then the value of the stress range between points X and Y (Dowling, 2013). Hence, the rainflow cyclic counting extracts the ranges cycles over a stress history.

2.4.2.2 SN-curve approach

The SN-approach is a phenomenological method which does not follow the growth/propagation of a crack. It is often used to identify fatigue-critical locations of a structure or component. It belongs to the category of total-life approaches where experiments must be carried out to define what fatigue failure is once the fatigue life has been reached (according to the numerical model). In the SN-approach, elastic stress response is assumed.

2.4.2.3 Damage accumulation

The SN-approach and rainflow counting method are often combined using the Palmgren-Miner partial fatigue damage accumulation rule. The principle uses the SN-curve as a tool to calculate the fatigue damage of each stress range, and when the damage accumulation reaches its critical value, then the material is assumed to fail. The critical value is defined as 1. Finally, the damage accumulation is defined in Equation (3).

$$D = \sum_{i=1}^{k} \frac{n_i}{N_i} \tag{3}$$

where D is the damage accumulation, k is the number of cycles at a given stress range, n_i is the number of occurrences of that stress range, N_i is the number of cycles to failure according to the SN-curve for the same stress range.

2.4.3 Water tree

Dynamic subsea cables are crucial components in the offshore industry, and their service life is the main factor of their development. It is because maintenance and repair in the offshore industry are difficult to arrange and also expensive. It emphasizes the need to have fewer cable defects to increase the service life for dynamic subsea cables and the profit of this solution. A fundamental aspect that affects their life is a phenomenon called water tree (Crine, 1998). Water trees are dendritic pathways formed in Polyethylene and cross-linked Polyethylene (XLPE) insulation layers in dynamic subsea cables due to electric stress and water immersion. This phenomenon is found mainly in the XLPE parts of these cables (Tanaka et al., 1976). One of the common ways for water to enter the Polyethylene is during the steam curing to produce the cross-linked structure of the XLPE. An amount of 2000-3000 ppm is absorbed in the region during this process (Tanaka et al., 1976). The presence of a water tree causes a drastic reduction in the dielectric strength of the insulating material. In addition, the density of water trees formation does not affect the dielectric strength rather the length of the water trees (Hvidsten et al., 1998). It has been found that critical loss in dielectric strength occurred when the water tree length reached 60-80% of the insulator thickness, according to Hvidsten et al. (1998). Another way in which the water enters the insulating material is by diffusion process or field-assisted diffusion. The formation of water trees is considered to be following the diffusion process. It is speculated that the water content, especially in steam cured XLPE, is approximately 1 wt.%, with the number of voids approximated to 107 (or 1010) with inter void distance of 50 (or 20) μm, assuming that each void has a size of 10 (or 5) μm. If the water occupies more than 20% of the voids present in the cable, an opaque ring will be seen in the cross-section. It will then disappear if left for too long in the atmosphere. However, this water remains, and more water is likely to enter if water exists outside the cable insulation similar to a submerged state, which is crucial in this work (Tanaka et al., 1976).

Water trees are classified into two broad categories bow-tie tree and vented tree. Bow-tie trees grow within the XLPE layer due to impurities or defects and develop in opposite directions (Young, 2019). The high electric field located at the tip of these water trees can eventually lead to the formation of electric trees. Then, they rapidly grow and weaken the XLPE layer till the dielectric strength is lost (Young, 2019).

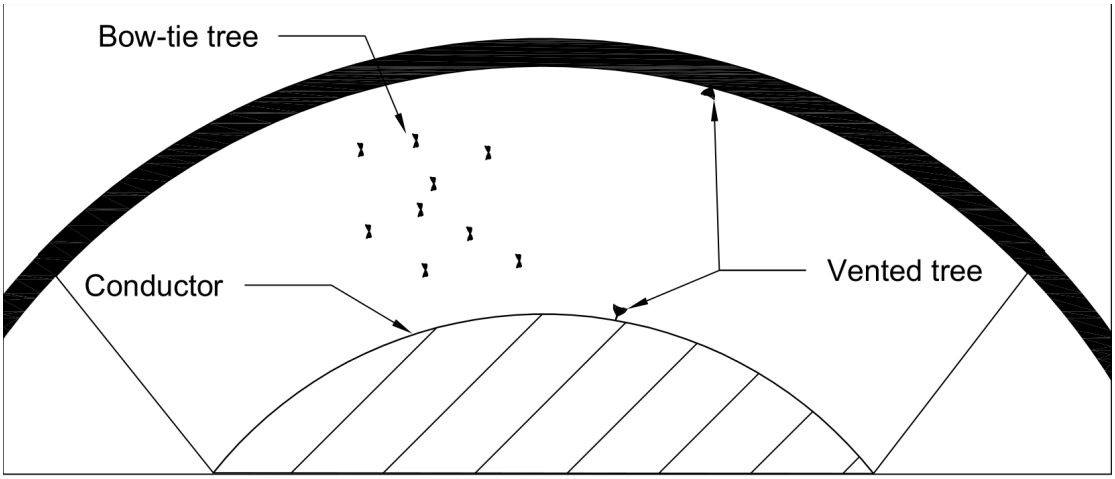

Figure 2.4: Schematic of vented and bow-tie water trees (data source: Young, 2019)

On the other hand, vented trees develop due to the impurities present at the interface of the two layers. They can expand at the conductor XLPE boundary due to defects in the conductor and grow outwards, or they can progress from the outer surface of the XLPE due to external factors and ageing (Young, 2019).

2.4.3.1 Water tree propagation

The development and growth of the water tree are affected by the electric field concentration at the tips of the water tree branches. This electric field concentration generates a frequency-dependent Maxwell stress along a fixed direction (Hvidsten et al., 1998). When the water molecules in the microvoids are exposed to these time-varying electric fields, they can be micro jetted toward a fixed direction (Crine, 1998). When a vented water tree grows from the conductor XLPE interface as it grows outwards, it experiences a reduction in the electric field that halts its growth. In the case of a water tree growing from the outer edge of the XLPE inwards, the electric field concentration increases as it advances further, promoting the water tree growth. Hence, these are the most dangerous water trees and may lead to the breakdown of the insulating material (Young, 2019). On the other hand, bow-tie water trees rarely develop to the extent where they cause dielectric breakdown (Young, 2019). However, once the bow-tie water tree grows to a sufficient size and develops into an electrical tree, it leads to rapid failure of the XLPE insulation.

2.4.3.2 Water tree geometry

The geometry of the water tree is dependent on many factors such as the electrical stress, frequency of the voltage, water content and the voltage applied (Young, 2019). Hvidsten et al. (1998) explain that the geometry of the water consists of ellipsoidal cavities connected by a narrow channel, as shown in Figure 2.5. However, this geometry of the water tree is invisible in the absence of voltage. Hvidsten et al. (1998) explain that the reason for this is when water exits the channels, the channels collapse and hence, make the water tree invisible.

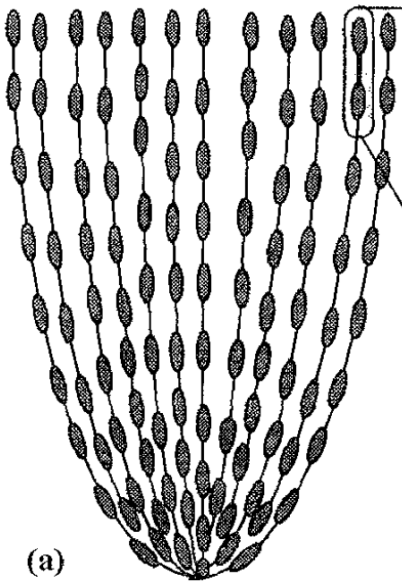

Figure 2.5: Pearl and string structure (Hvidsten et at., 1998)

When DC voltage is applied, the water slowly fills the channels due to the Maxwell forces that drive them. However, when an alternating current is applied, the steady current flows through this causes losses due to which water intrusion remains low (Young, 2019). However, as the applied voltage increases, the channels slowly start to fill (Hvidsten et al, 1998). Thus, making the water tree visible with a pattern similar to that of string and pearls. Here r represents the radius of the channel between the two ellipsoid structures each having a longitudinal axis of 2 µm.

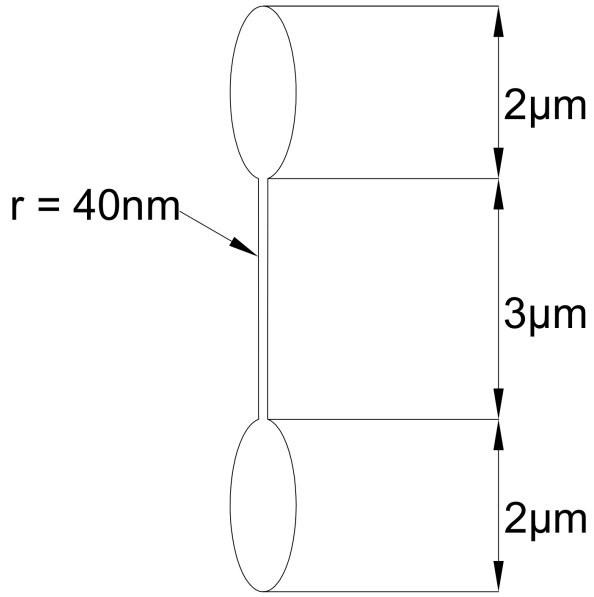

Figure 2.6: Water tree geometry (Hvidsten et at., 1998)

3 Methodology

This chapter presents the methodology in the thesis. The first section presents the procedure for the calculation of the motions-induced mechanical stresses. Then, the second section covers the approach employed to calculate the Maxwell stresses. The last section details the assessment of the fatigue life estimation.

3.1 Study case

For the study case, the cable used for the analysis in this study is the Chalmers RJIT cable. The reason for this selection is the extensive data available. It has a length of 126 meters and is connected to a wave energy converter and a hub. The mechanical and electrical properties of the cable are explained in Section 2.3. In addition, it has a global diameter of 38 mm, and its geometry is detailed in Figure 3.1.

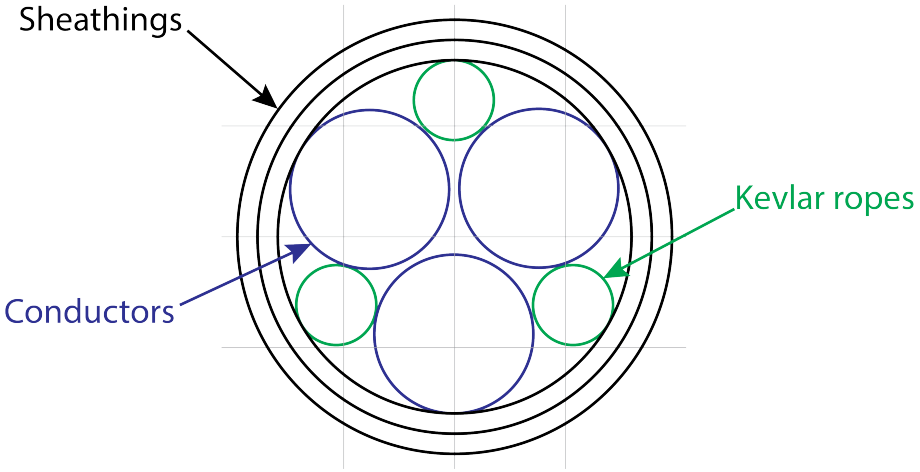

Figure 3.1: Sketch of the main geometry of the Chalmers RJIT cable (data source: Kuznecovs et al., 2019)

The cable is divided into a few components. The components at the middle in blue are the three conductors with a layup angle of +3.1°. The three smaller components in green are Kevlar ropes that provide good mechanical properties for the cable and allowing it to sustain loads, with a layup angle of +4.5°. Finally, two distinct sheathings in black are covering all this cable to make it as a whole. The conductor is divided into 19 concentric strands, each divided into 36 concentric wires covered by an insulation layer of Polyurethane. For the electrical model, it has been assumed that the wires and strands are a homogenous solid.

Table 3.1 shows the main dimensions used in this thesis for the insulation and the conductor.

Table 3.1: Main dimensions of the conductor and insulation layer

Cable Component	Dimensions
Conductor radius	5.45 mm
XLPE thickness	1.76 mm

3.2 Calculation of mechanical stresses

In this thesis, the focus has been to determine the stresses in the XLPE insulation layer to estimate the fatigue life of the dynamic subsea cables. These cables are subject to axial, bending, and torsional loads due to their environment. It is not possible to locally simulate in detail the stresses in the insulation layer along the cable's full length due to its long length. Hence, the use of the sub-modeling method developed by Ringsberg et al. (2000) is needed. This method consists of simulating the global stresses and displacements along the length of the cable using its mechanical properties, then creating a local model with a higher resolution on which are applied the stresses or displacements from the global model.

As showed in Figure 3.2, the global model is defined to determine the displacements along the cable to be used in a local FE model in ABAQUS (2020). The local model is more detailed than the global model, and its length is shorter. It allows identifying the local stresses in the XLPE that specifies the stress history and then the fatigue life of the insulation.

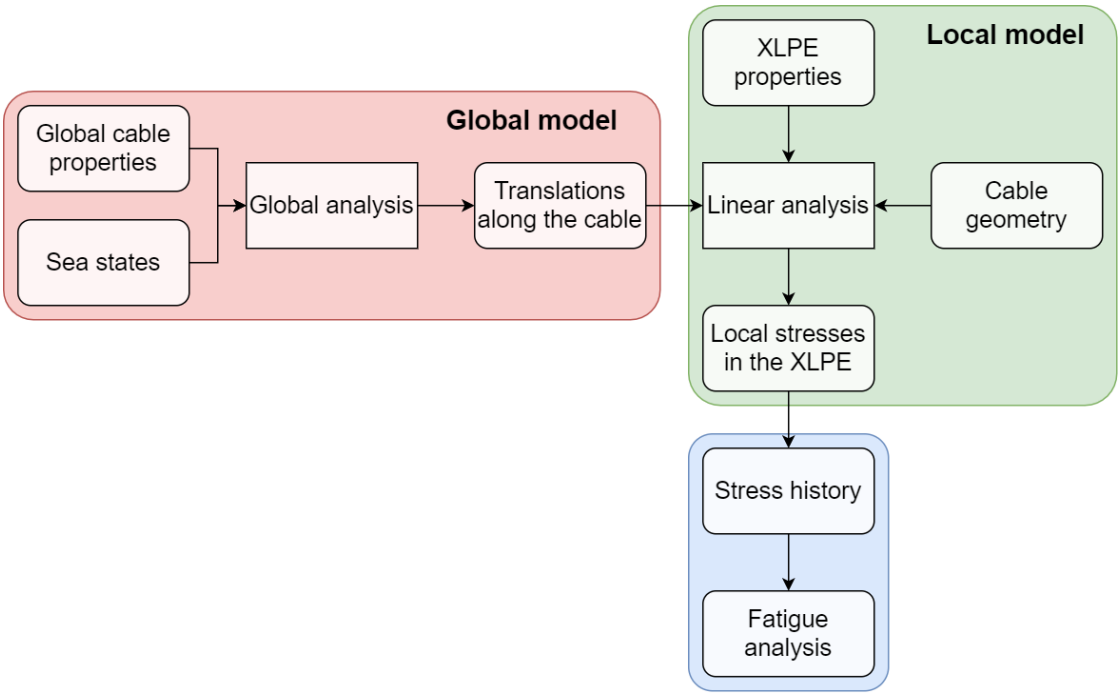

Figure 3.2: Flowchart of the mechanical analysis

3.2.1 Global assessment of the mechanical stresses in the cable

The global assessment of the mechanical stresses along the cable is carried out in SIMA (2020), a module from SESAM software (2020) developed by DNV. The data from SIMA (2020) is then extracted and used as boundary conditions for the local model. Figure 3.3 shows the different steps of the global assessment that are explained more in detail in this section.

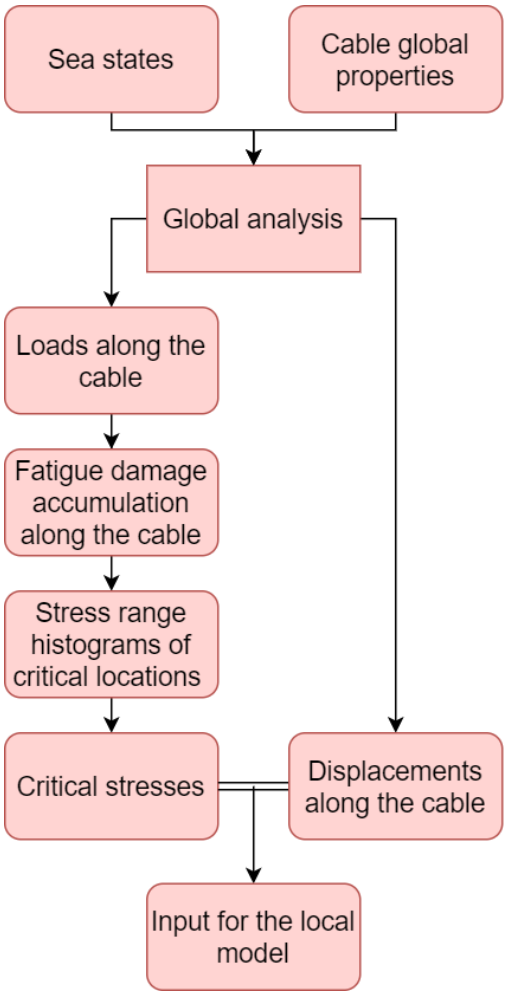

Figure 3.3: Methodology for the global assessment of the mechanical stresses in the cable

3.2.1.1 SIMA (2020) analysis

SIMA (2020) is used for the analysis of marine operations and mooring lines. SIMA (2020) allows the modelling of mooring lines and computes the displacements and loads according to a specified sea state. In SIMA (2020), the wave energy converter motion is simulated, and its cable has been defined with the mechanical properties defined in Section 2.3.1. The selection of the different sea states is explained later in the thesis.

3.2.1.2 Extraction of the data

It is crucial to identify the outputs from SIMA (2020) to progress from the global to the local scale. Hence, the stresses and displacements along the length over the time of the simulation have been extracted. From SIMA (2020), it is possible to get these outputs as Excel files or binary files. Since the simulation time is significant and there are many outputs, the choice has been made to use the binary files since the extraction is faster

and easier than Excel files. Also, the use of binary files makes the exploitation faster since automation can be made using MATLAB (2020). Hence, a script was written to read the binary files and save the outputs as *.m files. The results of these outputs have been verified using these Excel files.

3.2.1.3 Choices of the location

Once the data is extracted, the different sea state scenarios determine the critical locations of the cable using a fatigue code developed by Yang (2018). This code allows determining the SN-based fatigue damage accumulation (FDA) over the cable length for the global model.

The ideal solution is to implement in ABAQUS (2020) all the different steps from the stress history to determine the fatigue damage accumulation (FDA) in the insulation layer. However, due to computation issues and time, the choice has been made to select some load steps to create a stress history. Then, using the fatigue code developed by Yang (2018), it is possible to determine the critical locations of the cable where the FDA is the highest. One or two locations have been selected depending on the sea state condition. From these locations, a histogram of the stress ranges helps to define the best load cases.

3.2.1.4 Histograms and load choices

Each histogram of the stress ranges has been plotted using the function *histogram* in MATLAB (2020). The highest stress range was selected as the first load case to check if the sea state could propagate a physical initial crack in the insulation material. Depending on the results, the other stress ranges are chosen. If the highest stress range shows that the load is not large enough, then the sea state case is assumed to have no impact on the fatigue life of the insulation.

3.2.1.5 Extraction of the displacements

Once the stresses have been chosen, it is possible to extract the translations along the three directions. Using an in-house MATLAB (2020) code, it is possible to detect the time of the stresses used in the stress range and then determine the translations using the time step and the position along the cable.

3.2.2 Local assessment of the mechanical stresses in the XLPE

The local assessment of the mechanical stresses in the XLPE dwells on creating an FE model in ABAQUS (2020) and running the simulations using the boundary conditions found later with a more detailed procedure of the model implementation. The choices about the creation of the model are defined later in the thesis.

The local stresses are calculated the FE software, with the assumption of linear analysis. This assumption is needed later in the thesis because the Paris' law is adopted to determine the fatigue life. By defining the global properties of the cable and specifying a sea state (Period, Wave height, etc.), the forces, moments, translations, and curvatures can be disposed of using the methodology explained in Section 3.2.1. An application of the displacements as translations and curvatures ensures that all the components are moving together. Hence, it allows the determination of the stresses in the various parts and the XLPE insulation. In addition, the curvatures are a consequence of the rotations

in the three directions so, it is not necessary to force the curvatures. Instead, translations are used only with the three displacements degrees of freedom.

The local model is carried out in ABAQUS (2020) using first a model as close to reality as possible. As described by Ringsberg et al. (2000), one end of the cable should have a fixed boundary condition while the translation should be applied on the other one. In addition, a simple contact-to-contact condition has been implemented to allow collision and friction. The friction coefficients between the different components of the cables are yet to be investigated. Even if Table 2.3 shows the friction coefficients between the materials, the initial shrink of the cable could lead to a full-stick condition. Hence, an investigation of the influence of the friction coefficient is carried out later in the thesis.

The results from ABAQUS (2020) give local stresses in the XLPE. However, the boundary conditions affect the results close to where they are applied. The fixed boundary condition could prevent the cable to shrink since all displacements are locked. Thus, the results are captured at the middle of the model's length to avoid influence from the boundary conditions.

There is a need of extracting the axial and bending stresses in the insulation to determine the crack propagation. The only convenient value from ABAQUS (2020) is the axial stresses in the middle cross-section along the length of the segment defined as S33. S33 is the axial stress in the cross-section required for the crack propagation in Mode I. This stress is expected to be a gradient along the cross-section width or height, as shown in Figure 3.4.

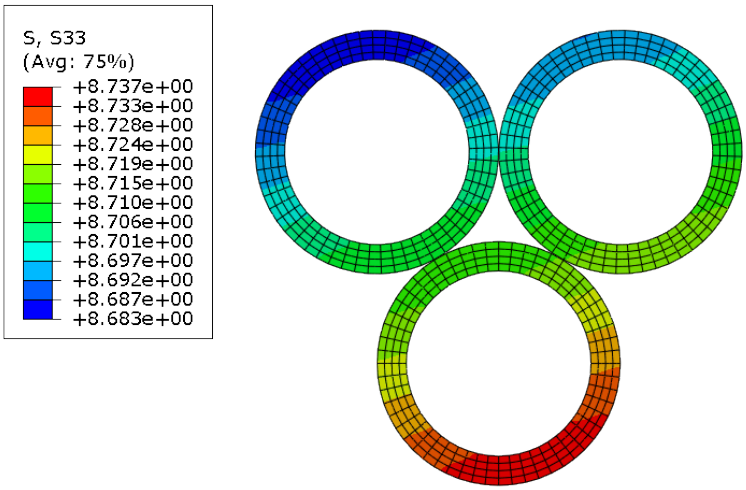

Figure 3.4: Example of an expected result from ABAQUS (2020)

This difference between the maximum and minimum would result in the determination of the bending stress defined as Equation (4).

$$\sigma_{bending} = \frac{\sigma_{max} - \sigma_{min}}{2} \tag{4}$$

The axial stress can be then determined from Equation (5).

$$\sigma_{axial} = \sigma_{max} - \sigma_{bending} = \sigma_{min} + \sigma_{bending} \tag{5}$$

3.3 Calculation of Maxwell stresses

This thesis analyses two distinct factors that aid the growth of water trees. This section explains the method of electrical analysis along with the procedures used for carrying out this analysis.

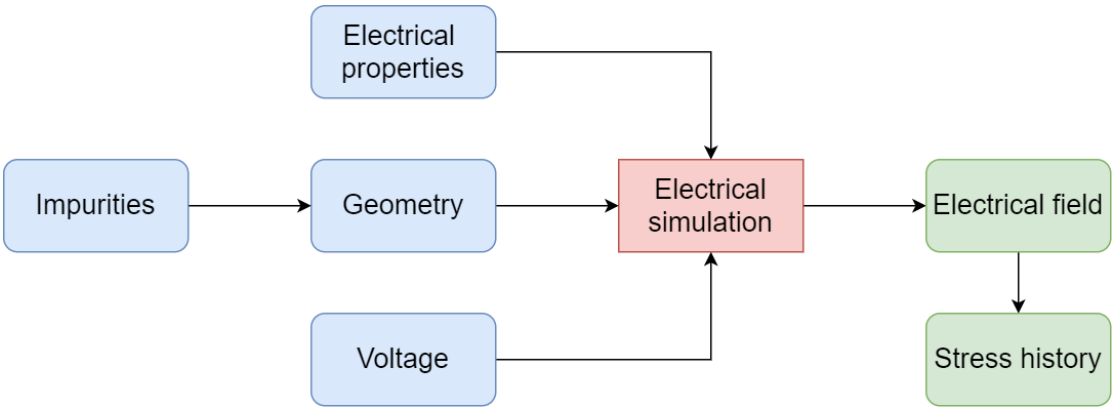

Figure 3.5: Electrical methodology

The outline of the electrical-induced stresses methodology is inspired by the work of Young (2019). Figure 3.5 presents the methodology of this thesis. The cable component of interest for the electrical factor is the insulating layer of cross-linked Polyethylene (XLPE) because it is the component submitted to water tree presence. Hence, the focus is to investigate the electric field generated in this component due to the current flow and the subsequent Maxwell stress.

3.3.1 Impurities

The impurities considered for the study have the properties of seawater to produce the most realistic results. Table 3.2 specifies these properties. The impurity properties are similar to seawater properties since the introduction of water molecules is through diffusion from the surrounding environment, in this case, seawater.

Table 3.2:Electrical properties of the seawater

Properties	Value
Conductivity	$1 \cdot 10^{-4}$ S/m
Relative Permittivity	10

The shape of the impurity is an elliptical shape to get as close as possible to the real-life pearl and string structure mentioned in section 2.4.3. The dimensions of the water tree impurity introduced are also the same as stated in the said section.

3.3.2 Simulations

The electrical model simulations associated with the thesis are carried out in the COMSOL Multiphysics software (2020) using the AC/DC module. The simulations are initiated by designing the model geometry with dimensions specified in Table 3.1. This step is followed by assigning the properties associated with each component.

Two models are developed for two different sets of simulations. One has the impurity present and the other without the impurity. The physics associated with the simulation is chosen as the electric current (EC) module in COMSOL Multiphysics software (2020). The next step is to select the locations for the grounding of the cable and the application of the voltage. It is then necessary to understand which properties of these materials will influence the results, hence, conduct a sensitivity study to evaluate the conductivity and the relative permittivity.

The next step in the simulation process is to carry out the mesh convergence analysis. For this, it is necessary to find which portion of geometry is crucial, identifying the tip of the water tree in the case where the water tree is present. Hence, the mesh around the water tree tip must be finer than in the remaining regions since the electric field concentration at the water tree tip is of interest for the study. In case the water tree is not present, a relatively coarser mesh can produce reliable results.

To understand the results from the COMSOL Multiphysics software (2020) simulations, the normal electric field is selected as the solution set. After obtaining the radial distribution of this normal electric field, this data can be used for calculating the Maxwell stress and onto the life expectancy of the cable.

3.3.3 Electric field and Maxwell stresses

The concept of the electric field is one of the basics in the branch of electromagnetism. It states that any positive or negative charge has an electric field accompanying it. The presence of this field dictates that work is needed to move a charge from one point to another of differing potential. It is known as potential difference or voltage. This moving charge is called a current which produces an accompanying magnetic field (Young, 2019). In this case, the distribution of electric field around the cable with the XLPE encompassing it. This should be uniform considering that the XLPE is evenly distributed around the cable core (Young, 2019).

Using Coulomb's law, the electric field can be calculated from Equation (6).

$$E = \frac{V}{4\pi\varepsilon_0\varepsilon_r r^2} \tag{6}$$

where E is in Vm^{-1} i.e., Volts per meter, and the radius r is in the meter the voltage applied in the simulation is 1kV. ε_0 is the permittivity of vacuum with a value of $8.85\cdot 10^{-12}$ and ε_r is the relative permittivity of the material as specified in Table 2.4.

The application of an AC voltage causes the development of the associated Maxwell force that imposes stress on the cable component. Since the AC voltage is cyclic, the associated Maxwell stress is also cyclic (Young, 2019). Equation (7) formulates the associated Maxwell stress.

$$F = \frac{\varepsilon_0}{2}(\varepsilon_r - 1)\nabla E^2 \tag{7}$$

where F is the Maxwell stress in Pa, ε_0 is the permittivity in vacuum Fm^{-1}, ε_r is the relative permittivity of the material XLPE and E is electric field strength in Vm^{-1}, ∇E is the partial differentiation of electric field E with respect to distance r.

3.4 The growth model of water tree

The growth model of water must include both models from Maxwell stresses and mechanical stresses. First, it is needed to identify the influence of these models on the propagation to determine if one of the models is predominant over the other. If it is the case, then the need of developing a growth model of a water tree using both models is negligible. Otherwise, the crack propagation should be assessed by combining the two models. Once the propagation frequency is determined for both models, the faster model defines the time increment. For each increment, the crack propagation of the faster model is implemented. Then, the slower model is incremented every time a cycle is passed. However, the electrical frequency of the electrical-induced stress is known and is about 50 Hz. The mechanical frequency of the motion-induced stress is assumed to be slower and, as an example, taken as 17 Hz. Hence, Figure 3.6 explains the procedure above. The black arrow represents the time when the different lines represent the models. Based on this figure, the selected increment is the time increment between two green steps since the green steps are the faster model. From the start, there are two steps without passing a slower model step. Then, two increments of the faster model are realised. However, after the third step, it would have passed one of the slower model steps. Hence the third increment would take into account the crack propagation of both models. It is also possible that a step covers at the same time both models. An example is shown in the purple line, where a step from both models happens simultaneously. Section 4.3 explains the mechanical growth model adopted for this work.

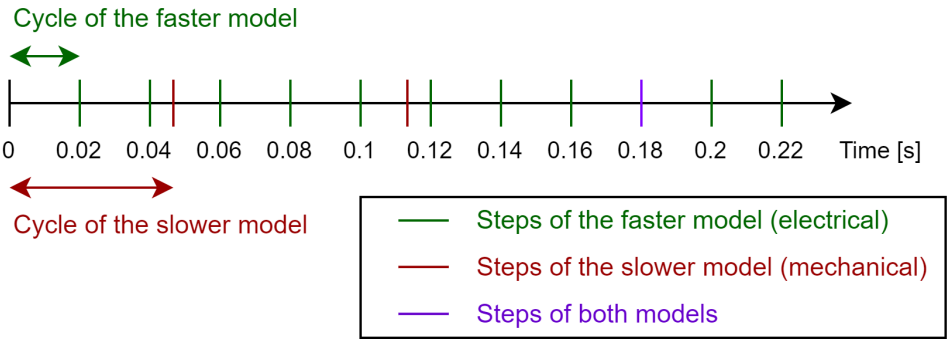

Figure 3.6: Method of incrementation of the fatigue damage for a cable

4 Numerical simulations

In this chapter, the different parameters for the mechanical and electrical simulations are investigated and discussed. This section helps as a reference for all the results found in Section 5. First, the analysis of the mechanical stresses is carried out for the models considered and the parameters of the models. Then, the electrical part explains the mesh convergence analysis with the different sensitivity analyses. Finally, the last subsection describes the various fracture models that could have fit the work and provide a comparison to select one of them.

4.1 Analysis of mechanical stresses

4.1.1 Sea states selection

The test site for the wave energy converter system studied in this thesis is located near Runde in Norway where the data in Figure 4.1 shows the probability of occurrence for different sea states.

H_s [m]	T_z [s]														Sum
	2.5	3.5	4.5	5.5	6.5	7.5	8.5	9.5	10.5	11.5	12.5	13.5	14.5	15.5	
12.5	0	0	0	0	0	0	0	1	2	3	0	0	0	0	6
11.5	0	0	0	0	0	0	0	2	7	0	0	0	0	0	9
10.5	0	0	0	0	0	0	0	11	10	0	0	0	0	0	21
9.5	0	0	0	0	0	0	6	42	10	0	0	0	0	0	58
8.5	0	0	0	0	0	2	29	87	2	0	0	0	0	0	120
7.5	0	0	0	0	0	14	107	103	2	0	0	0	0	0	226
6.5	0	0	0	0	0	44	267	33	5	1	0	0	0	0	350
5.5	0	0	0	0	7	166	337	37	7	2	0	1	0	0	557
4.5	0	0	0	0	43	558	136	32	14	5	1	1	0	0	790
3.5	0	0	0	1	371	563	123	48	19	6	2	1	0	0	1134
2.5	0	0	4	179	877	303	130	71	33	16	7	2	0	0	1622
1.5	0	0	221	1014	501	220	146	110	66	36	16	3	1	0	2334
0.5	644	367	684	248	107	142	162	192	117	64	19	22	3	4	2775
Sum	644	367	909	1442	1906	2012	1443	769	294	133	45	30	4	4	10002

Figure 4.1: Wave scatter diagram at the Runde test site (Yang et al., 2018)

This figure has only two parameters as the wave height and the wave period. For the rest of the work, the current and the wind speed have been neglect despite their potential influence. The lack of data caused the impossibility to take into account these parameters. In addition, the localisation of the test site makes the wave direction to be either 0° or 90°, according to Figure 4.2.

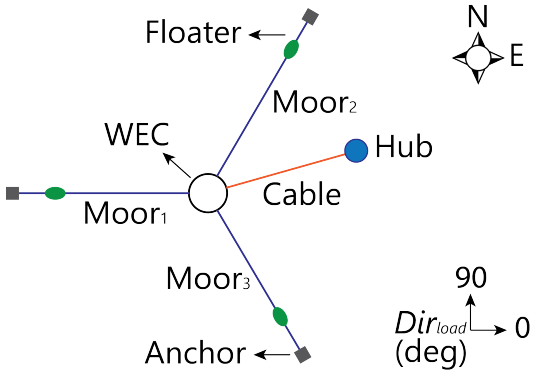

Figure 4.2: Wave direction according to the setup at Runde (data source: Yang, 2018)

Since Yang (2018) shows that 0° is the highest probability of occurrence, only this case is considered in this work. From Figure 4.1, the sea states selected with the highest probability of occurrence are presented in Table 4.1.

Table 4.1: Sea state occurrence for the site of Runde in Norway (Yang, 2018)

Sea states	Hs [m]	T [s]	Probability [%]
1	1.5	5.5	10.14
2	2.5	6.5	8.77
3	0.5	4.5	6.84
4	0.5	2.5	6.44
5	3.5	7.5	5.63
Accumulated probability			37.82

The sea states 3 and 4 have very wave height, and then it is most likely that the states would not propagate the crack. Then, this work focuses on sea states 1,2, and 5. If sea state 1 shows results with high crack propagation, then sea states 3 and 4 would be investigated.

4.1.2 Model choice

The model has been created using ABAQUS (2020). Due to the mesh in SIMA (2020), the segments of interest are 700 mm long since it corresponds to the length between two nodes. Hence, it has been chosen to make a model of the same length with solid elements. As shown in Figure 4.4, the model of the wires and strands is an equivalent solid shape to reduce the computation time despite accuracy. Modelling all the wires for all strands implies too many surfaces in contact that slows the computation. In addition, there is a twist of the components around the centre of the cable called layup angle. Equation (8) defines the length required for a complete rotation.

$$L_{lay} = \frac{2\pi R_{lay}}{\tan(\alpha_{lay})} \tag{8}$$

where, L_{lay} is the length for a complete rotation, R_{lay} is the radius considered from the centre to the cable to the centre of the component and α_{lay} is the angle between the axial baseline of the cable and the axial baseline of the component.

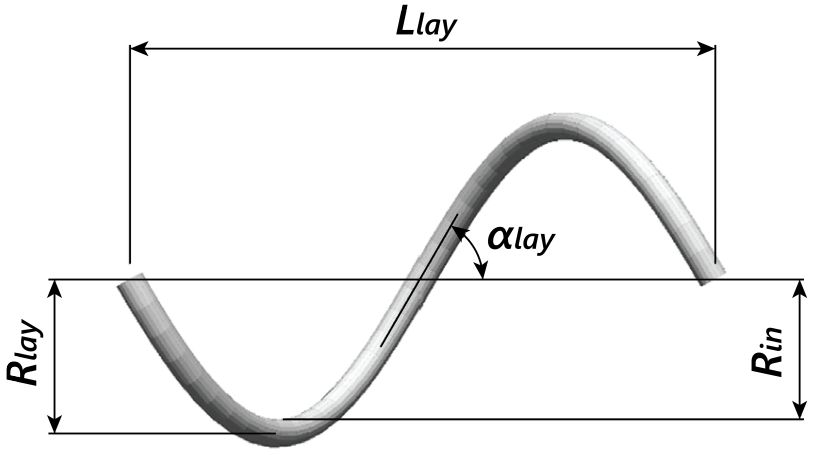

Figure 4.3: Definition of the layup angle (Kuznecovs et al., 2019)

The two distinct sheathings have been associated as one single sheathing because of the consideration of the friction coefficients, the initial shrink, and their location. It results in no changes in the stresses located in the insulation layer.

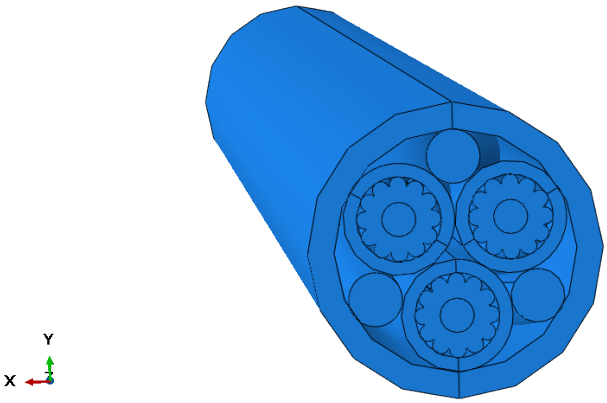

Figure 4.4: ABAQUS (2020) model

As explained in Section 3.2.2, one of the ends has been set as fixed. Hence, all the surfaces have been selected and set up as ENCASTRE condition in ABAQUS (2020) that locks all degrees of freedom. On the other end, the use of multiple points constraints (MPC) is used to apply the translation conditions. The MPC defines a link between one master node or reference point to a set of slave node(s) or element(s). Along with the different options offered by MPC, a beam condition has been chosen between the elements. The beam condition creates a rigid link between the nodes. Hence, a flat surface remains flat over the simulation. In addition, this condition does not constraint the degrees of freedom. So, when a translation is applied along the length of the cable on the master node, the model would allow the rotation around the master node for the other nodes if there was a difference in material properties.

Partitions have been built on each cylinder (insulations, sheathing) to have better control of the mesh aspect and resolution. It is then possible to set the number of layers for each component and the number of nodes around the cylinders. In addition, a circular partition has been introduced on the equivalent wires to apply a fine mesh on the external surfaces which is important for contact properties, and a coarse mesh on the centre to decrease the computation time. Later, Section 4.1.4 presents the mesh convergence analysis carried out.

4.1.3 Calibration

This section explains the calibration process. The purpose of the calibration is to ensure that the FE model used reaches the mechanical properties of the cable selected. If it is not possible to fulfil the requirements, then potential recommendations on how to fix them would be given for future work.

The calibration is divided into two distinct parts, the first one consists of the investigation of the axial stiffness of the cable and the second dwells in the bending stiffness. The calibration of the torsional stiffness is not investigated because the results from SIMA (2020) show small torsional moments. Therefore, this aspect is neglected and it is assumed that the contribution in reducing the fatigue life from torsion is negligible.

4.1.3.1 Calibration of the axial stiffness

To investigate the axial stiffness of the cable, the value of the axial stiffness must be first defined as a goal. HELICA software (2020) provides the axial stiffness of the cable, and the value has been found as 4.7 MN, according to Table 2.1 (Yang, 2018). However, new research and experimentations show that the actual value of the axial stiffness is around 6.5 MN. The differences can be explained by the realisation process. In the industry, the cable is initially shrunk, and all components are in contact with an initial contact pressure. Due to this difference, the value of 6.5 MN is taking as a goal for the calibration because it might be more realistic of the behaviour in real-life conditions.

Due to the highest importance of the calibration over the friction coefficients, the friction coefficients have been assumed to be as in Table 2.3 in this section. Once the FE model is created in ABAQUS (2020) using the different material properties and friction coefficients defined in Section 2.3.1, a unit axial load is applied on one end of the cable. After simulation, it is possible to get the deformation of the cable. According to beam theory, the deformation along the axial direction is enough to determine the axial stiffness of the cable. This axial stiffness is calculated using Equation (9).

$$EA = \frac{F_{axial}}{u} L \tag{9}$$

where EA is the axial stiffness in Newton, F_{axial} is the axial force applied on the model, u is the total deformation in meter and L is the initial length of the beam in meter.

In addition, the cable is twisted in the axial direction because of the layup angle defined in the previous sections. Hence, the influence of the force applied is led by thorough research. For a small force, the different components are not in contact in the FE model. In reality, they are already in contact due to the initial shrunk. So, a higher force has been used to make all components in contact which led to an axial stiffness of 6.65 MN. Since this value diverges by 2.3% from the initial goal, it has been assumed to be good enough.

Otherwise, it can be possible to lower the axial stiffness by reducing the Young's modulus of all the different material components, except the Young's modulus of the insulation layer that should be kept constant because it is the focus of the thesis.

4.1.3.2 Calibration of the bending stiffness

As for the calibration of the axial stiffness, the purpose is the same: verifying the bending stiffness of the FE model compared to the theory. From HELICA (2020), the bending stiffness has been found as 5 Nm², according to Table 2.1 (Yang, 2018). However, no further experimentations have been performed to verify the theory. Then, 5Nm² is the bending stiffness aimed in this thesis.

Same as the calibration of the axial stiffness, the previous FE model in ABAQUS (2020) is used. Then, a bending force in one of the radial directions of the cable is applied. Based on the deflection of the cable and according to beam theory, it is possible to determine the bending stiffness using Equation (10).

$$EI = \frac{L^3 P}{3\,\Delta_{max}} \tag{10}$$

where EI is the bending stiffness in Nm², P is the bending force applied, L is the initial length of the cable and Δ_{max} is the maximum deflection of the cable.

Due to the layup angle, the bending stiffness properties could vary depending on the radial direction of the load. A check has been carried out to make sure it would not influence the results.

The calibration shows a displacement corresponding to bending stiffness of 230 Nm² that is high compared to the value aimed. The assumption of using a solid shape to simulate the strands and wires explains this result. First, there is an addition of material since a solid shape implies the presence of material between the strands and wires. Secondly, using a solid shape does not allow the use of the layup angle for the strands and the wires from the cable geometry definition. Some simulations have been carried out to reduce this bending stiffness. However, no viable solutions have been found for this thesis. Later in the results part, it has been shown that the principal contribution of the fatigue damage accumulation is from the axial stiffness. Hence, as thesis scope, the value of 230 Nm² for the bending stiffness is assumed.

4.1.4 Mesh convergence analysis

The purpose of the mesh convergence analysis is to ensure that the mesh does not affect results. Then, the method is to create meshes with different element sizes and compare them. Hence, it has been decided to use a bending force since it is the most critical case to check the mesh. This work focuses on the stresses in the insulation layer so, the mesh of the other components has been set as coarse as possible and only the insulation's mesh has been studied in this section. Due to computational time, the model's length has been reduced to 100 mm instead of 700 mm to have faster computations.

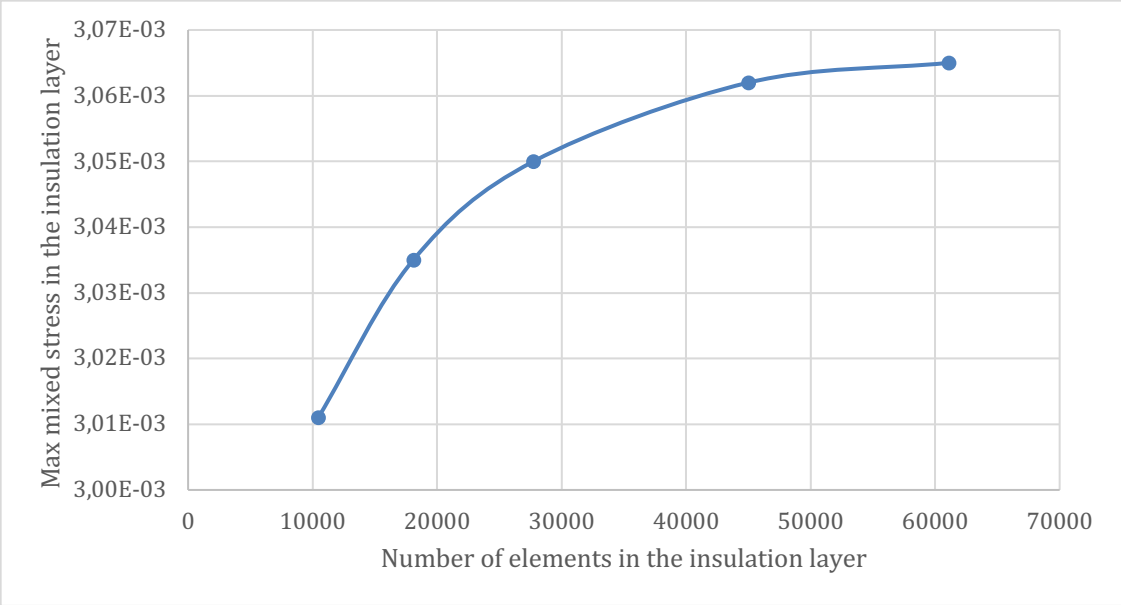

Figure 4.5: Max mixed stresses depending on the number of elements in the insulation layer

Figure 4.5 shows the maximum mixed stresses in the insulation layer depending on the mesh. The mixed stresses are an output from ABAQUS (2020) combining the stresses in all directions. The maximum mixed stresses have been taken according to the sub-modelling method so, in the cross-section at the middle of the segment's length. The results reveal a convergence after 60000 elements. However, the difference between simulations 4 and 5 is small. The maximum mixed stresses change by 0.098% which is reasonable. Hence, the mesh of simulation 4 shown in Figure 4.6 is good enough for accurate results without having a long computation time.

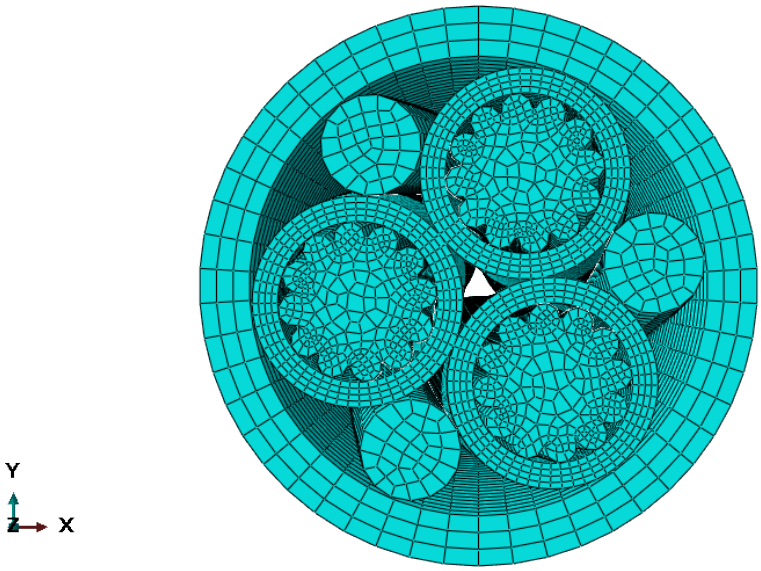

Figure 4.6: Mesh of the cross-section for the mesh selection after the convergence analysis from ABAQUS (2020)

4.2 Analysis of Maxwell stresses

This section details the explanations regarding the procedures taken during the simulations and analyses.

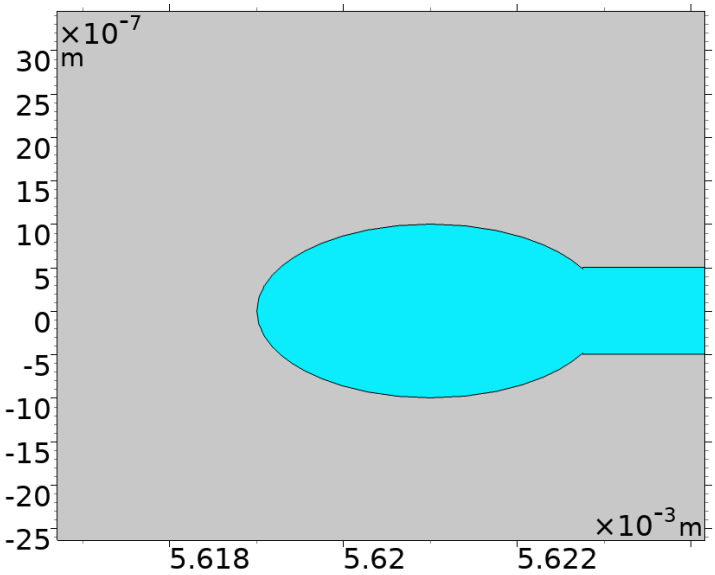

Figure 4.7: Water tree model from COMSOL Multiphysics software (2020)

Figure 4.7 shows the model of the water tree impurity used for carrying out the simulations. The shape of the water tree is similar to the pearl and string shape that has

been described in Section 2.4.3. It has an aspect ratio of 2 for the pearl structure based on the selected dimensions. Only one of the elliptical heads is developed in the model, as shown in Section 2.4.3 It is because the water tree tends to terminate with one elliptical head, and it is the electric field concentration located at the elliptical tip that is of utmost concern. The length of the rectangular region connecting the two elliptical heads is the region that is extended to stimulate the growth of the water tree. The natural growth of water trees cannot be simulated but may be assessed by experimentation. Hence, it is necessary to turn to this form of model development to simulate the conditions of water tree growth. The analyses are carried out in COMSOL Multiphysics software (2020).

4.2.1 Mesh convergence analysis

The objective of the mesh convergence analysis is to ensure that the mesh does not affect the results. To establish this analysis, the method is to carry out the simulation with different mesh sizes and then compare the results in each case.

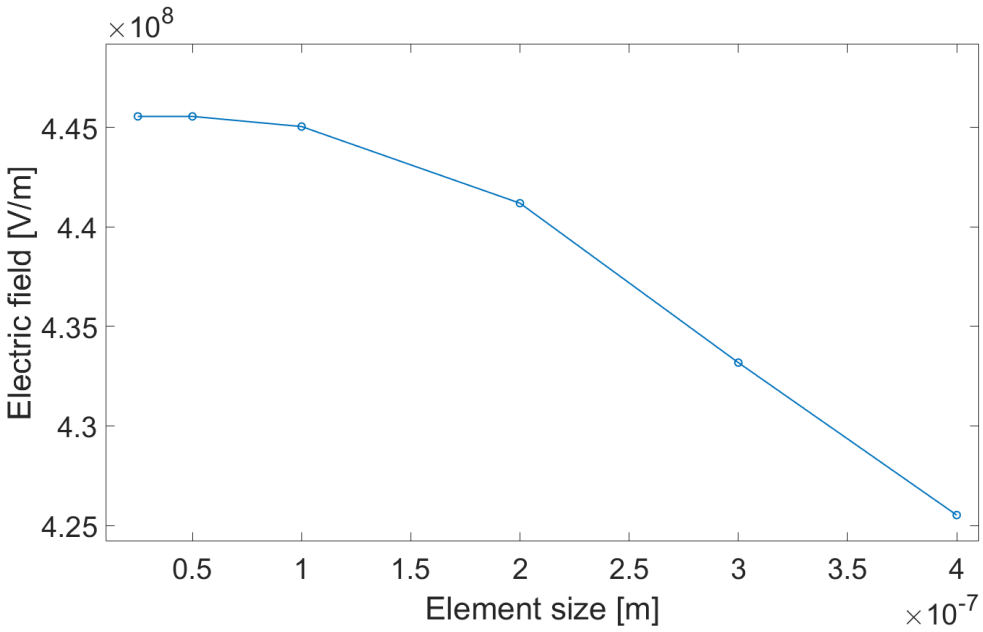

Figure 4.8: Mesh convergence analysis

The mesh element sizes in the simulation vary from $4 \cdot 10^{-7}$m to $0.5 \cdot 10^{-7}$m. From Figure 4.8, there is convergence when the element size is between $0.5 \cdot 10^{-7}$m and $0.25 \cdot 10^{-7}$m. The difference between the results is small for the two simulations. Hence, to decrease computation time, a slightly higher mesh size is selected since there is no numerical difference in the results. The analysis speed does not vary drastically and is completed within 5 minutes. The longest simulation happens when the water tree has been simulated to 90% length from the boundary of the XLPE layer. Further increase in the water tree length is detrimental to the simulation rather than advantageous due to the increased simulation time and the failure condition.

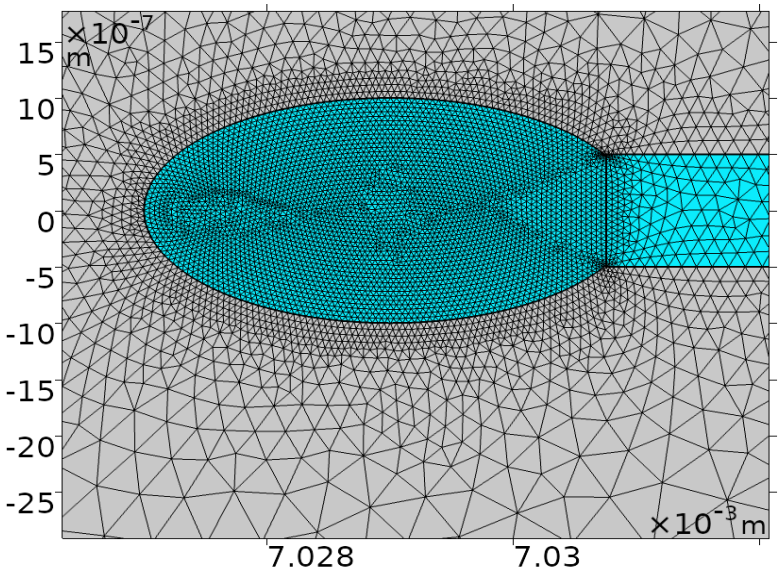

Figure 4.9: Meshing on the water tree region from COMSOL Multiphysics software (2020)

The final mesh size around the elliptical shape of the water tree impurity is $0.5 \cdot 10^{-7}$ m. A larger mesh size in the regions other than that of the water tip does not influence the overall results. It is because the main electric field gradient is located at the tip of the elliptical shape. Though it is observed that the simulation time does not vary drastically with the change in mesh size this observation is limited to the tip of the water tree, however, implementing such a small mesh in the entirety of the model will affect the simulation's time. It is due to this reason that the mesh size in the remaining no influential region is relatively coarse compared to the water tree tip.

4.2.2 Sensitivity analysis

Similar to the mesh convergence analysis, various properties associated with the materials that may influence the results of the simulation must be investigated.

4.2.2.1 Conductivity

The first property to be investigated is the conductivity of the water present in the water tree impurity. The analysis consists of comparing simulation results with different conductivity values.

The conductivity of a material plays a crucial role in the flow of current, hence, in the development of the electric field and Maxwell stress. Figure 4.10 shows the graph obtained after carrying out the conductivity analysis simulations. The values range in the graph represents the conductivity ranges from $1 \cdot 10^{-8}$ S/m to sea water at $1 \cdot 10^{-4}$ S/m. The source of water that is relevant for this case is the seawater since the cables are dynamic subsea cables hence, the value that is used in the simulation is $1 \cdot 10^{-4}$ S/m.

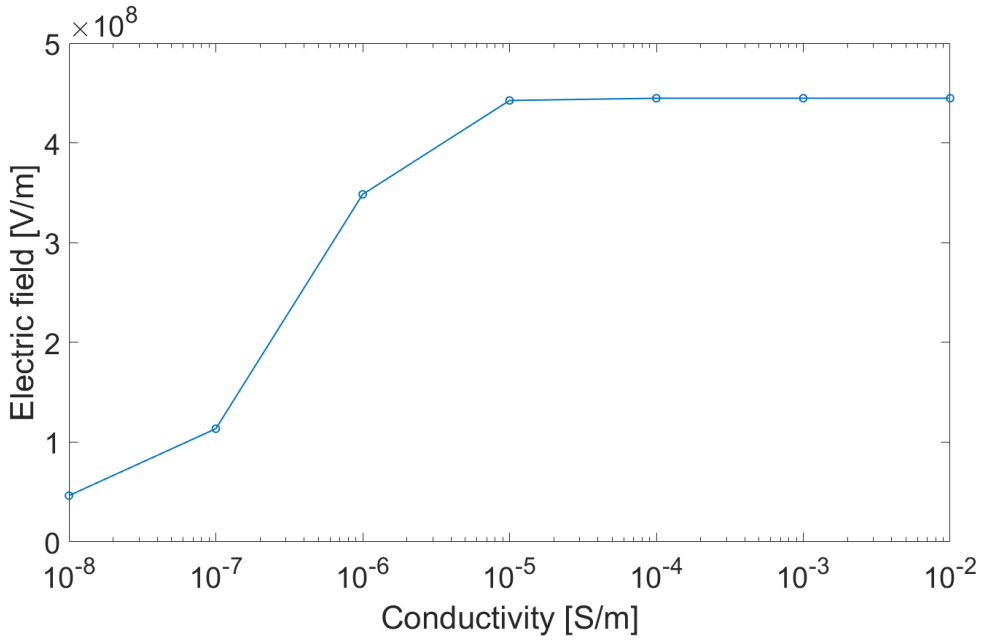

Figure 4.10: Sensitivity analysis: conductivity

It should be noted that any slight change in the conductivity value in either direction provides us with results having negligible numerical value change. Any major deviation from the selected value implies a change in the source of water used for experimentation thus, this parameter can be adjusted based on the region in which the cable operates.

4.2.2.2 Permittivity of water tree

Permittivity ε determines the ability of a material to be polarised. The higher the permittivity, the more the material polarises compared to a material with a lower permittivity. Hence, the material stores more energy in the presence of an applied electric field. The permittivity in vacuum (ε_0) is defined in Equation (11).

$$\varepsilon_0 = \frac{1}{c_0^2 \mu_0} \tag{11}$$

where c_0 is the speed of light in vacuum in m/s and μ_0 is the vacuum permeability in H/m. Similar to the sensitivity analysis of the conductivity, the sensitivity analysis of the permittivity is carried out by comparing simulation results using different permittivity. The range of relative permittivity is based on material data from Granta EduPack software (2020) with values representing the different materials that are involved in the simulation.

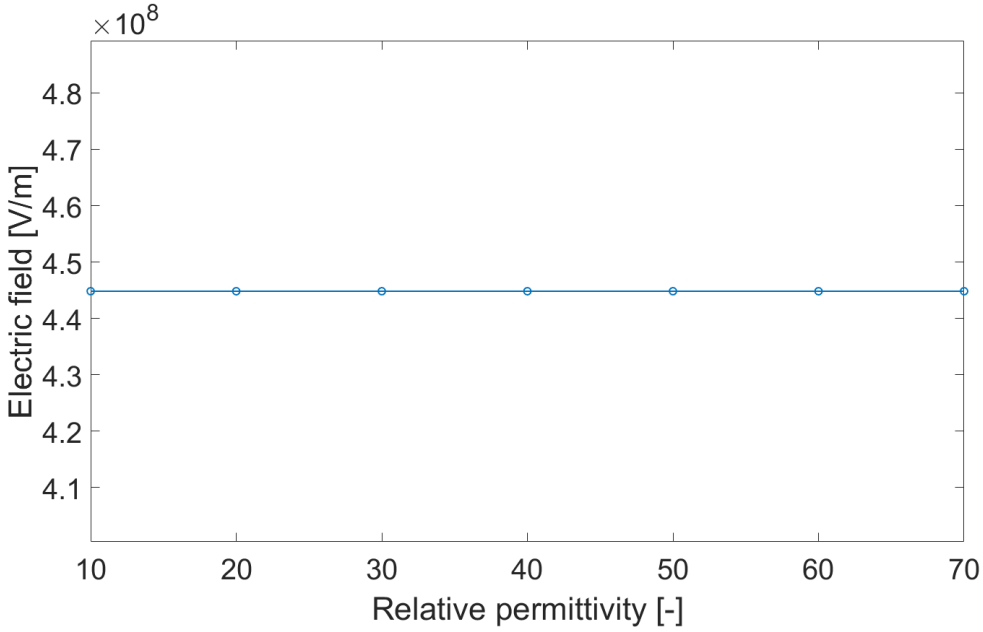

Figure 4.11: Sensitivity analysis: electric field depending on the relative permittivity

The altering of permittivity value of water tree impurity does not change the electric field associated. This may be explained due to the fact the polarising of the water molecule does not interfere with the generated electric field. Since the relative permittivity does not alter the electric field, it can be assumed that this parameter does not influence the electric field and hence, is of lower significance. With this result in reference, the final value of relative permittivity taken is the one from seawater in the region of cable operation. The simulation although it holds less relevance due to its result. It is to be understood that all of the parameters that are involved need to be evaluated to ensure no errors in this respect.

4.2.3 Final parameters of the models

Once all the pre-simulation assessments are carried out, the final parameters selected for the simulation can be identified, the value of conductivity and relative permittivity for the different materials involved. The final mesh dimension and the overall distribution of the mesh are done according to the mesh convergence analysis. Hence, the model has a fine mesh at the tip of the water tree and then, a mesh that gradually becomes coarser in the remaining regions of the model.

Table 4.2: Final water tree parameters for COMSOL Multiphysics software (2020) simulations

Parameter	Value
Mesh element size	$0.5 \cdot 10^{-7}$ [m]
Conductivity	$1 \cdot 10^{-4}$ [S/m]
Relative Permittivity	10 [-]

4.3 Fracture model

According to Section 2.4.1, there are several models capable of simulating various types of cracks. For this work, it has been concluded that the Paris' law method is the one to be used to determine the crack growth and to eventually combine it with the Maxwell

crack growth. Table 4.3 shows the parameters in the Paris' law method in addition to the minimum stress intensity factor to propagate the crack defined as K_{th}. All these parameters are specific to the XLPE material and cannot be used for another material.

Table 4.3: XLPE material properties

Parameter	Symbol	Value	Unit
Crack growth rate	C	$3.8874 \cdot 10^{-7}$	[mm/cycle]
Fatigue crack exponent	m	7.5295	[-]
Minimum stress intensity factor	K_{th}	0.5	[MPa$\cdot$ m$^{0.5}$]

This work focuses on four models that could reflect the water tree crack according to vented water trees. The bow-tie water tree has not been investigated here since the literature shows that this type of water tree does not cause cable failure. In addition, only one water tree is assumed to be present in the same cross-section. The assumption of having multiple water trees in the same cross-section could lead to very complex equations which is not the slope of the work.

First, all four models are presented with their advantages and drawbacks. Then, one of the models is selected based on their comparison and the critical stresses needed to propagate the crack.

4.3.1 Case #1

The first case is to consider a crack located at the edge of the geometry which is assumed to be semi-infinite shown in Figure 4.12, according to Sweeney (1988).

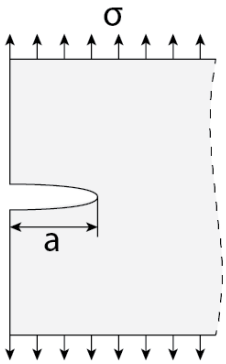

Figure 4.12: Crack geometry of case #1, edge crack in a semi-infinite body (data source: Sweeney, 1988)

This case considers that only the axial stress propagates the crack and there is no influence of the bending stress. The stress intensity factor is defined in Equation (12).

$$K_{case\#1} = f \times \sigma_{\text{axial}} \times \sqrt{\pi . \text{a}} \tag{12}$$

where f is the geometry factor, σ_{axial} is the axial stress in MPa and a is the crack length in meter. Due to the cable's dimensions compared to the water tree crack size, geometry is assumed to be semi-infinite. However, the model does not consider the cylindric shape of the cable and assumes that the water tree is a crack in one direction

even if studies showed that the water tree crack propagates over the thickness of the insulation and also over the radius. In addition, bending stresses cannot be considered.

4.3.2 Case #2

The second case considered is a thumbnail crack in a solid cylinder shown in Figure 4.13, according to Gallaghar et al. (1984).

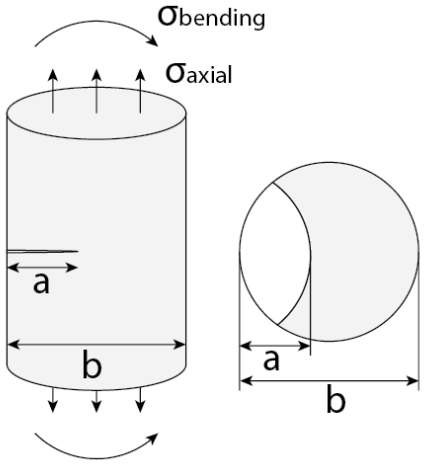

Figure 4.13: Crack geometry of case #2, thumbnail crack in a solid cylinder (data source: Gallaghar et al., 1984)

This case considers both axial and bending stresses. Also, the crack geometry is assumed to be a cylinder. The stress intensity factor is defined in Equation (13).

$$K_{case\#2} = \left(Y_a \sigma_{axial} + Y_b \sigma_{bending}\right) \times \sqrt{\pi . a} \tag{13}$$

where Y_a is an axial coefficient due to the geometry, σ_{axial} is the axial stress in MPa, Y_b is a bending coefficient due to the geometry, $\sigma_{bending}$ is the bending stress in MPa and a is the crack size in meter.

The geometry considered in this model is close to the water tree geometry. First, the crack is assumed to occur in a solid cylinder that can be related to the XLPE insulation, even if the insulation is a hollow cylinder. Moreover, the geometry of the crack could represent the water tree crack propagation since the crack is considered to be in two directions.

4.3.3 Case #3

The third case is quite similar to case #1 and considers an edge crack in a solid plane which has a thickness shown in Figure 4.14, according to Dowling (2007).

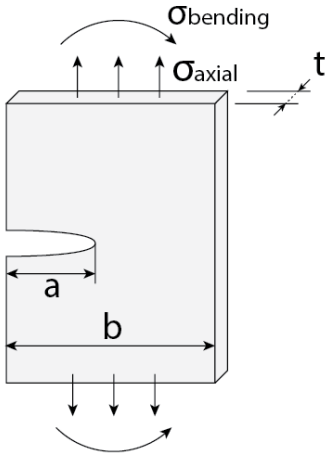

Figure 4.14: Crack geometry case #3, edge through a crack in a plate (data source: Dowling, 2007)

Due to the thickness, the bending stress can be considered compared to the first case. The stress intensity factor is defined in Equation (14).

$$K_{case\#3} = \left(Y'_a \sigma_{axial} + Y'_b \sigma_{bending}\right) \times \sqrt{\pi . a} \tag{14}$$

where Y'_a is an axial coefficient due to the geometry, σ_{axial} is the axial stress in MPa, Y'_b is a bending coefficient due to the geometry, $\sigma_{bending}$ is the bending stress in MPa and a is the crack size in meter.

The main advantage of this case is that it might be more accurate than case #1 since the bending stress can be considered. However, the drawbacks about the geometry of the solid element and the crack are the same.

4.3.4 Case #4

The last case is the most complex and considers an elliptical surface crack in a plate shown in Figure 4.15, according to Anderson (2005).

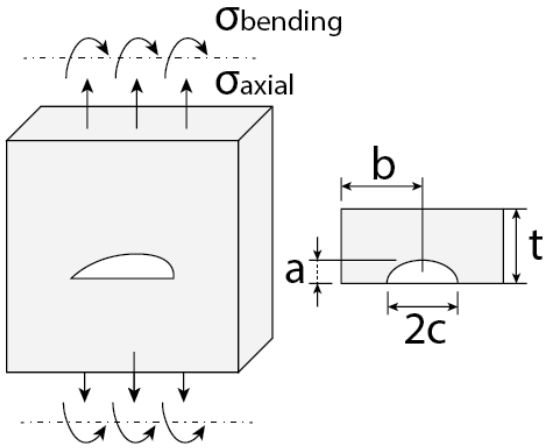

Figure 4.15: Crack geometry case #4, elliptical surface crack in a plate (data source: Anderson, 2005)

The model considers both axial and bending stresses and introduces the width of the elliptical surface crack. The stress intensity factor is defined in Equation (15).

$$K_{case\#4} = \left(Y''_a \sigma_{axial} + Y''_b \sigma_{bending}\right) \times \sqrt{\pi . a} \quad (15)$$

where $Y"_a$ is an axial coefficient due to the geometry, σ_{axial} is the axial stress in MPa, $Y"_b$ is a bending coefficient due to the geometry, $\sigma_{bending}$ is the bending stress in MPa and a is the crack size in meter.

The crack geometry of this model is quite accurate of the water tree propagation since it is an elliptical surface crack that can be assimilated to case #2. Besides the geometry, the model includes a parameter about the width of the crack which is not implemented in case #2.

4.3.5 Comparison of the cases

This section provides a comparison of the cases presented above. According to the drawbacks and advantages of each of the models, it seems that case #2 might be the most accurate model. However, the need of considering the minimum axial and bending stresses to propagate the crack is primordial to determine which case could be critical. Hence, an in-house MATLAB (2020) code has been written to estimate the minimum stress required to propagate the crack for each case. This code uses the function *solve* from MATLAB (2020) combined with the equations presented above. This code allows determining the minimum stresses individually. As a reminder, the final crack size corresponds to 60% of the thickness insulation hence, 1.056 mm in length. For an initial crack size of 0.01 mm, Table 4.4 shows the critical values.

Table 4.4: Minimum stresses required to propagate the crack for an initial crack size of 0.01 mm

	Case #1	Case #2	Case #3	Case #4
Minimum axial stress	79.65 MPa	135.72 MPa	79.47 MPa	83.95 MPa
Minimum bending stress	N/A	135.89 MPa	39.79 MPa	84.53 MPa

Due to the high stresses needed to propagate the crack, a larger initial crack size is assumed. This might not be the case in real life however, due to the Maxwell stresses, the crack length might achieve a higher crack size. Hence, for an initial crack size of 0.5 mm, Table 4.5 shows the critical values.

Table 4.5: Minimum stresses required to propagate the crack for an initial crack size of 0.5 mm

	Case #1	Case #2	Case #3	Case #4
Minimum axial stress	11.26 MPa	18.82 MPa	10.95 MPa	26.55 MPa
Minimum bending stress	N/A	20.05 MPa	5.83 MPa	73.29 MPa

The most critical minimum axial and bending stresses correspond to the stresses where the initial crack size is also the final crack size. This gives the condition if the stresses found later in ABAQUS (2020) can have an impact on the cable before failure. Table 4.6 presents these values.

Table 4.6:Minimum stresses required to propagate the crack for an initial crack length equals the final crack length

	Case #1	Case #2	Case #3	Case #4
Minimum axial stress	7.75 MPa	12.43 MPa	7.21 MPa	26.70 MPa
Minimum bending stress	N/A	14.22 MPa	4.02 MPa	-169.73 MPa

The value of the minimum bending stress for case #4 is negative so is approximated to 0 MPa instead. As shown in the tables above, the values are still large but reasonable and might be reachable due to the mechanical loads. Looking at the values, it seems not safe to consider case #4 since first, the drawbacks/advantages are not preferable to the other cases and second, the minimum stresses are the largest. Then, case #3 seems more accurate than case #1 because it includes the thickness of the material and allows to use of bending stresses. So, case #1 is also excluded. Then, the choice is between case #2 which looks more accurate due to the assumptions of the model, and case #3 which is the most critical. Due to the large disparities between the two cases, it has been chosen to use case #3 to be more conservative. Since this model is used later on in the thesis, all the equations to determine the coefficients of model #3 are specified in Equation (16) according to Dowling (2007).

$$\begin{cases} \alpha_{geo} = \dfrac{a}{b} \\ Y'_a = 0.265\left(1-\alpha_{geo}\right)^4 + \dfrac{0.857 + 0.265\,\alpha_{geo}}{\left(1-\alpha_{geo}\right)^{\frac{3}{2}}} \\ Y'_b = \sqrt{\dfrac{2}{\pi\alpha_{geo}}.\tan\left(\dfrac{\pi\alpha_{geo}}{2}\right)} \times \dfrac{0.923 + 0.199\,\left(1-\sin\left(\dfrac{\pi\alpha_{geo}}{2}\right)\right)^4}{\cos\left(\dfrac{\pi\alpha_{geo}}{2}\right)} \end{cases} \quad (16)$$

To conclude, this section investigates different fracture mechanics models and compares them based on the crack geometry, the case geometry, and finally, the minimum stresses required to propagate the crack. It has been concluded that model 3 which is the edge crack in a solid plane has a crack geometry and case that could correspond to the geometries of this work. In addition, it has been seen that model 3 is the most critical when it comes to the minimum stresses required to propagate the cracks. Hence, this model is the most conservative to use. The minimum stress required to propagate the crack is 7.21 MPa for the axial stress and 4.02 MPa for the bending stress if taken separately. These values are used to have an idea if a case might or might not propagate the crack. Later, the results in ABAQUS (2020) determine the minimum crack size required to propagate the crack combining both axial and bending stresses for the different cases.

4.3.6 Electrical crack growth

The water tree crack growth due to Maxwell stress is based on the kinetic theory of fracture at the tip of the water tree. Young (2019) explains the phenomenon as the breaking of interatomic bonds that lead to polymer fracture. The gradual breaking of these bonds leads to monomer breaks within the XLPE polymer chain, and the continuation of this process leads to the propagation of water trees (Young, 2019).

Stress accumulation over multiple cycles is required to break a polymer monomer chain (Tao et al., 2016). If it can be assumed that one stress cycle accumulated relates to a single unit of energy accumulation, then throughout cycles the accumulated energy will exceed the yield strength of the XLPE and would lead to the breaking of the monomer chain. Tao et al. (2016) provide an equation for this energy accumulation shown in Equation (17).

$$0.5\mathrm{V}_0\varepsilon_0\nabla(\varepsilon_r - 1)E^2 > \sigma_{yield}V_0 \tag{17}$$

where V_0 is the volume of XLPE on which the energy delivered by the Maxwell stress is accumulating, σ_{yield} is the yield strength of XLPE, V_0 is the voltage in V, and E is the electric field in V/m. ε_0 is the electrical permittivity in vacuum and ε_r is the relative electrical permittivity of a material with respect to vacuum. $\nabla(\varepsilon_r - 1)$ is the partial differentiation of relative permittivity $(\varepsilon_r - 1)$.

Once the energy accumulated per cycle is determined, the number of monomer chains that break in a set time can be determined. Hence, the crack growth can be deduced since the length of the monomer chains is known because the diameter of monomer chains is a fixed factor for XLPE material. Also, it has been assumed that the chains are oriented straight. The Maxwell stress helps to calculate the number of monomers broken in 10 minutes using the work from Young (2019). Then, it is possible to determine the water tree growth in 10 minutes and further in 1 minute. The estimated fatigue life of the cable due to Maxwell stress can be determined using the previous calculations.

5 Results and discussions

In this section, all the results from the mechanical parts and then from the electrical part are presented. Then, a discussion to better understand the results is given.

5.1 Mechanical results

As explained in Section 3.2, the mechanical results are divided into different parts. First, the fatigue damage accumulation of the cable is presented to determine the location of the most critical stresses. Then, the location provides the displacements for ABAQUS (2020) to determine the stresses in the insulation layer. Finally, this section gives an attempt at the calculation of the cable fatigue life.

5.1.1 Global loads from SIMA

From SIMA (2020), the various simulations have a simulation time of 1200 seconds with a frequency of 10 Hz, hence 12000 data points over the simulation time. Only the data after 60 seconds is considered. The time before 60 seconds corresponds to the transient time and it must be removed. The cable of 126 meters in length is divided into 106 segments. This segmentation has been set according to the mesh implemented in SIMA (2020).

The 23 first and last cable segments correspond to bending stiffeners that cover the cable to reduce the curvature at the boundary conditions. Also, these stiffeners prevent the cable to have direct contact with the WEC or the hub (Yang, 2018). Once the simulation is over, the bending stiffeners are excluded because they are not the focus of the work. Moreover, their variable diameter makes the fatigue damage accumulation inaccurate. In addition to these 23 first and last segments, an extra 2 segments from both sides have been excluded. They are too close to the bending stiffeners and the results might be then affected by the boundary conditions considered as the bending stiffeners.

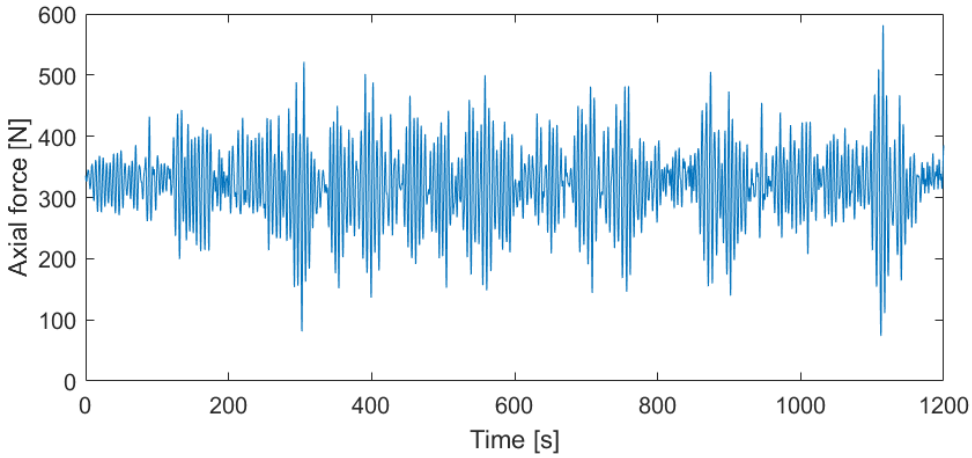

Figure 5.1: Example of the axial force overtime for an element of the cable

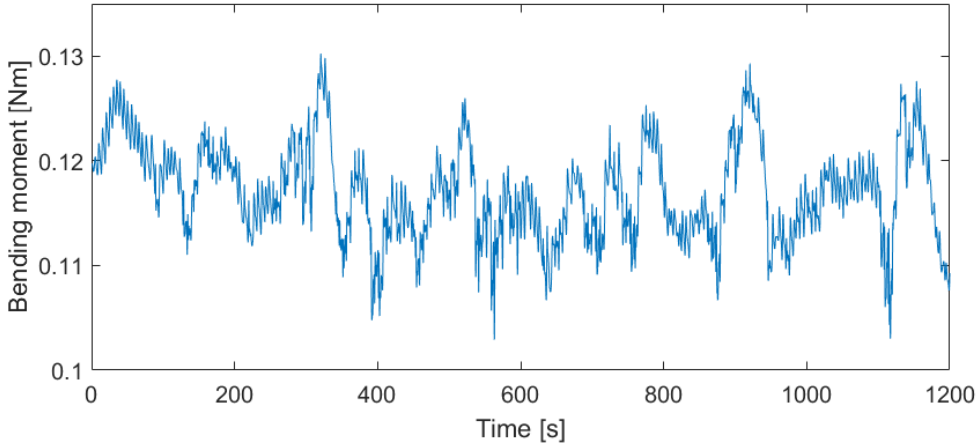

Figure 5.2: Example of the bending moment around Y overtime for an element of the cable

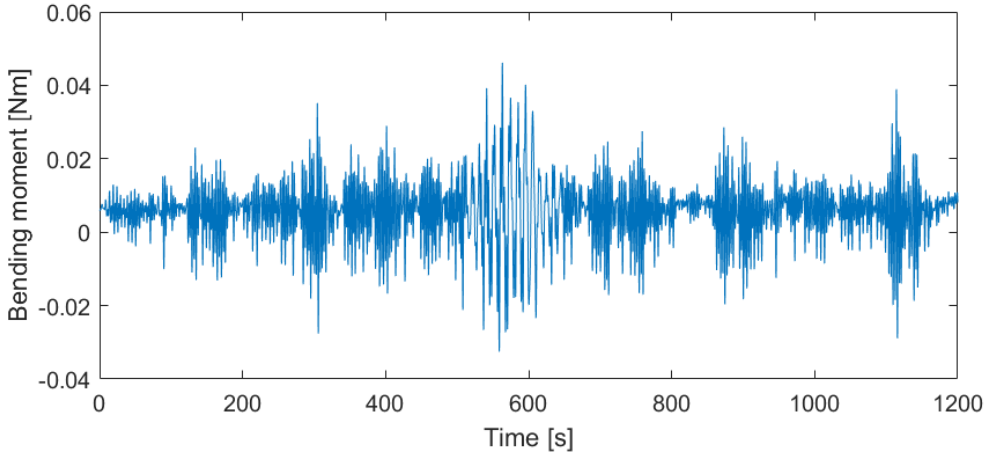

Figure 5.3: Example of the bending moment around Z overtime for an element of the cable

Figure 5.1, Figure 5.2, and Figure 5.3 are examples of the axial force, bending moments around Y and Z after the stimulation from SIMA (2020). As explained before, Figure 5.1 shows a transient time of 60 seconds at the beginning of the simulation, where the axial forces are small compared to the rest of the simulation.

From the data presented above, it is possible to determine the fatigue damage accumulation over the length of the cable using a MATLAB (2020) fatigue code developed by Yang (2018).

5.1.2 Fatigue damage accumulation (FDA) of the cable

From the sea states defined in Section 4.1.1, the various simulations in SIMA (2020) have been executed. From the output data explained in Section 5.1.1, the fatigue life estimation has been assessed for the different sea states. The code provided by Yang (2018) calculates the fatigue damage accumulation taking points all around the cable. Hence, the different angles found in the following figures represent these points.

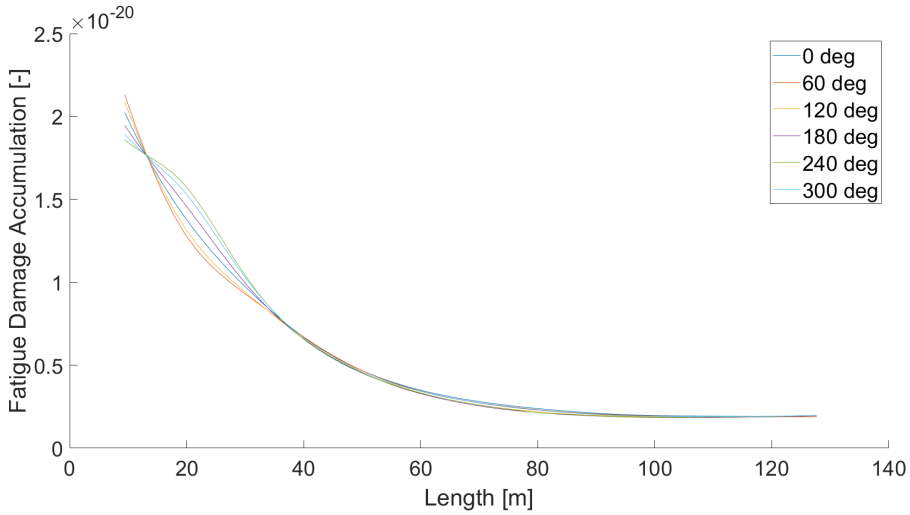

Figure 5.4: FDA for 3 hours along the length of the cable for sea state 1

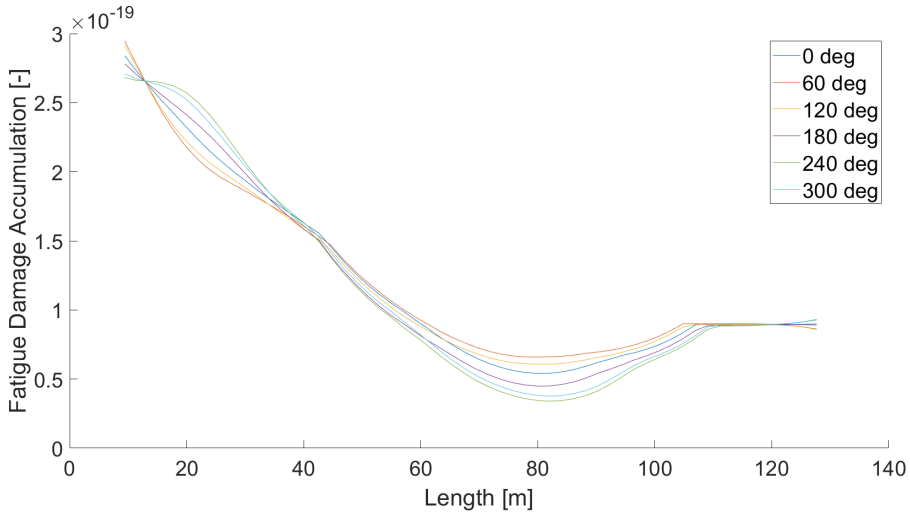

Figure 5.5: FDA for 3 hours along the length of the cable for sea state 2

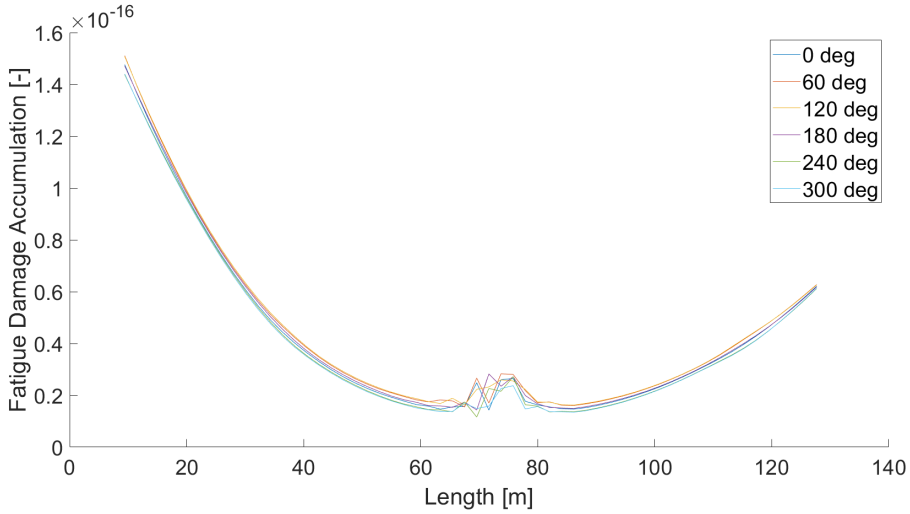

Figure 5.6: FDA for 3 hours along the length of the cable for sea state 5

The previous results presented in Figure 5.4, Figure 5.5, and Figure 5.6 reveal the impact of the sea state on the critical location for the fatigue damage accumulation. Also, there is a direct correlation between fatigue damage accumulation and the sea

state. For a smooth sea state, the FDA is around 10^{-20} where the FDA for a rough sea state is around 10^{-16}. This shows the importance of focusing sea states with important wave height because the potential crack propagation would be larger. Based on the results, the first location is taken as the beginning of the cable without the bending stiffeners since the FDA is the largest. It is located at the beginning of the cable around 15 meters. Then, another location is investigated for sea state 5 due to the peak at the middle of the cable. A relevant observation is to check the absolute value of the extreme stress range along the cable. As shown in Figure 5.7, the highest stress range seems to be correlated to the FDA.

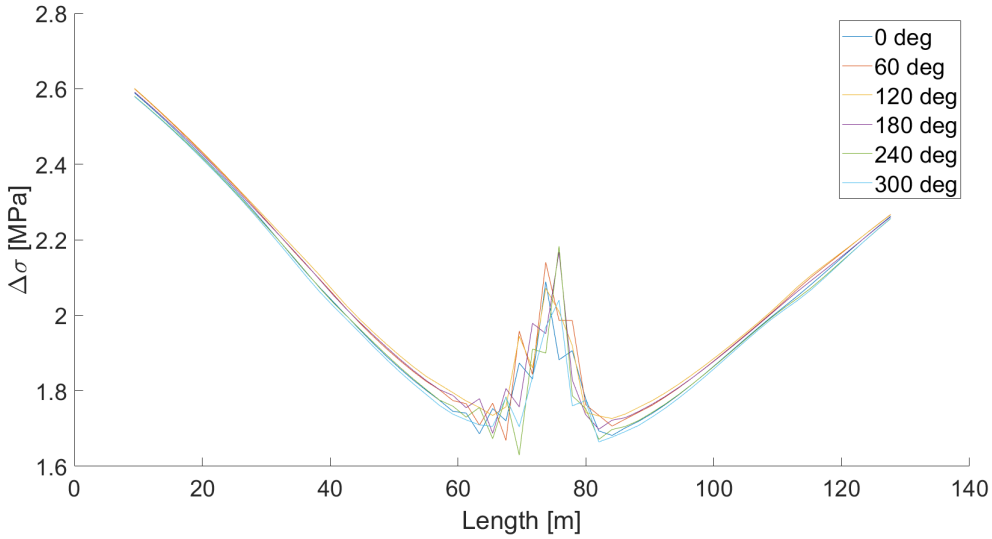

Figure 5.7: Maximum stress range along the length of the cable for sea state 5

Nevertheless, the maximum stress ranges are the FDA is still smaller than the first location. In addition, only sea state 5 has this peak so, the crack propagation over the lifetime of the cable is negligible compared to the first location. Hence, only the first location is considered later in the work.

5.1.3 Histograms of the different locations

This section presents the histograms of the first location selected in the previous section. They allow the selection of the load cases. To plot the histogram with the highest FDA, a MATLAB (2020) script has been written to determine which angle is the most critical.

5.1.3.1 Sea state 1

The histogram for sea state 1 is shown in Figure 5.8. Since the normal stress ranges are small, only the highest is computed, hence 0.54 MPa. Later, if the normal stresses are high enough to propagate the crack, other normal stresses would be considered.

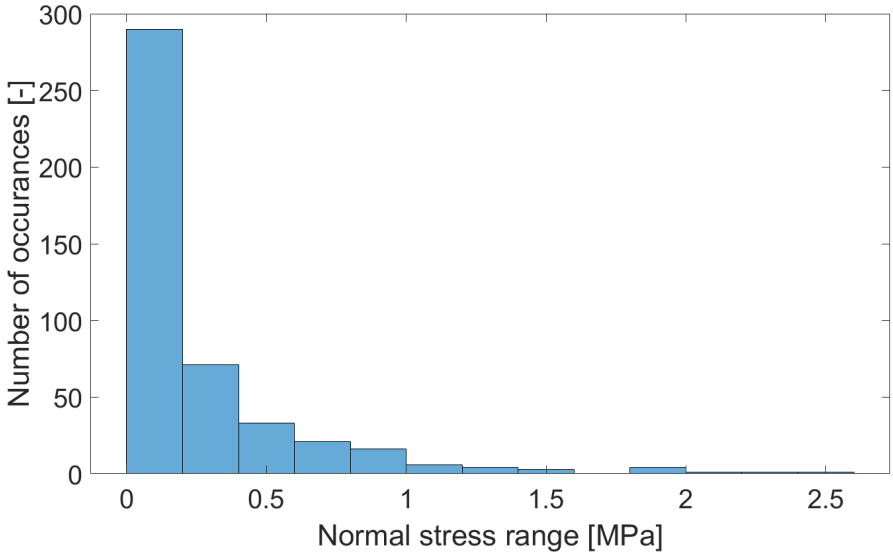

Figure 5.8: Histogram of the first location for the sea state 1 for angle 240°

5.1.3.2 Sea state 2

Same as before, the histogram for sea state 2 is shown in Figure 5.9. The highest stress range is 0.91 MPa.

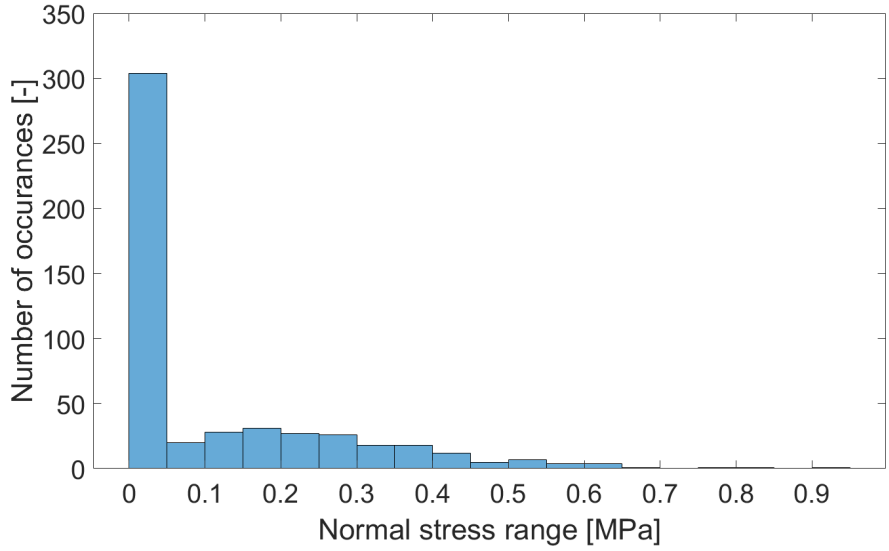

Figure 5.9: Histogram of the first location for the sea state 2 for angle 0°

5.1.3.3 Sea state 5

Same as before, the histogram for sea state 5 is shown in Figure 5.10. The highest stress range is 2.58 MPa.

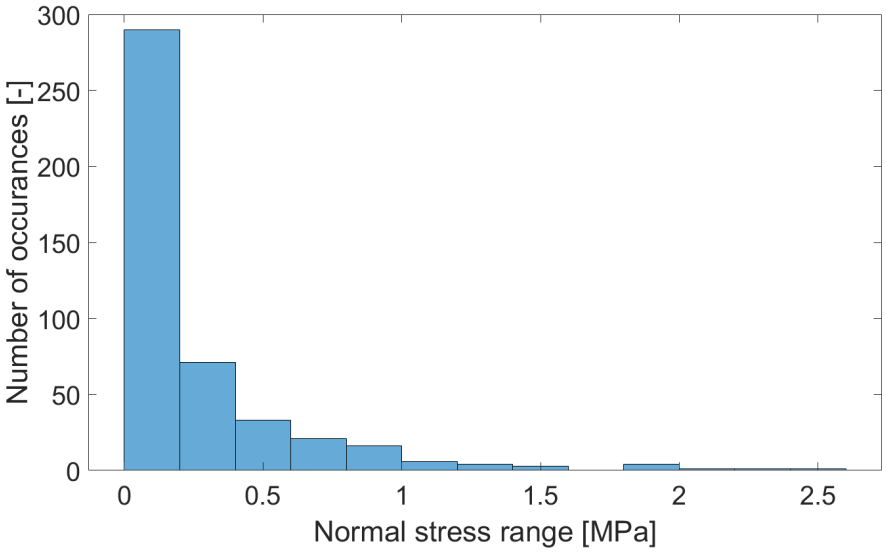

Figure 5.10: Histogram of the first location for the sea state 5 for angle 210°

The unequal distribution of the histogram shows a high number of occurrences for normal stress ranges lower than 1 MPa, and then small occurrences for normal stress ranges larger than 1 MPa. According to fracture mechanics, higher stress ranges would grow a crack faster than smaller stress ranges. Then, the choice has been made to study the highest normal stress range, and depending on the results on the crack propagation, other normal stress ranges might be selected.

5.1.4 Determination of the displacements in ABAQUS

As explained in Section 3.2.1.5, the goal is to determine the displacements to exploit as input in ABAQUS (2020). Since the time steps for the critical stresses are known from SIMA (2020), it is possible to determine the relative displacement by taking the position difference between the two endpoints and by removing the initial length of the cable. In addition, SIMA (2020) has a specific coordinate system that differs from the one in ABAQUS (2020). In ABAQUS (2020), the displacements along X and Y define the bending displacements where the displacements along Z define the axial displacements as shown in Figure 5.11.

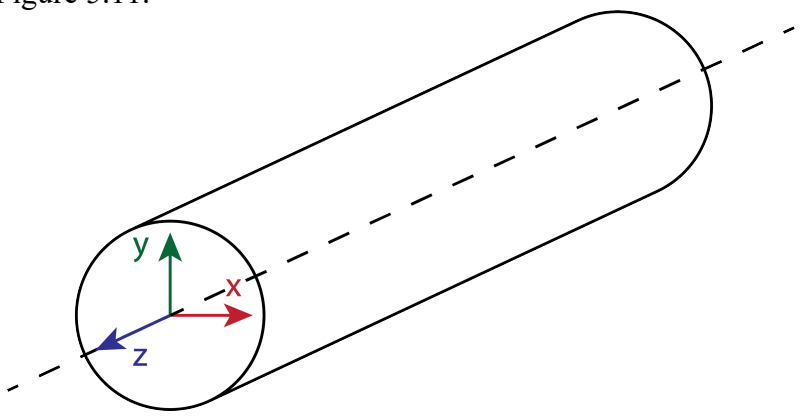

Figure 5.11: Coordinate system in ABAQUS (2020)

Figure 5.12 shows the coordinate system in SIMA (2020) and the different angles used in this section.

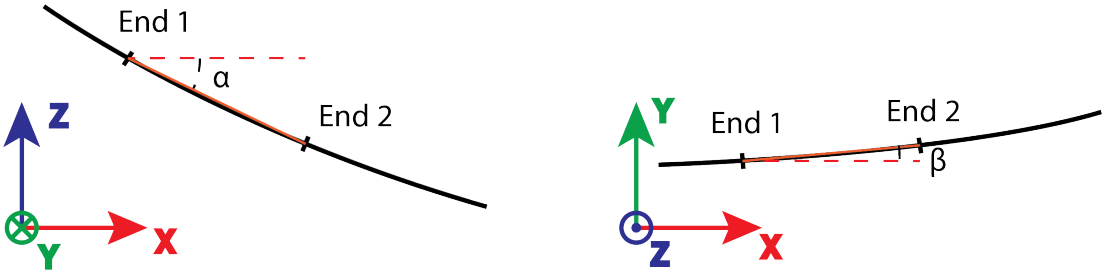

Figure 5.12: Coordinate system in SIMA (2020)

First, the determination of the theoretical coordinates of the second endpoint using the length of the cable is done. It has been assumed that the segment is straight to calculate the rotational angles between the bases. These coordinates are demonstrated using Equation (18).

$$\begin{cases} X_{theo} = l_{segm}\cos(\alpha)\cos(\beta) \\ Y_{theo} = l_{segm}\cos(\alpha)\sin(\beta) \\ Z_{theo} = l_{segm}\sin(\alpha) \end{cases} \tag{18}$$

Then the relative displacements in the coordinate's axes of SIMA (2020) are found using the difference between endpoint 2 and endpoint 1 minus the theoretical length of the cable as shown in Equation (19).

$$\begin{cases} Displ_X = X_2 - X_1 - X_{theo} \\ Displ_Y = Y_2 - Y_1 - Y_{theo} \\ Displ_Z = Z_2 - Z_1 - Z_{theo} \end{cases} \tag{19}$$

where, $Displ_X$, $Displ_Y$ and, $Displ_Z$ are the displacements along X, Y, and Z. The subscripts 2 define endpoint 2 where subscripts 1 define endpoint 1.

Finally, to have the displacements along X, Y, and Z in the ABAQUS (2020) coordinate system, Equation (20) has been used.

$$\begin{cases} Displ'_X = Displ_X\cos(\alpha) + Displ_Z\sin(\alpha) \\ Displ'_Y = Displ_Y \\ Displ'_Z = Displ_Z\cos(\alpha) - Displ_X\sin(\alpha) \end{cases} \tag{20}$$

From the different sea states, the displacements for ABAQUS (2020) have been found and resumed in Table 5.1.

Table 5.1: Displacements input for ABAQUS (2020) depending on the sea state

	$Displ'_X$ [mm]	$Displ'_Y$ [mm]	$Displ'_Z$ [mm]
Sea state 1	-0.83	0.26	2.82
Sea state 2	-0.82	0.17	2.18
Sea state 5	-1.13	3.41	12.18

These displacements are valid for a cable's segment having a length of 700 mm and must be scaled if the segment length is reduced. As shown in this table, the displacements are small compared to the segment's length and represent only 1.74% of

the total length. Hence, the assumption of linear analysis is verified and the axial stresses in the XLPE layer are expected to be small.

5.1.5 Adjustment of the model for the simulation of the sea states

Once the model has been correctly set up, simulations for the sea states have been started with the displacements corresponding to the highest stress ranges. However, it has been seen over this thesis that the displacements are too large for the FE model and induce computation issues such as no convergence of the results. Some solutions have been investigated to solve the computation issues and allow the determination of the normal stresses in the XLPE.

First, the model has been reduced in length to reduce the number of elements. Hence, the displacements have been scaled at the same factor as the length reduction. After some investigation, the reduction in length of the cable shown that it would increase the axial stiffness EA in addition to the bending stiffness EI. This might be caused by the layup angle which becomes almost insignificant when the length of the cable is not long enough. In addition, the layup angle showed a direct impact on the EA and EI values.

Hence, the layup angle has been scaled as well. If on the 700 mm length model, which is the normal length of the cable's segment, the layup angle implied two rotations for the different components over the length, then the shorter model should have the same number of rotations to maintain the layup angle influence. After investigation, the new model reveals that the mechanical properties of the cable have been fixed with a decrease of 28% for the bending stiffness EI. However, when applying the sea states boundary conditions, again the software faced computation issues with no convergence of the results.

Finally, it has been decided for the rest of the work to suppress the layup angle. Even if this assumption might not represent anymore the studied cable, it allows the continuation of the work and the analysis of the results, and the life estimation. In Section 7, some solutions are giving as future work to reduce or fix this issue.

Concerning the length of the segment simulated, it is now possible to simulate with a length of 700 mm since the layup angle has been removed. Still, an investigation is carried out later in the thesis to see if it is possible to reduce the length of it without impacting the results. In addition, a study of the influence of the friction coefficient is also carried out.

5.1.5.1 Investigation of the segment's length for the sea state simulations

In this section, an investigation of the segment's length is carried out to see if it is possible to gain computational time. Since it was possible to simulate sea state 5 for a cable length of 700 mm, this case is taken as a reference since it is the most critical one and so, with the highest displacements. To make this comparison, three models have been set up. One of these models is the reference and has a length of 700 mm. The other models have a length of 350 mm and 100 mm. It has been assumed that the friction coefficients between the different components are the ones defined in Table 2.3.

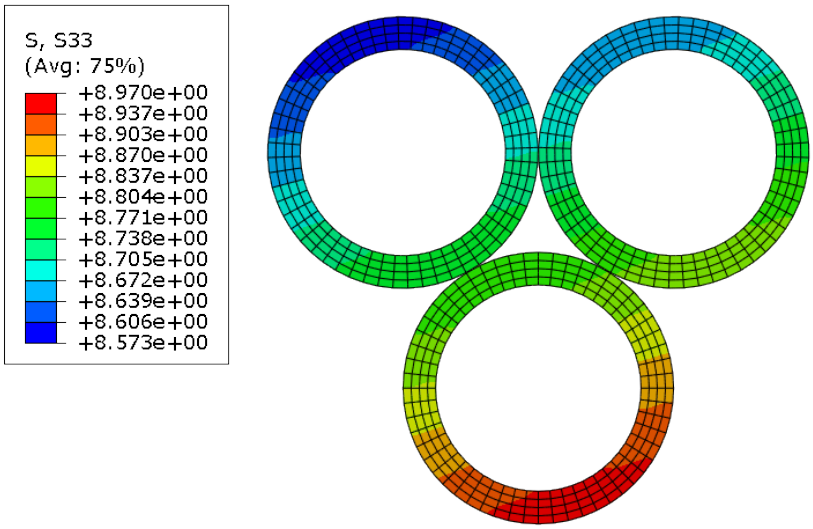

Figure 5.13: Normal stresses in XLPE due to sea state 1 for a cable length of 100 mm

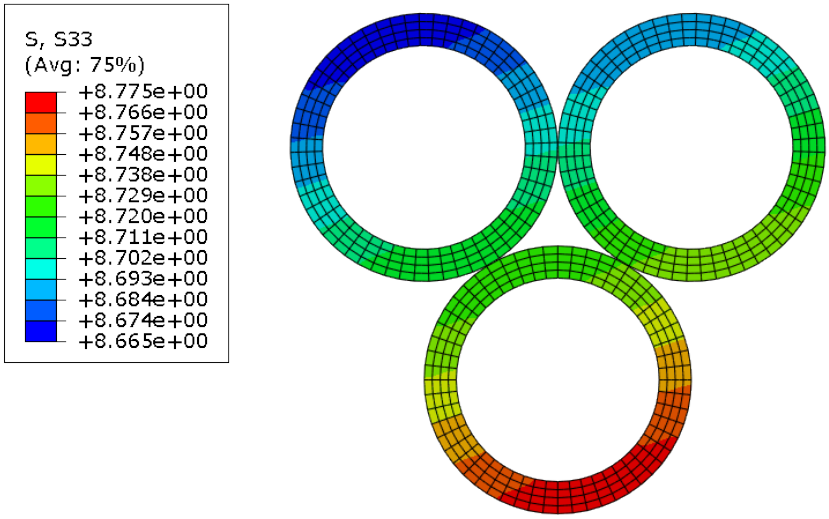

Figure 5.14: Normal stresses in XLPE due to sea state 1 for a cable length of 350 mm

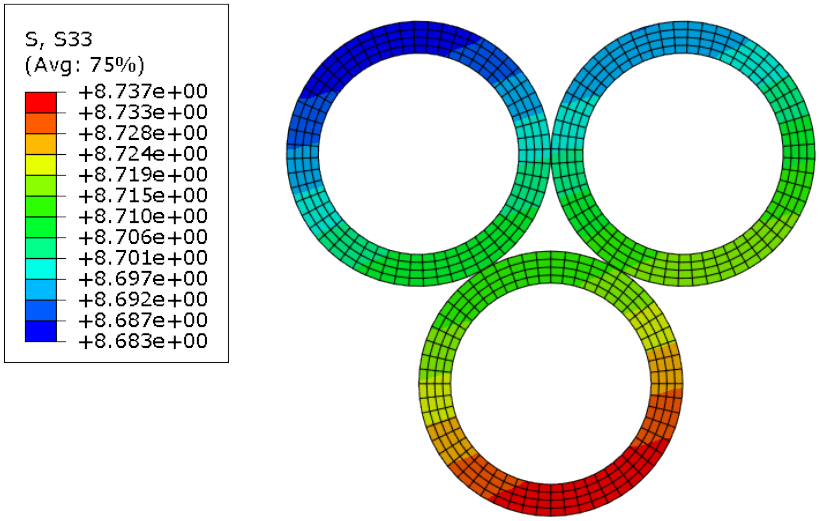

Figure 5.15: Normal stresses in XLPE due to sea state 1 for a cable length of 700 mm

From Figure 5.13, Figure 5.14, and Figure 5.15, the normal stresses in the XLPE for sea state 5 are plotted for different cable lengths. It seems that the shorter is the length, the higher are the stresses. For the comparison, the 700 mm length cable is taken as a reference because it corresponds to the initial length between two nodes in SIMA (2020). Between 700 mm and 350 mm, the difference is up to 0.4%, and between 700 mm and 100 mm, the difference is up to 2.7%. From these results, taking a shorter cable length would not influence too much the results. However, the gain in computation time by shortening the cable length is reduced from 21 minutes for the segment's length of 700 mm, to 12 minutes for the segment's length of 350 mm, until 4 minutes for the segment's length of 100 mm.

It can be noted that in the slope of this thesis, only the highest load cases of each sea state are considered and so, the computation time using the segment's length of 700 mm is still reasonable in addition to more accurate results. Hence, the segment's length is now taken as 700 mm for the thesis. Nevertheless, for future work, if now the focus is not to implement a few load cases, but the full stress history for each sea state, a decrease of 43-81% on the computation time could help the simulations to be faster without impacting too much the results.

5.1.5.2 Investigation of the friction coefficient for the cable

Now, the focus is to investigate the impact of the friction coefficient on the results. Three different models have been set up with different friction coefficients. The first model is defined with the friction coefficients in Table 2.3 with various values between each of the components. Then, the second and third models are a full-stick model and a frictionless model. The choice of a full-stick model is because during the manufacturing, the cable is shrunk, and all the various components are in contact with an initial contact pressure. Hence, it could imply material penetration and so, full-stick contacts. Then, the frictionless model shows if there is an impact of friction on the stresses in the insulation layer. For the simulations, the worst sea state is considered hence, sea state 5.

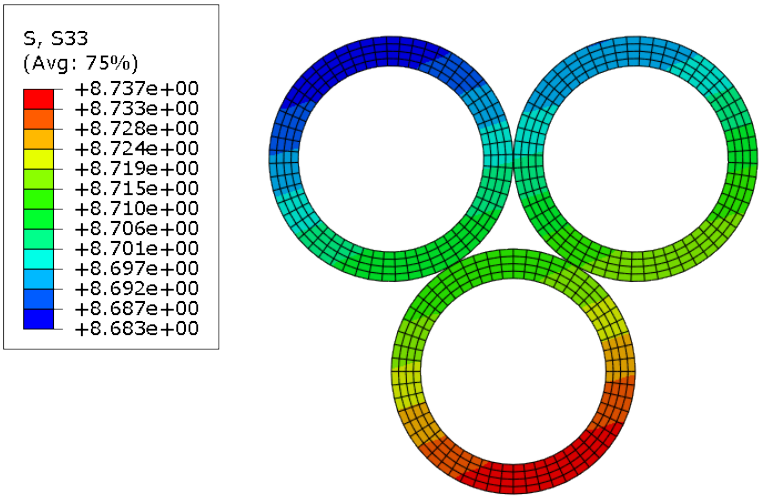

Figure 5.16: Axial stresses in the insulation layer for the friction coefficients defined in Table 2.3

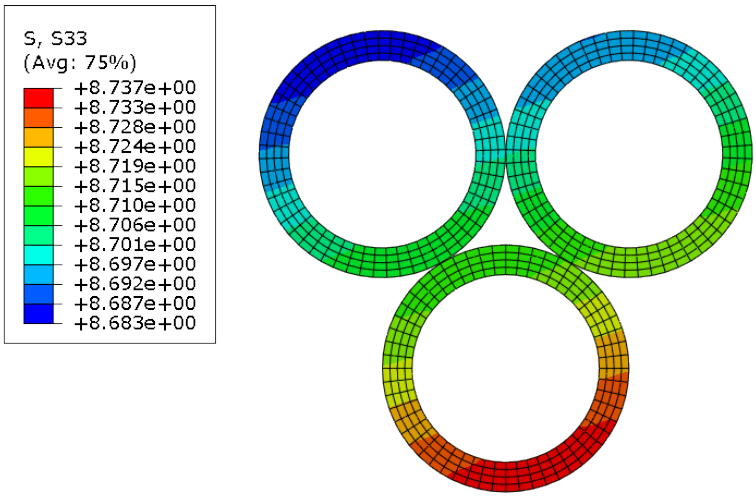

Figure 5.17: Axial stresses in the insulation layer for a full-stick condition

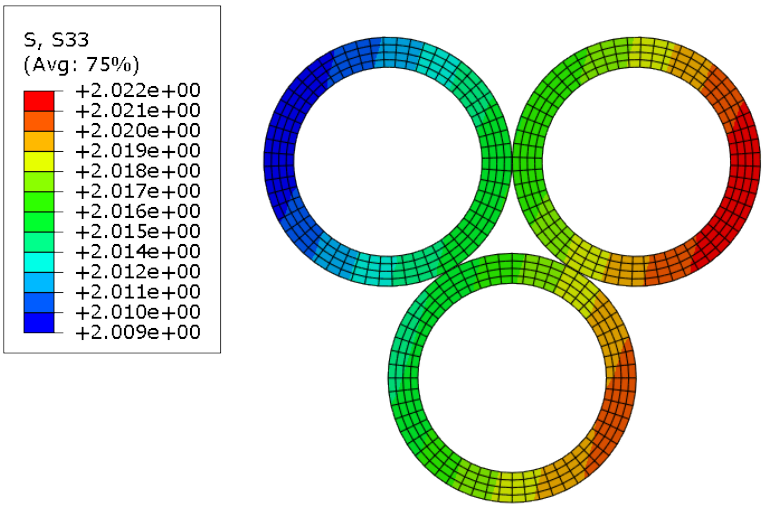

Figure 5.18: Axial stresses in the insulation layer for a frictionless condition

The results in Figure 5.16, Figure 5.17, and Figure 5.18 show that there are no impacts due to the change of the friction coefficients. Hence, a small investigation is carried out to see if there is a contact between the components over the simulations.

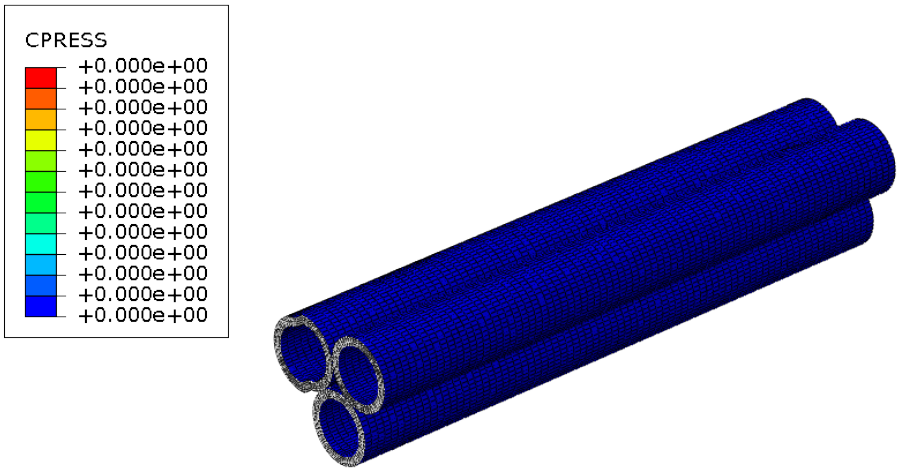

Figure 5.19: Contact pressure of the XLPE layer and the other components

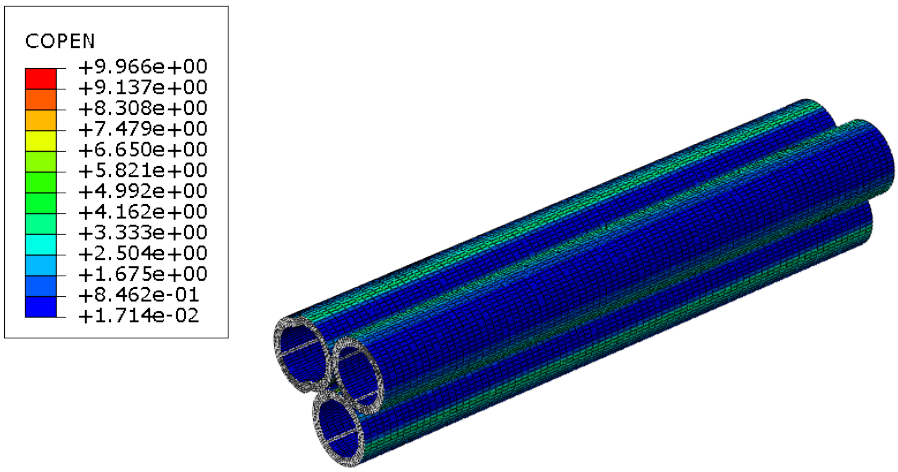

Figure 5.20: Minimum distance between the XLPE layer and the other components

From Figure 5.19, the contact pressures CPRESS over the XLPE layer are zero all over the length of a part selected around the middle of the segment. In addition, from Figure 5.20, the minimum distance between the XLPE layer and the other components is displayed. All these distances are above zero meaning that there are no contacts. Hence, the displacements are not large enough to induce any contact between the different components. Moreover, the initial shrunk of the cable has been neglected.

To conclude, the values of the friction coefficients do not impact the results to a large extent. However, it has been seen that the frictionless model takes 20% less time to compute results. Hence, the frictionless model is selected for the rest of the work. In Section 7, some ideas about how to compute correctly the initial shrunk and so, to compute properly the different contact conditions between the materials.

5.1.6 Determination of the axial and bending stresses in the XLPE

This section discusses the results of the axial stress found in the XLPE. Later in Section 5.1.7, these results are used to attempt the cable fatigue life.

5.1.6.1 Sea state 1

After simulation in ABAQUS (2020), the final axial stresses found in the XLPE are shown in Figure 5.21 using the displacements from Table 5.1.

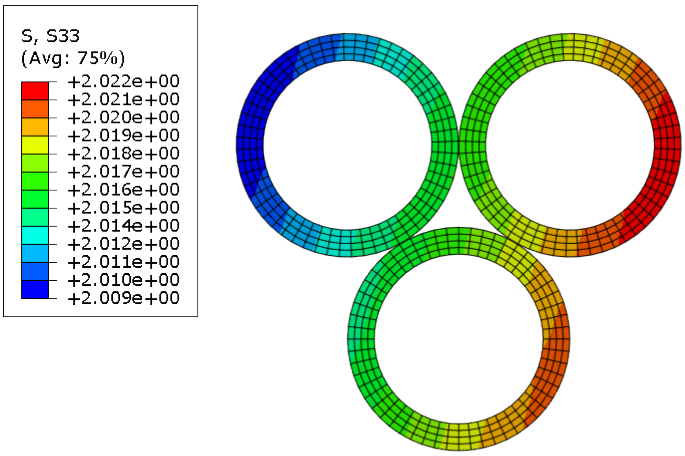

Figure 5.21: Axial stress in the insulation layer for sea state 1, stress range of 0.54 MPa

From this case, it is noted that the maximum axial stress in the XLPE is located at one of the sides. This is due to the bending displacement as explained in Section 3.2.2.

From Equations (4) and (5), the bending and axial stresses are defined below.

$$\begin{cases} \sigma_{bending} = \dfrac{2.022 - 2.009}{2} = 0.007\ MPa \\ \sigma_{axial} = 2.022 - 0.013 = 2.015\ MPa \end{cases} \quad (21)$$

According to Table 4.6, and to the combination of both stresses, the displacements of sea state 1 do not imply stresses large enough to propagate the crack. Hence, sea state 1 does not influence the fatigue life of the studied cable.

5.1.6.2 Sea state 2

Hence, the same simulations have been done for sea state 2. Figure 5.22 shows the axial stress distribution in the insulation layer after computation of the displacements of sea state 2 from Table 5.1.

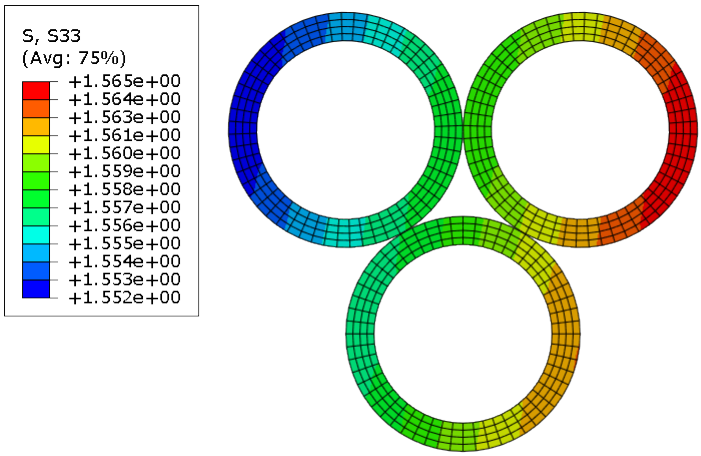

Figure 5.22: Axial stress in the insulation layer for sea state 2, stress range of 0.91 MPa

From Equations (4) and (5), the bending and axial stresses of this simulation are defined below.

$$\begin{cases} \sigma_{bending} = \dfrac{1.565 - 1.552}{2} = 0.007\ MPa \\ \sigma_{axial} = 1.565 - 0.007 = 1.558\ MPa \end{cases} \quad (22)$$

Same as sea state 1, the stresses are not large enough to propagate the crack. Sea state 2 does not influence the fatigue life of the XLPE layer.

5.1.6.3 Sea state 5

Finally, the simulation for sea state 5 is made and the results are presented. Hence, the displacements of the highest stress range of the sea state are first implemented in ABAQUS (2020). the final axial stresses found in the XLPE are shown in Figure 5.23.

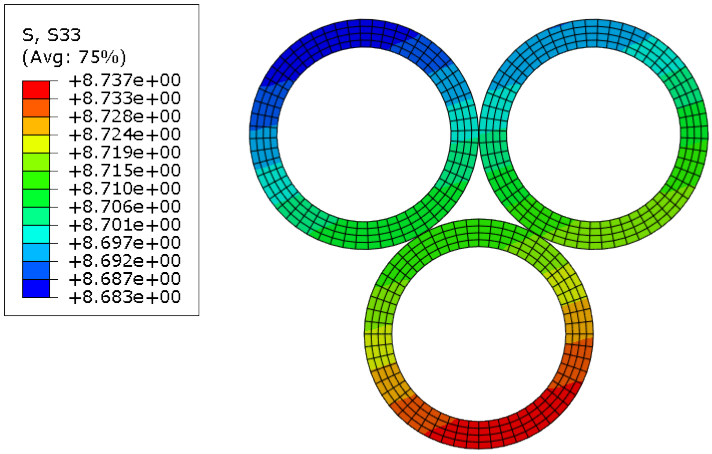

Figure 5.23: Axial stress in the insulation layer for sea state 3, stress range of 2.58 MPa

From Equations (4) and (5), the bending and axial stresses of the highest stress range for this sea state can be calculated.

$$\begin{cases} \sigma_{bending} = \dfrac{8.737 - 8.683}{2} = 0.027\ MPa \\ \sigma_{axial} = 8.737 - 0.027 = 8.710\ MPa \end{cases} \tag{23}$$

According to Table 4.6, the stresses are large enough to propagate the crack. Hence, the minimum crack size can be determined in addition to the fatigue damage accumulation related to these stresses. Hence, a crack size of 0.753 mm is required for this stress to have an impact on the fatigue damage of the cable. However, this crack size corresponds already to 57% of the insulation thickness. Then, it means that sea state 5 influences the fatigue life of the cable, nevertheless, this influence starts very late in the fatigue life of the cable.

Assuming that this crack size is now the initial crack size, it would need 72 million cycles to fail the cable using mechanical loads using sea state 5, which correspond to 2641 years.

Since the highest stress range might propagate the crack but has a very low influence over the lifetime of the cable, it is assumed that the results for other cases would lead to the same conclusion since the stress ranges are smaller.

5.1.6.4 Conclusion of the various sea states

From the results in this section, it can be concluded that the most critical location is located just after the bending stiffeners around 15 meters. Only this location has been investigated in this section. Other parts of the cable could have been selected, however, the first location has the highest fatigue damage accumulation and so, is more likely to fail before the rest of the cable.

In addition, in Section 4.1.1, it has been assumed that sea states 3 and 4 that correspond to a wave height of 0.5 meters and a wave period of 4.5 s and 2.5 s might not have an impact on the life expectancy of the cable. For sea state 1, it has been seen that even the highest stress range case does not propagate the crack which has a wave height of 1.5 meters and a wave period of 5.5 s. Hence, these results go in favour of this assumption.

From the results presented above, only sea state 5 showed a potential crack growth in the insulation layer with an initial crack size of 0.753 mm. From this value, and the life estimation, which is 2641 years, it can be concluded that the sea state has still a negligible influence on the fatigue life of the cable.

Hence, the conclusion is that the mechanical loads might not influence on the insulation fatigue life. However, it must not be forgotten that the cable is not fully accurate since the stiffnesses of the cable simulated do not correspond to the real cable. So, the introduction of the layup angle which decreases the axial and bending stiffnesses could lead to higher stresses in the XLPE insulation.

5.1.7 Determination of the fatigue life of the insulation layer along the length of the cable

As explained in Section 5.1.6.4, only sea state 5 slightly influences the crack propagation. Hence, the mechanical loads seem to have no impact on the fatigue life. However, in the slope of the thesis, this case only is still considered to give an example of how the fatigue life determination should have been carried on.

In theory, it would have been necessary to determine the crack growth depending on the seasons and when the sea states occur to have better accuracy. This was complicated to implement in this work, so neglect. To calculate the crack propagation, Equation (24) which corresponds to the crack growth from Paris's law is used.

$$a_{t+1} = a_t + CK^m(a_t) \tag{24}$$

where a_{t+1} is the crack size after an increment, a_t is the crack size before an increment, K is the stress intensity factor, C and m are the parameters of the SN-curve.

This crack growth formulation has been implemented on MATLAB (2020). The initial crack size has been taken as the minimum crack size needed to propagate the crack using these stresses. Figure 5.24 shows the crack propagation of the highest stress of load case 5 is simulated.

Figure 5.24 shows that the crack propagation is quite slow even when the crack is close to the critical crack length. The time needed for the initial crack of 0.753 mm to propagate until failure is 2641 years.

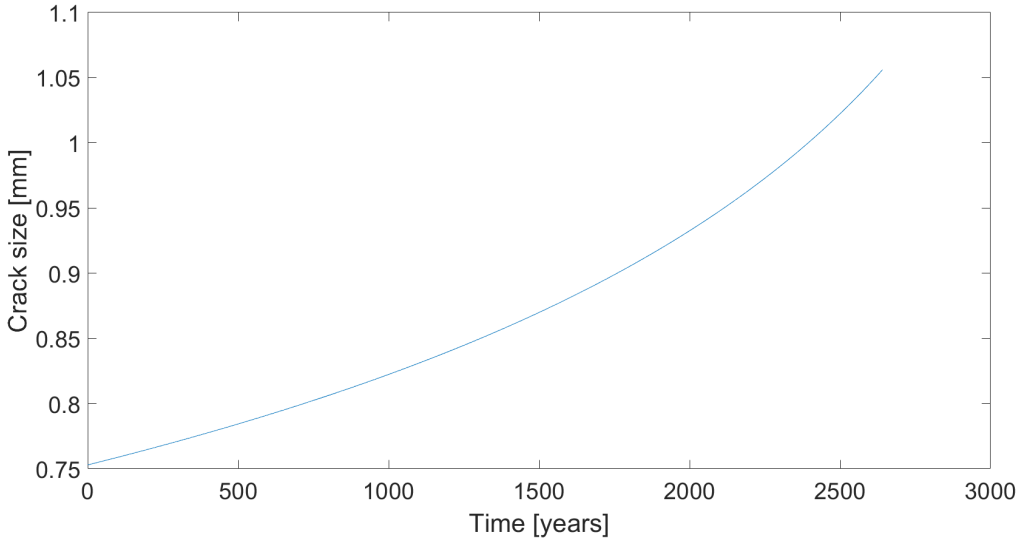

Figure 5.24: Crack propagation for the worst load case of sea state 5

Since reducing the initial crack size would result in no propagation of the crack from the mechanical stresses, a study has been made about the life expectancy for a larger initial crack size.

Table 5.2: Life expectancy for different initial crack size

Initial crack increase	+0%	+10%	+20%	+30%
Initial crack size [mm]	0.753	0.828	0.904	0.979
Percentage of the insulation thickness	71.3%	78.4%	85.6%	92.7%
Life expectancy [years]	2 641	1 572	853	357
Reduction of the life expectancy	-	40%	68%	86%

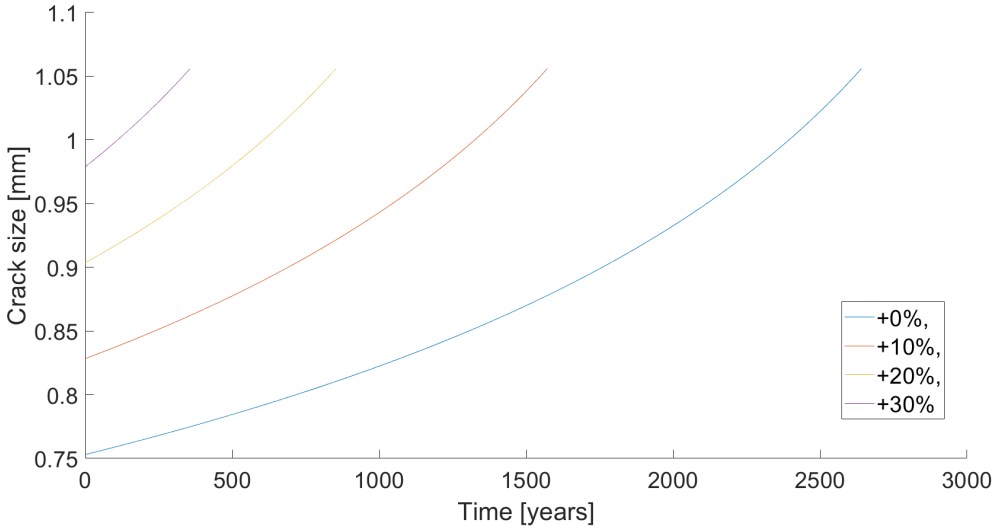

Figure 5.25: Crack growth for different initial crack sizes

From Table 5.2 and Figure 5.25, it can be concluded that a small increase in the initial crack size reduces by a lot the life expectancy. As an example, increasing the crack size by 30%, in this case, reduces the life expectancy by 86%.

In this section, the fracture mechanics model found in Section 4.3 with the use of Paris' law allows the estimation of the fatigue life from mechanical stresses using the highest stress from sea state 5. It can be concluded that with a crack size of 0.753 mm which allows the propagation of the crack from mechanical stresses, the estimation of the fatigue life has been found as 2641 years. An investigation of the initial crack size on the life expectancy showed that a small increase of 30% on the initial crack size reduces the life expectancy by 86%. From these results, it is concluded that the mechanical stresses do not have an important influence on the fatigue life of the cable. However, the initial crack size plays an important role in the cable fatigue life. Hence, using a large insulation thickness is best to reduce the impact of the mechanical stresses on the fatigue life. Moreover, these results were expected from the beginning since it has been found in the literature review that the Maxwell stresses have more impact on the fatigue life than the mechanical stresses. However, it must be remembered that these results consider a cable that does not match the theoretical mechanical properties.

Also, here only one load case has been considered for the fatigue life. If one wants to compute all the different sea states and stresses, the order of the stresses matter. Large stress at the beginning of the fatigue life of the cable would not have the same effect as the same stress at the middle of the fatigue life due to the size of the crack which would be different. Hence, to properly compute the cable fatigue life, every load and sea state must be selected randomly based on their probability of occurrence, and multiple simulations must be carried out to get a large sample.

5.2 Electrical results

The results from the electrical analyses can be divided into two sections the results linked with the inclusion of the impurity and the ones without. The latter is the simulation that was carried out first.

5.2.1 Electric field without impurity

This simulation result provides the initial estimation of the electric field around the cable that is not influenced by the presence of an impurity.

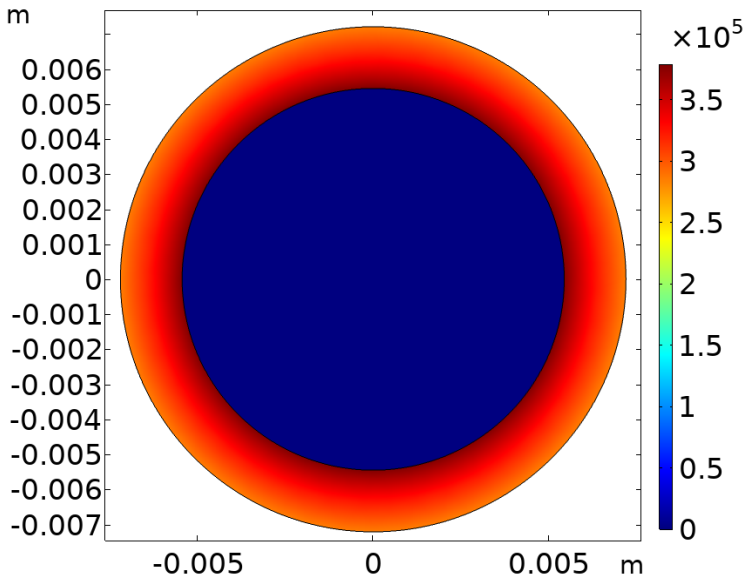

Figure 5.26: Electric field in V/m inside XLPE insulation without the impurity

Figure 5.26 shows the distribution of electric field in the XLPE of an underwater cable without the presence of impurity. The graph shows a gradient in the electric field distribution around the core of the cable. However, this gradient in an electric field is very small, this implies that the strength of the electric field exists almost at its full length throughout the thickness of the XLPE with a maximum value of $3.76 \cdot 10^5$ V/m. This result implies that when the impurity is introduced in the subsequent simulations, the impurity is going to experience the maximum electric field strength in the initial condition rather than having a gradual increase in the influencing electric field. The subsequent Maxwell stress that is generated would also be much higher since it is directly proportional to the square of the affecting electric field.

A higher existing field produces a higher Maxwell stress which is not good for the fatigue life of the cable since the time it takes for the water tree to grow may be substantially reduced to the increased in the Maxwell stress. This phenomenon can be attributed to the thickness of the XLPE insulation layer. A thicker layer of insulation results in a more gradual strengthening of the electric field this can cause the speed at which water tree grows to be lower. This is because the water tree will only experience gradually strengthening of electric field This would increase the fatigue life of the underwater cable.

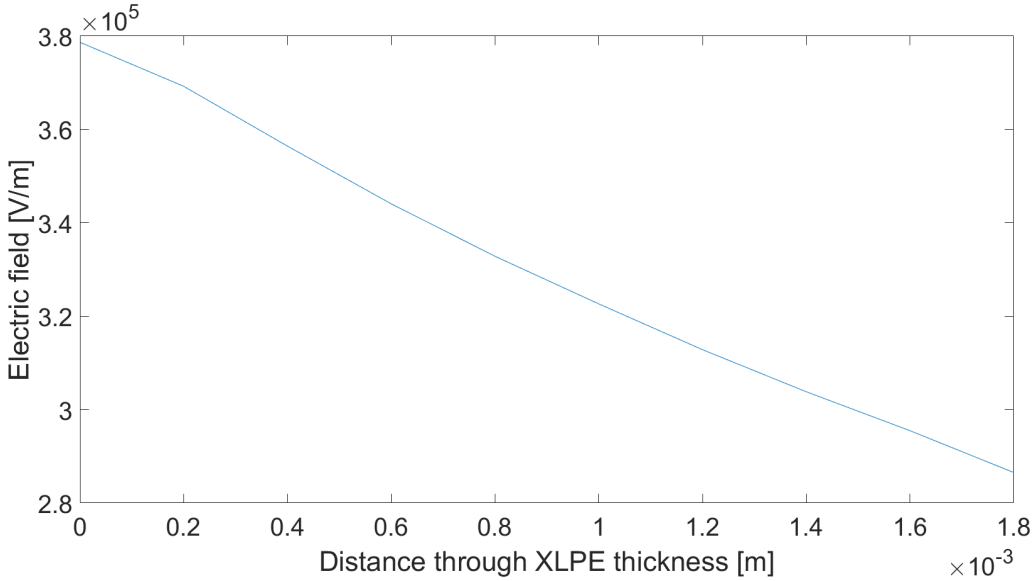

Figure 5.27: Variation of the electric field along the distance of the water tree from the core

The entire thickness of the XLPE layer is 1.76 mm which was divided into 10 equal sections of 0.176mm. The reason is to have uniform locations at which the electric field readings can be taken. The division also helps to identify the 60% thickness which is essentially the critical length at which the breakdown of the XLPE layer occurs.

5.2.2 Electric field with impurity

Section 5.2.1 provides an insight into how the electric field is present throughout the thickness of the XLPE. However, this is only applicable for an ideal cable. This section provides the results about the electric field in a cable with the presence of a water tree impurity. In this study, the investigation is about the presence of one single water tree. The situation where there are multiple water trees has not been investigated. Simulations involving multiple water trees can significantly increase the complexity of

the problem. In addition, Young (2019) states that the length of the water tree rather than the number of water trees influences the failure of the XLPE. It leads to the conclusion that investigating multiple water trees does not provide more significant results.

The parameters considered for the simulation are specified in Section 4.2.3 the electric field distribution can be seen in Figure 5.28.

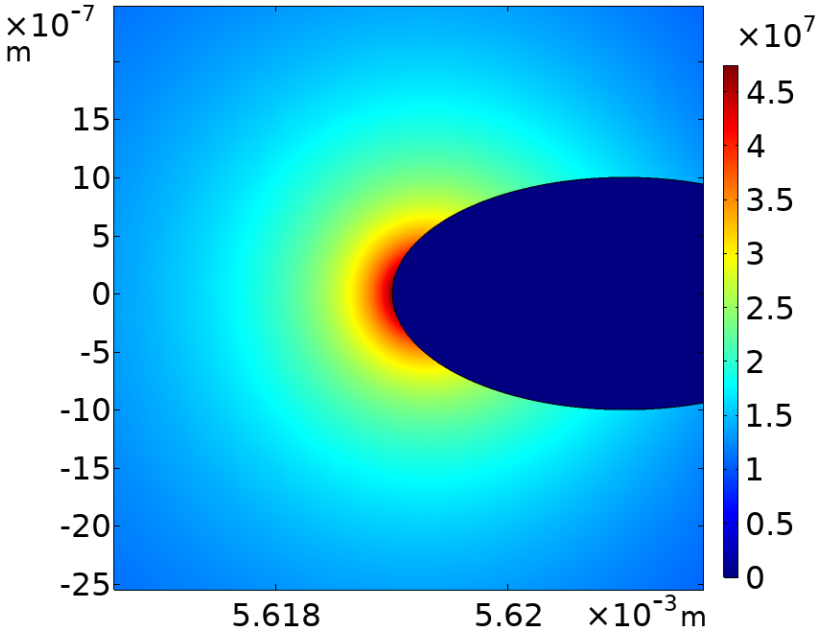

Figure 5.28: Electric field in V/m at the tip of water tree

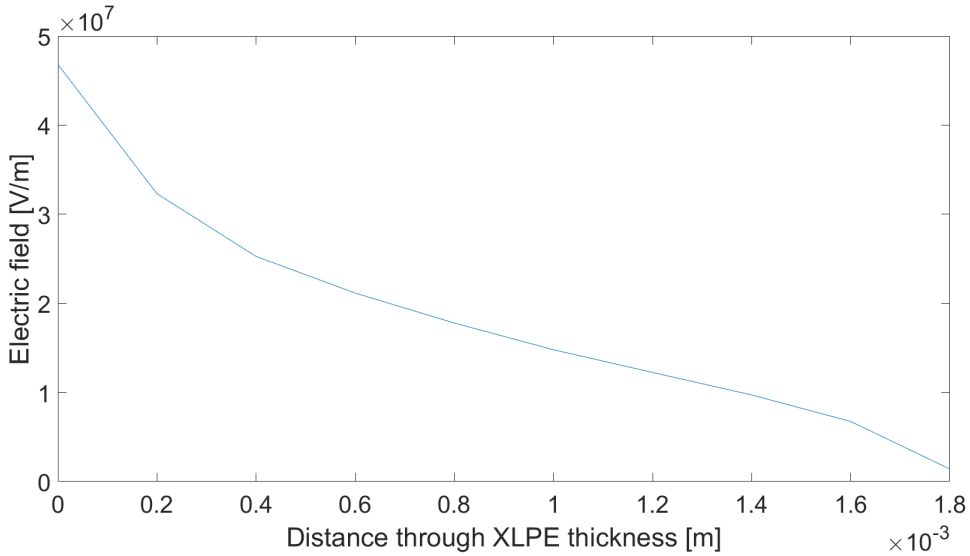

Figure 5.29: Variation in electric field with distance

From Figure 5.29, there is a severe change in the distribution of the electric field within the XLPE. A higher concentration of electric field is present at the tip of the water tree. This higher intensity of the electric field at the tip of the water tree is responsible for the degradation of the insulating material. It can also be observed that the length of the water tree increases the intensity of the electric field also increases, peaking at a maximum of $4.68 \cdot 10^7$ V/m, as seen in Figure 5.29. The increase in the water tree length replicates the phenomenon of the water tree gradually growing. Multiple simulations are carried out by incrementing the length of the rectangular channel region

with each increment being 0.176 mm in length. As the water tree continues to grow in length towards the conductor the intensity of the electric field continues to increase. This electric field continues to break the polymer chains and further propagates the crack, and the speed of this breakdown increases as the water tree approaches the conductor. It has been explained in Section 2.4.3 that the insulator breaks down when the crack length will reach 60% of the thickness of the XLPE.

Figure 5.30 compares the electric field variation with distance with and without impurity. It shows the significant increase in the concentration of electric field due to the presence of a water tree impurity; this result once more reaffirms the inference that is drawn from the initial results without impurity, the resulting maxwell stress in this case this situation will be significantly high and will drastically affect the fatigue life of the cable. The graph is on a log-normal scale to increase the clarity of the graph.

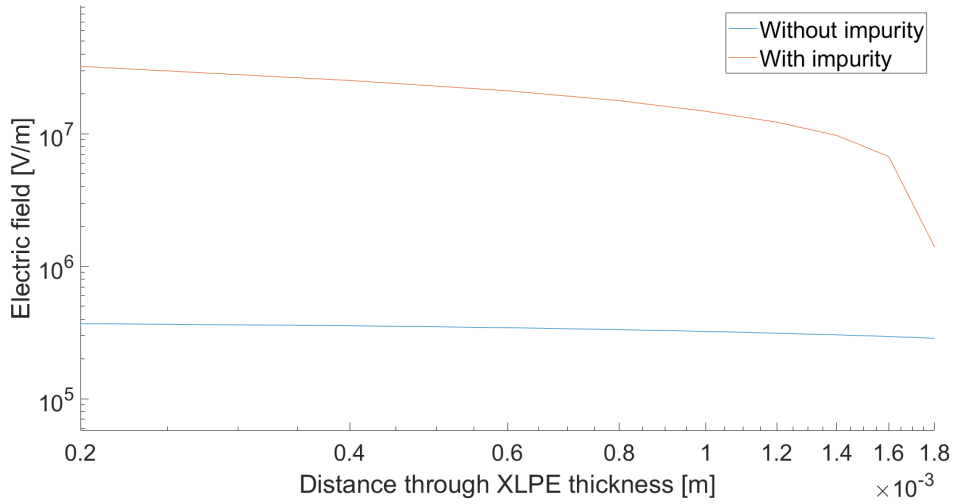

Figure 5.30: Comparison of the electric field in two cases

5.2.3 Maxwell stresses

The Maxwell stress associated with the water tree can be estimated using Equation (7) which shows that the Maxwell stress varies with respect to the distance from the conductor. This is because Maxwell Stress is directly proportional to the square of the electric field as per Equation (7).

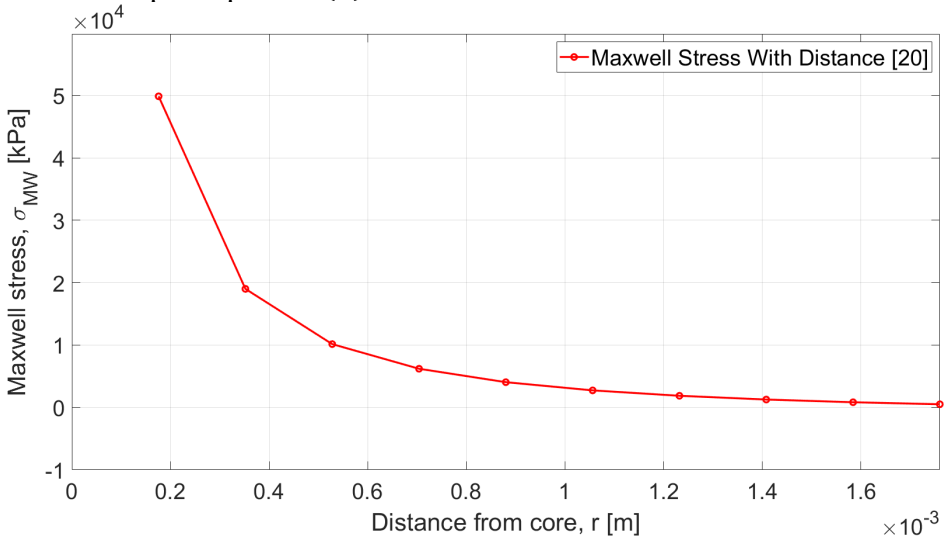

Figure 5.31: Maxwell stresses vs distance

Figure 5.31 shows the variation of Maxwell stress along the distance from the core. The Maxwell stress is only calculated till 90% of the thickness of the insulation layer, it should be noted that once the water tree grows to 60% of thickness dielectric failure of the insulation layer occurs.

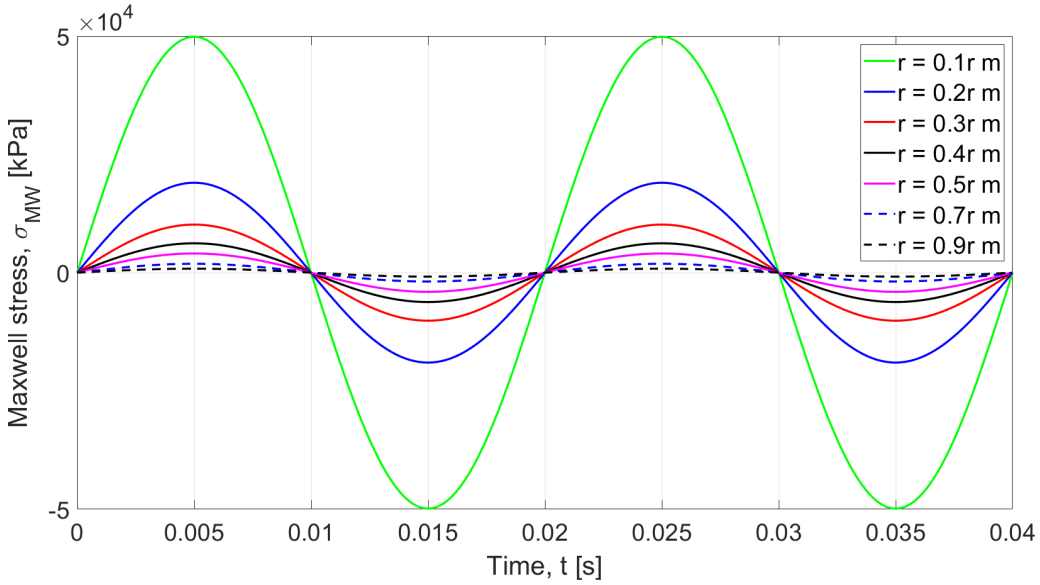

Figure 5.32: Cyclic Maxwell stresses

From Figure 5.32, it is observable that this sinusoidally varying Maxwell stress increases as it gets closer to the conductor. The Maxwell stress curve produced due to an AC current behaves sinusoidally alternating. The peak value of Maxwell stress is obtained when the water tree grows through 90% of the thickness peaking at $4.8 \cdot 10^4$ kPa. The Maxwell stress value at peak conditions and the limiting length is too high to provide any valid results for the calculation of life expectancy. As a result, the lowest Maxwell stress acting on the water tree impurity which occurs in the initial state is used in the calculation of fatigue life with respect to the Maxwell stress resulting in a fatigue life of 17.35 hours.

5.2.4 Electrical fatigue life

This section discusses the results of fatigue life calculation due to electrical stress. It can be seen from Young's (2019) work that the maximum Maxwell stress cycle amplitude for a water tree with an aspect ratio of two to four mm from the cable core which is the 60% critical length for study case is 4.3 kPa. This value results in the break of a maximum of 18 monomer chains in 10 minutes. In this study, however, the thickness of the insulation layer itself is limited to 1.76 mm resulting in much higher stress. Maxwell stress is obtained using the electric field simulations as described in Section 3.3 which is the principal factor of this calculation. This results in having a Maxwell stress of 6204 kPa. Based on Young's (2019) work and assuming direct similarity, the number of monomers broken in 10 minutes is estimated to be $2.6 \cdot 10^4$. These values allow the estimation of the growth rate for one minute. The limit length of 60% thickness of XLPE corresponding to 1.056 mm, sets the failure condition for the calculation of the fatigue life. A resume of the parameters used for the fatigue life are presented in Table 5.3.

Table 5.3: Electrical fatigue life calculation

Maxwell stress	6204 kPa
Monomer diameter	$329 \cdot 10^{-12}$ m
Monomers broken in 10 minutes	$2.6 \cdot 10^{4}$
Water tree growth in 10 minutes	$1.0 \cdot 10^{-5}$ m
Water tree growth in 1 minute	$1.0 \cdot 10^{-6}$ m
Limit length	$1.056 \cdot 10^{-3}$ m
Lifetime in minutes	1041 min
Lifetime in hours	17.35 hrs

From the calculation, the fatigue life is very small and since this value is based on the lowest Maxwell stress the crack experiences, and as the crack propagates the stress experienced also increases exponentially.

One of the reasons why the life is small is because of the thickness of the XLPE insulation layer. Assumptions have been made to carry out this calculation and its accuracy is under question, however, the steps needed to carry out this calculation can be considered as preliminary guides for similar works.

6 Summary and conclusions

Wave energy converters are potential sustainable energy sources that must be investigated. The main components required in the offshore power industry are the dynamic subsea cables that transport the produced electricity to distribution centres on land. The overall strength and life expectancy of these cables can determine the economic benefits of the offshore industry. The two main aspects affecting the strength of dynamic subsea cables are the mechanical stresses induced by the wave motions and the electric field disparity due to the presence of water trees.

From the literature review, the presence of a water tree affects the life expectancy of the dynamic subsea cables, reducing it by about two to five years (Young, 2019). Analyses carried out in the thesis provide an insight into how this defect grows.

Overall, this thesis presented a methodology to investigate the crack propagation from two distinct phenomena: motion-induced stresses and electrical-induced stresses produced by water trees in the insulation. The main goal was to determine the fatigue life of the cable from these two mechanisms. Individual assessments to estimate the fatigue life of the dynamic subsea cable are achieved. This work finally proposed a combined model estimating the cable fatigue life. However, it has not been feasible due to electrical results.

6.1 Mechanical simulations

First, this thesis contains a mechanical methodology based on the sub-modelling method. The sub-modelling approach consists of determining the global motions/displacements of the cable for different sea states. Then, these displacements are used on a local FE model to calculate the local stresses. Finally, the determination of the fatigue life is carried out using linear elastic fracture mechanics.

SIMA (2020) allowed to determine the global cable motions for different sea states. The fatigue damage accumulation along the cable length revealed a critical location located at the beginning of the cable. From this location, the local displacements have been extracted.

Then, the local displacements are applied as boundary conditions on the FE model in ABAQUS (2020) to get the local stresses in the XLPE layer. A few complications were encountered throughout the thesis. These complications made it impossible to create an accurate model. Hence, the work presented solutions by using a simplified model without a layup angle. From the simplified model, simulations showed a stress gradient across the cross-section. This gradient allowed the determination of the axial and bending stresses.

Then, different fracture mechanics models have been investigated and compared to determine the cable fatigue life. The model of an edge crack in a solid plane was the most critical and so selected. The minimum stress required to propagate the crack has been found as 7.21 MPa for the axial stress and 4.02 MPa for the bending stress if taken separately.

Using this fracture mechanics model and Paris' law, it has been possible to estimate the fatigue life from the mechanical stresses exploiting the load case from sea state 5. The

maximum axial and bending stresses have respectively been found as 8.710 MPa and 0.027 MPa. With an initial crack size of 0.753 mm, the estimation of the fatigue life is 2641 years. An investigation of the initial crack size on the life expectancy showed that an increase of 30% on the initial crack size reduces the life expectancy by 86%. Therefore, the thickness of the cable studied in this thesis can be considered too small.

These results mean that the influence of the mechanical stresses on the cable might be insignificant considering that the cables are designed to sustain 25-30 years and last only over two to five years due to water trees (Young, 2019). This result has been expected from the beginning since the literature review strongly suggests the Maxwell stresses have a faster influence. Also, the stresses and displacements from the fatigue damage accumulation were small and expected not to induce high stresses in the insulation layer.

6.2 Electrical simulations

Overall, a good understanding of the water tree phenomenon was achieved throughout this thesis. A methodology was developed to determine the influence of a water tree over the electric field in the cable. This work proposes a standard assessment of Maxwell stress from the electric field. The Maxwell stress determination led to an estimation of the cable fatigue life. However, this estimation must be reviewed for more accurate results.

The main goal was to develop a working model in COMSOL Multiphysics software (2020) to determine the distribution of the electric field with and without the presence of a water tree impurity. With this model, the electric field across the insulation layer was obtained with a maximum value at the tip of the water tree of $4.68 \cdot 10^7$ V/m. The electric field concentration at the tip of the water tree is much higher than the anticipated values from a similar study by Young (2019). The results of multiple simulations indicated that the thickness of the insulating XLPE layer is of utmost importance to the cable fatigue life. Then, the thickness of 1.76 mm is inadequate to accurately calculate the fatigue life with the Maxwell stress at 6204 kPa at 60% of XLPE thickness and a maximum at $5 \cdot 10^4$ kPa. Hence, the Maxwell stress might cause rapid material failure and reduce the fatigue life.

Finally, the lower thickness of the XLPE material resulting in higher electric field values even at a low voltage of 1 kV resulted in a life expectancy of 17.35 hours. The calculation of the life expectancy concerning electrical stress has been carried out with numerous assumptions. Hence, the accuracy of the result is in question. However, in the given timeframe, the methodology is effective for the current study case and may be helpful for future research models.

7 Future work

This chapter presents all the future work possible to improve the methodology, models, and results presented in the previous chapters. It is divided into sections to cover the various possibilities.

7.1 Model adjustments

Section 5.1.5 showed the impossibility of using the developed model due to inaccurate results. Even with different simulations, the investigation to improve the model revealed inaccurate results or unsolved computation errors. Hence, the potential issue of this work has been to compute a solid cable. As future work, it would be interesting to simulate only a short part of the solid cable located at the middle of the initial length that would be attached on its ends to beam elements. These beam elements could be configured to have the correct mechanical properties of the cable where ABAQUS (2020) sees them as a 1D model, which is very fast to compute. The eventual drawback of this solution is to confirm the continuity of the mechanical properties when it comes to the solid part. A disparity between the beam and the solid elements could lead to a non-uniform distribution of the stresses over the cable length. It would also induce inaccurate stresses in the XLPE layer.

In addition, the computation of some of the sea state cases failed whereas others were computed correctly. In this thesis, it is seen that multiple computers were necessary. It has been observed that depending on the computer and the number of CPUs used for the analysis, the computations might or might not be carried out. In some cases, the usage of 16 CPUs decreased the computation time but produced computation errors compared to the use of 4 CPUs.

7.2 Bending stiffness EI

It has been seen in Section 4.1.3.2 that the bending stiffness EI is not reachable even with the most complex model used in this work. It is because the wires were considered as a solid element. Hence, they increase the bending stiffness with extra material. It was impossible to simulate every wire since it would imply too many contact conditions that are time-consuming and produce computation errors.

Hence, a solution would have been to model each wire as a beam element. The use of beam elements is powerful since ABAQUS (2020) considers beam elements as 1D elements that decrease the computation time. In addition, it is possible to define the beam radius with the material in reach the axial and bending stiffnesses of a wire and so, of the entire cable. This solution has been investigated in this work however, it was not possible to reach the end of it due to lack of time. Nevertheless, the small results showed high potential for future work.

7.3 Friction

In Section 5.1.5.2, the results show that none of the displacements was large enough to induce contact between the different components. Hence, the assumption made along this work of a frictionless model might be wrong even if it has no effect in this work. In future work, the focus would be to investigate the friction coefficients using higher displacements to see the impact on the results.

Moreover, after the manufacturing process, there is an initial shrinking of the cable. It applies an initial pressure all over the cable circumference. This initial shrinking also involves a constant contact between the different components and potentially an initial penetration of some components in others. Hence, a full-stick condition might be more realistic than the friction coefficient defined in Section 2.3.1 but is yet to be investigated. The dimensions of the cable could be adjusted to imply an initial contact between the different components in ABAQUS (2020). In addition, a distributed pressure could be applied all around the cable. After all, the deformed geometry from this case could be used as initial undeformed geometry in ABAQUS (2020) to remove the residual stresses. However, there is still a lack of data concerning the initial pressure to be applied.

7.4 Sea states

In this work, only three sea states have been considered with a wave and wind direction of 0°. In future work, one can focus on considering other cases with different wave and wind directions, especially sea states with higher fatigue damage accumulation. The only issue is the lack of data about the combination of wave period, wave height, and directions which is hard to found. Also, in this work, only one load case has been investigated for each sea state. One can focus on simulating all the stress history to improve the accuracy of fatigue life.

7.5 Fatigue life

It has been assumed in this work that only one load case from sea state 5 would propagate the crack. One can focus on getting the data from all the sea states to compute a fracture mechanics model using Paris' law. For that, a random sea state and load case can be taken to propagate the crack. Overall, it is needed to make this procedure multiple times to get a good sample and plot the distribution of the failures over the lifetime of the cable.

7.6 Maxwell stresses and fatigue life

The principal assumption about Maxwell stress is that the relation between the stress cycle and the number of monomers broken is linear. However, this may not be the case and needs to be a focus for future work. The unit energy accumulated and the critical volume to which this energy is from Maxwell stress are crucial factors in determining the fatigue life of the cable (Tao et al., 2016). Combined fracture mechanics and crack propagation are only possible if this part of future work is correctly assessed.

7.7 Combined fatigue life model

One of the fundamental objectives of the thesis was to develop a combined model for determining water tree propagation in dynamic subsea cables. This model required combining both motion-induced and electrical-induced stresses that influence the crack growth and subsequently the fatigue life of the dynamic subsea cable caused by water trees. The methodology presented in Section 3.4 seems suitable for this task. However, the small contribution of mechanical loads towards crack growth and the significant influence of electrical loads has made this objective difficult.

8 References

Aderinto, T., & Li, H. (2018). Ocean Wave Energy Converters: Status and Challenges. *Energies*, *11*(5), 1250. https://doi.org/10.3390/en11051250

Anderson, T. L. (2005). *Fracture Mechanics: Fundamentals and Application* (3rd ed.). Taylor & Francis Group. https://doi.org/10.1201/9781420058215

ANSYS Inc. (2020). *Granta EduPack*. [Computer software]. https://www.ansys.com/products/materials/granta-edupack

Astariz, S., & Iglesias, G. (2015). The economics of wave energy: A review. *Renewable and Sustainable Energy Reviews*, 45, 397-408. https://doi.org/https://doi.org/10.1016/j.rser.2015.01.061

Chen, J. L., & Filippini, J. C. (1993). The morphology and behavior of the water tree. *IEEE Transactions on Electrical Insulation*, *28*(2), 271–286. https://doi.org/10.1109/14.212252

COMSOL Inc. (2020). *COMSOL Multiphysics* (Version 5.6) [Computer software]. https://www.comsol.co.in/

Crine, J. P. (1998). Electrical, chemical and mechanical processes in water treeing. *IEEE Transactions on Dielectrics and Electrical Insulation, 5*(5), 681-694. https://doi.org/10.1109/94.729690

Dassault Systèmes Simulia Corp. (2020). *ABAQUS* (Version 2020.HF3) [Computer software]. https://www.3ds.com/products-services/simulia/products/abaqus/

de Wild, F. (2018). *Offshore wind industry joins forces to reduce costs of cable failures*. Available at: https://www.dnv.com/news/offshore-wind-industry-joins-forces-to-reduce-costs-of-cable-failures-117811 [Accessed 15 June 2021]

Dissado, L. A., Danikas, M. G., Champion, J. V., & Dodd, S. J. (1998). Propagation of electrical tree structures in solid polymeric insulation [comment and reply]. *IEEE Transactions on Dielectrics and Electrical Insulation*, *5*(3), 458–460. https://doi.org/10.1109/94.689435

Dowling, N. E. (2007). *Mechanical Behavior of Materials: Engineering Methods for Deformation, Fracture, and Fatigue* (3rd ed.) Pearson.

Dowling, N. E. (2013). *Mechanical Behavior of Materials: Engineering Methods for Deformation, Fracture, and Fatigue* (4th ed.) Pearson.

DNV (2020). *HELICA* [Computer software]. https://www.dnv.com/services/umbilical-analysis-and-flexible-pipe-analysis-helica-69553

DNV (2020). *SESAM* [Computer software]. https://www.dnv.com/services/strength-assessment-of-offshore-structures-sesam-software-1068

DNV (2020). *SIMA* (Version 3.7) [Computer software]. https://www.dnv.com/services/marine-operations-and-mooring-analysis-software-sima-2324

Engineering ToolBox (2004). *Friction and Friction Coefficients*. Available at: https://www.engineeringtoolbox.com/friction-coefficients-d_778.html [Accessed 10 February 2021]

European Union (2012). *Energy roadmap 2050*. Available at: https://europeanpowergeneration.eu/files/Energy_Roadmap_2050pdf.pdf [Accessed 15 November 2020]

Eurostat (2020). *Share of renewable energy in the EU up to 18.0%.* Available at: https://ec.europa.eu/eurostat/documents/2995521/10335438/8-23012020-AP-EN.pdf/292cf2e5-8870-4525-7ad7-188864ba0c29 [Accessed 15 November 2020]

Faiz, J., & Nematsaberi, A. (2017). Linear electrical generator topologies for direct-drive marine wave energy conversion - an overview. *IET Renewable Power Generation*. https://doi.org/10.1049/iet-rpg.2016.0726

Falcão, A. F. D. O. (2010). Wave energy utilization: A review of the technologies. *Renewable and Sustainable Energy Reviews, 14(3)*, 899–918. https://doi.org/10.1016/j.rser.2009.11.003

Gallaghar, J.P., Giessler, F.J., & Berens, A.P. (1984). *USAF Damage Tolerant Design Handbook: Guidelines for the Analysis and Design of Damage Tolerant Aircraft Structures*

GCube (2016). *Down to the Wire: An Insurance Buyer's Guide to Subsea Cabling Incidents.* GCube Insurance Services. Available at: http://www.gcube-insurance.com/reports/down-to-the-wire/

Hvidsten, S., Ildstad, E., Sletbak, J., & Faremo, H. (1998). Understanding water treeing mechanisms in the development of diagnostic test methods. *IEEE Transactions on Dielectrics and Electrical Insulation*, *5*(5), 754–760. https://doi.org/10.1109/94.729699

Kaldellis, J. K., & Kapsali, M. (2013). Shifting towards offshore wind energy—Recent activity and future development. *Energy Policy*, *53*, 136–148. https://doi.org/10.1016/j.enpol.2012.10.032

Kuznecovs, A., Ringsberg, J. W., Yang, S.-H., Johnson, E., & Anderson, A. (2019). A methodology for design and fatigue analysis of power cables for wave energy converters. *International Journal of Fatigue*, 122, 61–71. https://doi.org/10.1016/j.ijfatigue.2019.01.011

Minitry of the Environment (2019). *Sweden's draft intergrated national energy and climate plan.* Government Offices of Sweden. Available at: https://www.government.se/reports/2019/01/swedens-draft-integrated-national-energy--and-climate-plan/ [Accessed 11 December 2020]

Radon, J. C. (1980). Fatigue crack growth in polymers. *International Journal of Fracture*, *16*(6), 533–552. https://doi.org/10.1007/bf02265216

Ringsberg, J. W., Bjarnehed, H., Johansson, A., & Josefson, B. L. (2000). Rolling contact fatigue of rails—finite element modelling of residual stresses, strains and crack initiation. *Proceedings of the Institution of Mechanical Engineers, Part F: Journal of Rail and Rapid Transit*, 214(1), 7–19. https://doi.org/10.1243/0954409001531207

Shaw, M., & Shaw, S. (1984). Water Treeing in Solid Dielectrics. *IEEE Transactions on Electrical Insulation, EI-19*(5), 419-452. https://doi.org/10.1109/tei.1984.298768

Sönnichsen, N. (2020). *Net consumption of electricity worldwide from 1980 to 2017*. Statista. Available at: https://www-statist com.eu1.proxy.openathens.net/statistics/280704/world-power-consumption/ [Accessed 11 November 2020]

Sweeney, J. (1988). The stress intensity for an edge crack in a semi-infinite orthotropic body. *International Journal of Fracture*, *37*(3), 233–241. https://doi.org/10.1007/bf00045865

Tanaka, T., Fukuda, T., & Suzuki, S. (1976). Water tree formation and lifetime estimation in 3.3 kV and 6.6 kV XLPE and PE power cables. *IEEE Transactions on Power Apparatus and Systems*, *95*(6), 1892–1900. https://doi.org/10.1109/t-pas.1976.32290

Tao, W., Ma, Z., Wang, W., Liu, J., Zhou, K., Li, T., & Huang, M. (2016). *The mechanism of water tree growth in XLPE cables based on the finite element method*. https://doi.org/10.1109/ichve.2016.7800764

The Math Works, Inc. (2020). *MATLAB* (Version 2020a) [Computer software]. https://www.mathworks.com/

Wang, Z., Marcolongo, P., Lemberg, J. A., Panganiban, B., Evans, J. W., Ritchie, R. O., & Wright, P. K. (2012). Mechanical fatigue as a mechanism of water tree propagation in TR-XLPE. *IEEE Transactions on Dielectrics and Electrical Insulation*, *19*(1), 321–330. https://doi.org/10.1109/tdei.2012.6148534

Xu, J. J., & Boggs, S. A. (1994). The chemical nature of water treeing: theories and evidence. *IEEE Electrical Insulation Magazine*, *10*(5), 29–37. https://doi.org/10.1109/57.318803

Yang, S.-H. (2018). *Analysis of the Fatigue Characteristics of Mooring Lines and Power Cables for Floating Wave Energy Converters* [Doctor of Philosophy, Chalmers University of Technology]. ResearchGate. https://doi.org/10.13140/RG.2.2.28560.66562

Yang, S.-H., Ringsberg, J. W., & Johnson, E. (2018). Parametric study of the dynamic motions and mechanical characteristics of power cables for wave energy converters. *Journal of Marine Science and Technology*, *23*(1), 10–29. https://doi.org/10.1007/s00773-017-0451-0

Zhang, Y., Zhao, Y., Sun, W., & Li, J.. (2021). Ocean wave energy converters: Technical principle, device realization, and performance evaluation. *Renewable and Sustainable Energy Reviews*, *141*, 110764. https://doi.org/10.1016/j.rser.2021.110764

9 Appendix

9.1 Mechanical crack propagation

```
clear
close all
addpath('Crack_Progagation_functions')

%% Initialisation of the variables

%%%%%%%%%%%%%%%%%%%%%
% Crack properties %
%%%%%%%%%%%%%%%%%%%%%

thickness_XLPE = 1.76e-3; %m

crack_init = 0.753e-3;                  % Initial crack length [m]
percentage_added = [0, 0.1, 0.2, 0.3];
failure = 0.6;                          % Percentage of the layer needed to
fail
crack_end = thickness_XLPE*failure;     % Final crack length [m], failure%
of the insulation material

crackcase = 3;
cases = ["CASE #1: edge crack in semi-infite body (axial stress)", "CASE #2:
thumbnail crack in solid cylinder (axial+bending stress)", ...
"CASE #3: single edge through crack in plate (axial+bending stress)", "CASE
#4: elliptical surface crack in plate (axial+bending stress)"];
step = 1e3;                             % Stress amplitude amplifier Delta_a
"blocks"/"steps" for faster "initial" propagation

%%%%%%%%%%%%%%%%%%%%%%%%%%%
% Initialisation time step %
%%%%%%%%%%%%%%%%%%%%%%%%%%%

frequency_mecha = 1/1200;   %Hz
t_mecha = 1/frequency_mecha;

Probability_sea_states = [0, 0, 0, 0, 100]/100;
Sea_state_1 = [0,0,0,0];
Sea_state_2 = [0,0,0,0];
Sea_state_5 = [1, 0.027, 8.710, 0.753];

n1 = 1;
n2 = length(Sea_state_2);
n5 = length(Sea_state_5);

frequency_elect = 50;       %Hz
t_elect = 1/frequency_elect;

t_inc = min(t_mecha);

inc_stop = 10;

%%%%%%%%%%%%%%%%%%%%%%%
% Material properties %
%%%%%%%%%%%%%%%%%%%%%%%

material=2;     % 1=steel, 2=XLPE

if material==1
    % Steel
    Kth=2;      % [MPa*m1/2]
    KIc=60;     % [MPa*m1/2]
    C=2.47e-9;  % Growth rate mm/cycle, load in MPa
    m=3.33;     % Fatigue crack exponent
```

```
else
    % XLPE NOTE: data from Young ref [42], see Matlab code Parislaw.
    %Kth=0.69;     % [MPa*m1/2]
    Kth=0.5;
    KIc=10;        % [MPa*m1/2], "JR guessed"
    C=3.8874e-7;  % From Parislaw.m, growth rate m/cycle, load in MPa
    m=7.5295;      % From Parislaw.m
end

%%%%%%%%%%%%%%%%%%%%%%%%%%%%%%%
% Cross-section geometry data %
%%%%%%%%%%%%%%%%%%%%%%%%%%%%%%%

D=10e-3;       % Diameter [m] of the solid cylinder CASE #2
b=D;           % Plate width, same as D [m], CASE #3
t=100e-3;      % Plate thickness [m], CASE #3 and #4
c=0.25e-3;     % Half axis of ellipse [mm], crack geometry CASE #4

%%%%%%%%%%%%%%%%%%
% Stress cycles %
%%%%%%%%%%%%%%%%%%

% Stress amplitude [MPa], R=0

if material==1 % Steel, A=axial stress, B=bending stress
    sigmaA1=100; sigmaA2=100; sigmaA3=100;
    sigmaB1=100; sigmaB2=100; sigmaB3=100;
end

if material==2 % XLPE, A=axial stress, B=bending stress
    sigmaA1=8.710; sigmaA2=8; sigmaA3=8;
    sigmaB1=0.027; sigmaB2=0; sigmaB3=0;
end

sigma = [sigmaA1, sigmaB1];

%% Crack propagation

figure(1)
xlabel("Time [years]")
ylabel("Crack size [mm]")
title('Crack propagation for an different initial crack sizes')
legend_temp = '';

for n = 1:length(percentage_added)
    i = 1;
    time = 0;
    inc_mecha = 0;
    inc_elect = 0;
    crack(i) = crack_init*(1+percentage_added(n)); %#ok<SAGROW>

    if n == length(percentage_added)
        leg{n}=sprintf('+%d%c',percentage_added(n)*100, '%');
    else
        leg{n}=sprintf('+%d%c%c',percentage_added(n)*100, '%', ',');
    end
    cycles_mecha = 0;
    cycles_elect = 0;

    % Check if the crack did not reach the critical length
    while crack(i) < crack_end %crack_end*thickness_XLPE
        % Time step increment
        time = time + t_inc;
        % Initialisation of the variables to avoid an error line 131
        mecha_growth = 0;
        elect_growth = 0;

        if time/t_mecha - inc_mecha >= 1
```

```
        Matrix_1 = Sea_state_1(:,:).*(Sea_state_1(:,4) <=
    ones(n1,1)*crack(i)*1000);
        Matrix_2 = Sea_state_2(:,:).*(Sea_state_2(:,4) <=
    ones(n2,1)*crack(i)*1000);
        Matrix_5 = Sea_state_5(:,:).*(Sea_state_5(:,4) <=
    ones(n5,1)*crack(i)*1000);

        mecha_growth_temp = 0;

        for i_case = 5 %[1,2,5]

            eval(sprintf("Matrix_temp = Matrix_%d;",
         i_case))
            eval(sprintf("n_temp = n%d;", i_case))

            for j=1:1
                if Matrix_temp(j,1) ~=0
                    sigma = Matrix_temp(j,[3,2]);
                    occ = Matrix_temp(j, 1);

                    % Mechanical growth depending of the case
                    if crackcase == 1
                        mecha_growth_temp = fun_crackcase1(crack(i),
                              sigma, C, m, Kth, step*occ);
                    elseif crackcase == 2
                        mecha_growth_temp = fun_crackcase2(crack(i),
                              sigma, C, m, Kth, step*occ, D);
                    elseif crackcase == 3
                        mecha_growth_temp = mecha_growth_temp +
                              Probability_sea_states(i_case)*
                              fun_crackcase3(crack(i), sigma, C, m, Kth,
                              step*occ, b);
                    elseif crackcase == 4
                        [mecha_growth_temp, c] =
                              fun_crackcase4(crack(i), sigma, C, m, Kth,
                              step*occ, b, c, t);
                    else
                        error("Crack case " + crackcase + " does not
                              correspond to any case implemented.")
                    end
                end
            end
        end

        mecha_growth = mecha_growth_temp;

        if mecha_growth > 0
            cycles_mecha = cycles_mecha + 1;
        end

        inc_mecha = inc_mecha + 1;
    end

    if time/t_elect - inc_elect >= 1
        % Electrical growth due to Maxwell stresses
        elect_growth = 0;

%         %
%         Electrical crack propagation to be implemented here
%         %
%
%         if elect_growth > 0
%             cycles_elect = cycles_elect + 1;
%         end

        inc_elect = inc_elect + 1;
    end

    % Crack propagation
    crack(i+1) = crack(i) + elect_growth + mecha_growth;
```

```
        i = i+1;

        % If there is no crack propagation
        if i > inc_stop + 1
            if crack(i-inc_stop) == crack(i)
                error(['The crack propagation is 0mm for more than ',
                    num2str(inc_stop) , ' increments'])
            end
        end
    end

        %% Display
    disp('***')
    disp(cases(crackcase))
    disp(['Initial crack size of: ', num2str(crack_init*1000), 'mm (+',
       num2str(percentage_added(n)*100), '%)'])
    disp(['Number of mechanical stress cycles: ',
       num2str(cycles_mecha*step), 'cycles'])
    disp(['Number of electrical stress cycles: ', num2str(cycles_elect),
       'cycles'])
    disp(['Final time: ', num2str(time*step), 'seconds'])
    disp(['Final time: ', num2str(time*step/60/60/24/365.25), 'years'])
    disp(' ')

    %% Plot

    % Update of the figure containing the different initial crack size
    figure(1)
    hold on
    time_crack = (0:length(crack)-1)*step*t_mecha/60/60/24/365.25;
    x = time_crack;
    y = crack*1000;
    plot(x, y)

    % Plot the figure for the specific initial crack size
    figure(n+1)
    plot(x, y)
    title(['Crack propagation for an initial crack size of: ',
       num2str(crack_init*1000), 'mm (+', num2str(percentage_added(n)*100),
       '%)'])
    xlabel("Time [years]")
    ylabel("Crack size [mm]")

    %% Reset
    clear cycles_mecha cycles_elect time time_crack crack x y inc_elect
inc_mecha
end

figure(1)
legend(leg)
```

9.2 Crack propagation case #1

```
%% CASE #1: edge crack in semi-infite body (axial stress)

% Check if K>Kth
f=1.12;
K_check=f*max(sigmaA)*sqrt(pi*ai);

K=0; a1=ai; i=1;

if K_check>Kth
    while (a1<af)&&(K<KIc)
        K=f*sigmaA(i)*sqrt(pi*a1);
        if K>Kth
            growth1=(C*K^m)*1e-3*step; % Growth m/cycle
            a1=a1+growth1;
            %disp(num2str(a1));
        end
```

```
        K1(i)=K;
        crack1(i)=a1;
        N1(i)=i;
        i=i+1;
    end
end
disp(' ')
disp('***')
disp('CASE #1: edge crack in semi-infite body (axial stress)')
if K_check<Kth
    disp(' ')
    disp('K_check<Kth')
    disp(' ')
end
if K_check>Kth
    disp(['Crack length: ',num2str(crack1(i-1)),' mm'])
    disp(['Stress intensity factor: ',num2str(K1(i-1)),' MPa*m^.5'])
    disp(['Number of stress cycles: ',num2str(N1(i-1)*step),' cycles'])
    disp('***')
    disp(' ')
end

K_check1=K_check;

%% Error check
%#ok<*SAGROW>
```

9.3 Crack propagation case #2

```
%% CASE #2: thumbnail crack in solid cylinder (axial+bending stress)

% Check if K>Kth
beta=0.5*pi*ai/D; % a=crack depth, D=diameter of cylinder
H=1-sin(beta);
G=0.92*(2/pi)*sec(beta)*sqrt((tan(beta)/beta));
Yb=G*(0.923+0.199*H^4);              % Bending
Ya=G*(0.752+1.286*beta+0.37*H^3);    % Axial, tension
K_check=(Ya*max(sigmaA)+Yb*max(sigmaB))*sqrt(pi*ai);

K=0; a2=ai; i=1;

if K_check>Kth
    while (a2<af)&&(K<KIc)
        beta=0.5*pi*a2/D; % a=crack depth, D=diameter of cylinder
        H=1-sin(beta);
        G=0.92*(2/pi)*sec(beta)*sqrt((tan(beta)/beta));
        Yb=G*(0.923+0.199*H^4);              % Bending
        Ya=G*(0.752+1.286*beta+0.37*H^3);    % Axial, tension
        K=(Ya*sigmaA(i)+Yb*sigmaB(i))*sqrt(pi*a2);
        if K>Kth
            growth2=(C*K^m)*1e-3*step;
            a2=a2+growth2;
            %disp(num2str(a2));
        end
        K2(i)=K;
        crack2(i)=a2;
        N2(i)=i;
        i=i+1;
    end
end
disp(' ')
disp('***')
disp('CASE #2: thumbnail crack in solid cylinder (axial+bending stress)')
if K_check<Kth
    disp(' ')
    disp('K_check<Kth')
    disp(' ')
end
```

```
if K_check>Kth
    disp(['Crack length: ',num2str(crack2(i-1)),' mm'])
    disp(['Stress intensity factor: ',num2str(K2(i-1)),' MPa*m^.5'])
    disp(['Number of stress cycles: ',num2str(N2(i-1)*step),' cycles'])
    disp('***')
    disp(' ')
end

K_check2=K_check;

%% Error check
%#ok<*SAGROW>
```

9.4 Crack propagation case #3

```
%% CASE #3: single edge through crack in plate (axial+bending stress)

% Check if K>Kth
alpha=ai/b;  % a=crack depth, b=plate width
Yb=sqrt((2/(pi*alpha))*tan((pi*alpha)/2))*((0.923+0.199*(1-
sin((pi*alpha)/2))^4)/(cos(pi*alpha)/2));
Ya=0.265*(1-alpha)^4+(0.857+0.265*alpha)/(1-alpha)^(3/2);
K_check=(Ya*max(sigmaA)+Yb*max(sigmaB))*sqrt(pi*ai);

K=0; a3=ai; i=1;

if K_check>Kth
        while (a3<af)&&(K<KIc)
            alpha=a3/b;  % a=crack depth, b=plate width
            Yb=sqrt((2/(pi*alpha))*tan((pi*alpha)/2))*((0.923+0.199*(1-
sin((pi*alpha)/2)^4))/(cos(pi*alpha)/2));
            Ya=0.265*(1-alpha)^4+(0.857+0.265*alpha)/(1-alpha)^(3/2);
            K=(Ya*sigmaA(i)+Yb*sigmaB(i))*sqrt(pi*a3);
            if K>Kth
                growth3=(C*K^m)*1e-3*step;
                a3=a3+growth3;
                %disp(num2str(a3));
            end
            K3(i)=K;
            crack3(i)=a3;
            N3(i)=i;
            i=i+1;
        end
end

disp(' ')
disp('***')
disp('CASE #3: single edge through crack in plate (axial+bending stress)')
if K_check<Kth
    disp(' ')
    disp('K_check<Kth')
    disp(' ')
end
if K_check>Kth
    disp(['Crack length: ',num2str(crack3(i-1)),' mm'])
    disp(['Stress intensity factor: ',num2str(K3(i-1)),' MPa*m^.5'])
    disp(['Number of stress cycles: ',num2str(N3(i-1)*step),' cycles'])
    disp('***')
    disp(' ')
end

K_check3=K_check;

%% Error check
%#ok<*SAGROW>
```

9.5 Crack propagation function case #4

```
%% CASE #4: elliptical surface crack in plate (axial+bending stress)

% Note: this code allows the width of the crack (2c) two grow without
% limitations on af (or cf). It is the af through thickness (a) that limits
the
% boundary of crack propagation.

% Check if K>Kth
a=ai;
alpha=a/b;  % a=crack depth, b= plate width

% Analysis of a-tip (crack depth)
fi=90; % 0 at c-tip, 90 at a-tip (full depth of crack)
if a<=c
    Q=1+1.464*(a/c)^1.65;
    M1=1.13-0.09*(a/c);
    M2=-0.54+0.89/(0.2+(a/c));
    M3=0.5-1/(0.65+(a/c))+14*(1-(a/c))^24;
    f1=((a/c)^2*(cos(fi))^2+(sin(fi))^2)^0.25;
    f2=(sec(pi*c/2/b*sqrt((a/t))))^0.5;
    g=1+(0.1+0.35*(a/t)^2)*(1-sin(fi))^2;
    p=0.2+(a/c)+0.6*(a/t);
    G11=-1.22-0.12*(a/c);
    G21=0.55-1.05*(a/c)^(3/4)+0.47*(a/c)^(3/2);
    H1=1-0.34*(a/t)-0.11*(a/c)*(a/t);
    H2=1+G11*(a/t)+G21*(a/t)^2;
else
    Q=1+1.464*(c/a)^1.65;
    M1=sqrt(c/a)*(1+0.04*(c/a));
    M2=0.2*(c/a)^4;
    M3=-0.11*(c/a)^4;
    f1=((c/a)^2*(sin(fi))^2+(cos(fi))^2)^0.25;
    f2=(sec(pi*c/2/b*sqrt((a/t))))^.5;
    g=1+(0.1+0.35*(c/a)*(a/t)^2)*(1-sin(fi))^2;
    p=0.2+(c/a)+0.6*(a/t);
    G11=-0.04-0.41*(c/a);
    G12=0.55-1.93*(c/a)^(3/4)+1.38*(c/a)^(3/2);
    G21=-2.11-0.77*(c/a);
    G22=0.55-0.72*(c/a)^(3/4)+0.14*(c/a)^(3/2);
    H1=1+G11*(a/t)+G12*(a/t)^2;
    H2=1+G21*(a/t)+G22*(a/t)^2;
end

F=(M1+M2*(a/t)^2+M3*(a/t)^4)*f1*f2*g;
H=H1+(H2-H1)*(sin(fi))^p;
Ya=F*sqrt(1/Q);
Yb=H*Ya;
K_check_atip=(Ya*max(sigmaA)+Yb*max(sigmaB))*sqrt(pi*a);

% Analysis of c-tip (crack width)
fi=0; % 0 at c-tip, 90 at a-tip (full depth of crack)
if a<=c
    Q=1+1.464*(a/c)^1.65;
    M1=1.13-0.09*(a/c);
    M2=-0.54+0.89/(0.2+(a/c));
    M3=0.5-1/(0.65+(a/c))+14*(1-(a/c))^24;
    f1=((a/c)^2*(cos(fi))^2+(sin(fi))^2)^0.25;
    f2=(sec(pi*c/2/b*sqrt((a/t))))^0.5;
    g=1+(0.1+0.35*(a/t)^2)*(1-sin(fi))^2;
    p=0.2+(a/c)+0.6*(a/t);
    G11=-1.22-0.12*(a/c);
    G21=0.55-1.05*(a/c)^(3/4)+0.47*(a/c)^(3/2);
    H1=1-0.34*(a/t)-0.11*(a/c)*(a/t);
    H2=1+G11*(a/t)+G21*(a/t)^2;
else
    Q=1+1.464*(c/a)^1.65;
    M1=sqrt(c/a)*(1+0.04*(c/a));
```

```
    M2=0.2*(c/a)^4;
    M3=-0.11*(c/a)^4;
    f1=((c/a)^2*(sin(fi))^2+(cos(fi))^2)^0.25;
    f2=(sec(pi*c/2/b*sqrt((a/t))))^.5;
    g=1+(0.1+0.35*(c/a)*(a/t)^2)*(1-sin(fi))^2;
    p=0.2+(c/a)+0.6*(a/t);
    G11=-0.04-0.41*(c/a);
    G12=0.55-1.93*(c/a)^(3/4)+1.38*(c/a)^(3/2);
    G21=-2.11-0.77*(c/a);
    G22=0.55-0.72*(c/a)^(3/4)+0.14*(c/a)^(3/2);
    H1=1+G11*(a/t)+G12*(a/t)^2;
    H2=1+G21*(a/t)+G22*(a/t)^2;
end

F=(M1+M2*(a/t)^2+M3*(a/t)^4)*f1*f2*g;
H=H1+(H2-H1)*(sin(fi))^p;
Ya=F*sqrt(1/Q);
Yb=H*Ya;
K_check_ctip=(Ya*max(sigmaA)+Yb*max(sigmaB))*sqrt(pi*a);

K_atip=0; K_ctip=0;
a=ai; i=1;

if K_check_atip>Kth
    while (a<af)&&(K_atip<KIc)
        % Analysis of a-tip (crack depth)
        fi=90; % 0 at c-tip, 90 at a-tip (full depth of crack)
        if a<=c
            Q=1+1.464*(a/c)^1.65;
            M1=1.13-0.09*(a/c);
            M2=-0.54+0.89/(0.2+(a/c));
            M3=0.5-1/(0.65+(a/c))+14*(1-(a/c))^24;
            f1=((a/c)^2*(cos(fi))^2+(sin(fi))^2)^0.25;
            f2=(sec(pi*c/2/b*sqrt((a/t))))^0.5;
            g=1+(0.1+0.35*(a/t)^2)*(1-sin(fi))^2;
            p=0.2+(a/c)+0.6*(a/t);
            G11=-1.22-0.12*(a/c);
            G21=0.55-1.05*(a/c)^(3/4)+0.47*(a/c)^(3/2);
            H1=1-0.34*(a/t)-0.11*(a/c)*(a/t);
            H2=1+G11*(a/t)+G21*(a/t)^2;
        else
            Q=1+1.464*(c/a)^1.65;
            M1=sqrt(c/a)*(1+0.04*(c/a));
            M2=0.2*(c/a)^4;
            M3=-0.11*(c/a)^4;
            f1=((c/a)^2*(sin(fi))^2+(cos(fi))^2)^0.25;
            f2=(sec(pi*c/2/b*sqrt((a/t))))^.5;
            g=1+(0.1+0.35*(c/a)*(a/t)^2)*(1-sin(fi))^2;
            p=0.2+(c/a)+0.6*(a/t);
            G11=-0.04-0.41*(c/a);
            G12=0.55-1.93*(c/a)^(3/4)+1.38*(c/a)^(3/2);
            G21=-2.11-0.77*(c/a);
            G22=0.55-0.72*(c/a)^(3/4)+0.14*(c/a)^(3/2);
            H1=1+G11*(a/t)+G12*(a/t)^2;
            H2=1+G21*(a/t)+G22*(a/t)^2;
        end

        F=(M1+M2*(a/t)^2+M3*(a/t)^4)*f1*f2*g;
        H=H1+(H2-H1)*(sin(fi))^p;
        Ya=F*sqrt(1/Q);
        Yb=H*Ya;
        K_atip=(Ya*max(sigmaA(i))+Yb*max(sigmaB(i)))*sqrt(pi*a);

        % Analysis of c-tip (crack width)
        fi=0; % 0 at c-tip, 90 at a-tip (full depth of crack)
        if a<=c
            Q=1+1.464*(a/c)^1.65;
            M1=1.13-0.09*(a/c);
            M2=-0.54+0.89/(0.2+(a/c));
            M3=0.5-1/(0.65+(a/c))+14*(1-(a/c))^24;
```

```
            f1=((a/c)^2*(cos(fi))^2+(sin(fi))^2)^0.25;
            f2=(sec(pi*c/2/b*sqrt((a/t))))^0.5;
            g=1+(0.1+0.35*(a/t)^2)*(1-sin(fi))^2;
            p=0.2+(a/c)+0.6*(a/t);
            G11=-1.22-0.12*(a/c);
            G21=0.55-1.05*(a/c)^(3/4)+0.47*(a/c)^(3/2);
            H1=1-0.34*(a/t)-0.11*(a/c)*(a/t);
            H2=1+G11*(a/t)+G21*(a/t)^2;
        else
            Q=1+1.464*(c/a)^1.65;
            M1=sqrt(c/a)*(1+0.04*(c/a));
            M2=0.2*(c/a)^4;
            M3=-0.11*(c/a)^4;
            f1=((c/a)^2*(sin(fi))^2+(cos(fi))^2)^0.25;
            f2=(sec(pi*c/2/b*sqrt((a/t))))^.5;
            g=1+(0.1+0.35*(c/a)*(a/t)^2)*(1-sin(fi))^2;
            p=0.2+(c/a)+0.6*(a/t);
            G11=-0.04-0.41*(c/a);
            G12=0.55-1.93*(c/a)^(3/4)+1.38*(c/a)^(3/2);
            G21=-2.11-0.77*(c/a);
            G22=0.55-0.72*(c/a)^(3/4)+0.14*(c/a)^(3/2);
            H1=1+G11*(a/t)+G12*(a/t)^2;
            H2=1+G21*(a/t)+G22*(a/t)^2;
        end

        F=(M1+M2*(a/t)^2+M3*(a/t)^4)*f1*f2*g;
        H=H1+(H2-H1)*(sin(fi))^p;
        Ya=F*sqrt(1/Q);
        Yb=H*Ya;
        K_ctip=(Ya*max(sigmaA(i))+Yb*max(sigmaB(i)))*sqrt(pi*a);

        if K_atip>Kth
            growth4_a=(C*K_atip^m)*1e-3*step;
            a=a+growth4_a;
            %disp(num2str(a));
        end
        if K_ctip>Kth
            growth4_c=(C*K_ctip^m)*1e-3*step;
            c=c+growth4_c;
            %disp(num2str(c));
        end
        K4_atip(i)=K_atip;
        K4_ctip(i)=K_ctip;
        crack4_a(i)=a;
        crack4_c(i)=c;
        N4(i)=i;
        i=i+1;
    end
end

disp(' ')
disp('***')
disp('CASE #4: elliptical surface crack in plate (axial+bending stress)')
if K_check_ctip<Kth
    disp(' ')
    disp('K_check_ctip<Kth')
    disp(' ')
end

if K_check_atip<Kth
    disp(' ')
    disp('K_check_atip<Kth')

elseif K_check_atip>Kth
    disp(' ')
    disp(['Crack length (a): ',num2str(crack4_a(i-1)),' mm'])
    disp(['Crack width (2c): ',num2str(2*crack4_c(i-1)),' mm'])
    disp(['Stress intensity factor, Ka: ',num2str(K4_atip(i-1)),'
      MPa*m^.5'])
```

```
    disp(['Stress intensity factor, Kc: ',num2str(K4_ctip(i-1)),'
      MPa*m^.5'])
    disp(['Number of stress cycles: ',num2str(N4(i-1)*step),' cycles'])
else
    disp(' ')
    disp('K_check_atip = Kth')
end

K_check4=K_check_atip;

%% Error check
%#ok<*SAGROW>
```

9.6 Electrical crack growth

```
close all
clear
lw=2;                   % Line width in figures

% Constants
eps_r_XLPE=2.3;         % Relative permittivity XLPE
eps_r_WT=80;            % Relative permittivity Water Tree
eps_r_Cu=1;             % Relative permittivity Copper
eps_0=8.8541878e-12;    % Permittivity in vacuum [F/m]

gamma_XLPE=1e-17;       % Conductivity XLPE [Siemens/m]
gamma_WT=1e-8;          % Conductivity Water Tree [Siemens/m]
gamma_Cu=9.33e6;        % Conductivity Copper (correct to 59e6 [Siemens/m]?)

f=50;                   % Electrical frequency [Hz]
T=0.04;                 % Maxwell stress cycle simulation time [s]

% Water tree dimensions
a=2e-6;                 % Width of ellipse [m]
b=4e-6;                 % Length of ellipse [m]
c=1e-6;                 % Width of "mouth" [m]

% Radius of the conductor, r [m]
r=1.76e-3;
r_vec=0:r/10:r;

% Electric field strength from Young, E [V/m]
E=-5.42*1e7*r_vec.^0.45+1.03e7;

% Electric field strength from Chalmers, E [V/m]
EC=-1.4212*1e7*r_vec.^0.5061+2.898e6;

% E=x*r^(z1)+y
x=-5.314e+8; y= 3.959e+8; z1=  0.04808;

% Maxwell stress, sig_MW
sigMW=0.5*eps_0*(eps_r_XLPE-1)*(2*z1*x^2*r_vec.^(2*z1-
1)+2*z1*y*(x*r_vec.^(z1-1)));
sigMW=sigMW/1e3; % to kPa

% Cyclic Maxwell stress
t=0:(1/f/100):T;
cycle=sin(2*pi*f*t);

% Water tree propagation, see p. 170
frequency=f;
Cycles_10min=frequency*60*10;
Ra=b/a;
Stress_cycle= 6204;
Monomer_diameter=390e-12; %[pm]
Monomers_broke10min=  2.6e+04;
Watertree_growth=Monomers_broke10min*Monomer_diameter; % 7.02nm
```

```
Watertree_growth1min=Watertree_growth/10;
Limit_length= 1.0560e-3;
time=Limit_length/Watertree_growth1min; %[min]
Time_days=time/1440;
Time_years=Time_days/365;

%% Plots

figure(1), clf
plot(r_vec,-sigMW,'ro-','LineWidth',lw), hold on, grid on
xlabel('Distance from core, r [m]')
ylabel('Maxwell stress, \sigma_{MW} [kPa]')
legend('Maxwell Stress With Distance [20]')
axis([0 r -1e4 max(-sigMW)+1e4])
print -djpeg90 Maxwell_stress

figure(2), clf
plot(t,-cycle*sigMW(1,2),'g-','LineWidth',lw), hold on, grid on
plot(t,-cycle*sigMW(1,3),'b-','LineWidth',lw)
plot(t,-cycle*sigMW(1,4),'r-','LineWidth',lw)
plot(t,-cycle*sigMW(1,5),'k-','LineWidth',lw)
plot(t,-cycle*sigMW(1,6),'m-','LineWidth',lw)
plot(t,-cycle*sigMW(1,7),'g--','LineWidth',lw)
plot(t,-cycle*sigMW(1,8),'b--','LineWidth',lw)
plot(t,-cycle*sigMW(1,9),'r--','LineWidth',lw)
plot(t,-cycle*sigMW(1,10),'k--','LineWidth',lw)
plot(t,-cycle*sigMW(1,11),'m--','LineWidth',lw)
xlabel('Time, t [s]')
ylabel('Maxwell stress, \sigma_{MW} [kPa]')
legend('r = 0.1r m','r = 0.2r m','r = 0.3r m','r = 0.4r m','r = 0.5r m'...
 ,'r = 0.6r m','r = 0.7r m','r = 0.8r m','r = 0.9r m','r = 1r m')
print -djpeg90 Maxwell_stress_cyclic
```

DEPARTMENT OF MECHANICS AND
MARITIME SCIENCES
CHALMERS UNIVERSITY OF TECHNOLOGY
Gothenburg, Sweden 2021
www.chalmers.se

CHALMERS
UNIVERSITY OF TECHNOLOGY